

Global analysis of fragmentation functions to light neutral hadrons

Jun Gao¹, ChongYang Liu¹, Mengyang Li², XiaoMin Shen^{3,1}, Hongxi Xing^{2,4,5}, Yuxiang Zhao^{3,5,6,7}, Yiyu Zhou^{8,9,10}

¹*State Key Laboratory of Dark Matter Physics, Shanghai Key Laboratory for Particle Physics and Cosmology, Key Laboratory for Particle Astrophysics and Cosmology (MOE),*

School of Physics and Astronomy, Shanghai Jiao Tong University, Shanghai 200240, China

²*State Key Laboratory of Nuclear Physics and Technology, Institute of Quantum Matter, South China Normal University, Guangzhou 510006, China*

³*Institute of Modern Physics, Chinese Academy of Sciences, Lanzhou, Gansu 730000, China*

⁴*Guangdong Basic Research Center of Excellence for Structure and Fundamental Interactions of Matter, Guangdong Provincial Key Laboratory of Nuclear Science, Guangzhou 510006, China*

⁵*Southern Center for Nuclear-Science Theory (SCNT), Institute of Modern Physics, Chinese Academy of Sciences, Huizhou 516000, China*

⁶*University of Chinese Academy of Sciences, Beijing 100049, China*

⁷*Key Laboratory of Quark and Lepton Physics (MOE) and Institute of Particle Physics, Central China Normal University, Wuhan 430079, China*

⁸*Key Laboratory of Atomic and Subatomic Structure and Quantum Control (MOE), Guangdong-Hong Kong Joint Laboratory of Quantum Matter, Guangzhou 510006, China*

⁹*Department of Physics, University of Turin, via Pietro Giuria 1, I-10125 Torino, Italy*

¹⁰*INFN, Section of Turin, via Pietro Giuria 1, I-10125 Torino, Italy **

Fragmentation functions (FFs) are crucial non-perturbative components in quantum chromodynamics (QCD), playing a vital role in predictions and understanding of the hadronization process. In this paper, we present the FFs for K_S^0 , η , π^0 mesons, and Λ baryons in the context of global QCD analysis. The data included in the fit are from single inclusive e^+e^- annihilation (SIA), semi-inclusive deep-inelastic scattering (SIDIS) and proton-proton collisions, with kinematic cuts carefully applied to ensure validity of collinear factorization and perturbative QCD expansion. For the first time, data from SIDIS and hadron-in-jet production in SIA have been incorporated into the extraction of FFs for light-flavor neutral hadrons. Our analysis reveals that these data play a critical role in constraining the gluon distribution, and in distinguishing between different quark flavors. Pulls from different datasets are also studied by performing alternative fits with systematically subtracting groups of data from the nominal fit. For the quality of the fit, good χ^2 values are achieved for most of the datasets, and FFs are generally well constrained within the momentum fraction region (0.1, 0.5). The extracted K_S^0 fragmentation functions, together with the K_S^0 FFs constructed from K^\pm FFs via isospin symmetry, are used to test isospin symmetry in kaon fragmentation. Although a definitive conclusion cannot be reached yet, these studies have identified several potential measurements that can be performed at existing facilities, which may ultimately help us to arrive at a conclusive answer. With the comprehensive species of FFs extracted within the NPC framework, we are able to perform a test on the momentum sum rule with the light-flavor charged and neutral hadrons. These neutral hadrons are found to carry a relatively smaller fraction of the fragmenting parton's momentum compared to the charged ones. The central and Hessian error sets of the fitted FFs, denoted as NPC23, are publicly available in the form of LHAPDF6 grids.

*Electronic address:

jung49@sjtu.edu.cn

liucy1999@sjtu.edu.cn

limengyang@m.scnu.edu.cn

xiaominshen@impcas.ac.cn

hxing@m.scnu.edu.cn

yxzhao@impcas.ac.cn

yiyu.zhou@unito.it

Contents

I. Introduction	3
II. Overview of the NPC23 analysis of FFs	4
A. Executive Summary	4
B. Experimental data sets fitted	8
1. K_S^0 data	8
2. Λ data	10
3. η data	11
4. π^0 data	12
III. Theoretical inputs to the NPC23 analysis	14
A. Parametrization	14
B. Theoretical computation method	15
C. Goodness of fit function and the covariance matrix	15
IV. The NPC23 predictions	17
A. Moments and sum rules of FFs	17
B. Neutral hadrons in jet fragmentation	21
C. Ratios of neutral and charged kaon production	23
V. Quality of fit to data	27
A. K_S^0 production	27
B. Λ production	31
C. η production	35
D. π^0 production	38
VI. Alternative fits	41
A. K_S^0 production	41
B. Λ production	45
VII. Discussion and Conclusions	48
A. Comparison to other groups	48
B. Impact of the Belle measurements	51
C. Impact of the LHCb measurements	54
D. LHAPDF6 grid	58
References	60

I. INTRODUCTION

Understanding hadronization is essential for exploring color confinement in quantum chromodynamics (QCD). In high-energy collisions, hadrons are abundantly produced via fragmentation of primary quarks and gluons. Fragmentation functions (FFs) are proposed to describe the hadronization process, characterizing the probability density of an outgoing parton (quark or gluon) transforming into color neutral hadrons, with respect to the light-cone momentum fraction it carries [1–3].

As one of the fundamental objects of non-perturbative QCD, FFs are widely studied and have many important applications [4]. In collinear factorization, the cross sections can be factorized into perturbatively calculable short-distance matrix elements, and non-perturbative distribution functions [5], including parton distribution functions (PDFs) and FFs, each characterizing the hard scattering process and universal long-distance effects, respectively. Therefore, leveraging the universality property, FFs can be extracted from various hadron production processes, such as e^+e^- annihilation (SIA), semi-inclusive deep-inelastic scattering (SIDIS), and proton-proton collisions. These extracted FFs can then be utilized to make predictions for hadron production in different high-energy processes, providing a powerful tool for theoretical and phenomenological studies in QCD. Apart from collinear factorization, FFs are also involved in transverse momentum dependent (TMD) factorization. The hadronization in TMD processes is more complicated than in collinear processes due to the inclusion of an additional kinematic variable, namely the transverse momentum \mathbf{k}_T of the hadron with respect to the fragmenting parton. However, since TMD FFs can be matched to collinear FFs [6], our knowledge of collinear FFs remains crucial in the study of TMD physics. Recently, study of the transverse energy-energy correlator (TEEC) has brought a lot of insight into TMD physics [7–9]. TEEC is defined by integrating the differential cross section weighted by the transverse energy of the final-state particles. Since the final-state hadrons are summed over, the calculation of the TEEC must be approximated due to limitations in the available hadron FFs. This approximation arises because the current set of FFs is restricted to only a few types of hadrons. The situation is even worse when nuclear modification is studied [8, 9] because the availability of nuclear FFs is more limited [10–13]. Besides, the study of polarization phenomena, especially the Λ baryon spontaneous transverse polarization [14] also relies on precise inputs of collinear unpolarized FFs of Λ . With the key applications of collinear FFs for various hadrons, their determination has become a more pressing subject.

Unfortunately, direct calculation of FFs has not been realized due to its non-perturbative and time-dependent nature, although initial efforts of using quantum computing have been proposed recently [15, 16]. Global analysis remains the most robust method for determining the FFs. In the past few decades, great progress has been made towards the calculation of the hard scattering cross sections at higher orders in QCD. In particular, coefficient functions for SIA at the next-to-next-to-leading order (NNLO) have been calculated in Refs. [17–20]. Results of threshold resummation are available at the next-to-next-to-leading logarithmic (N^2LL) [21, 22] and next-to-next-to-next-to-leading logarithmic (N^3LL) [23] accuracy, which are important at large momentum fractions. For SIDIS, the next-to-leading order (NLO) coefficient functions are available in Refs. [24–29]. The NNLO coefficient functions are recently computed in Refs. [30, 31]. On the other hand, approximate NNLO and N^3LO results have been obtained via threshold resummation [32, 33]. The hard cross sections for single inclusive hadron production in proton-proton collisions are calculated up to NLO in [34–36] and NNLO in [37]. Besides, hadron production inside jets can provide direct access to the shape of FFs [38–41] and result in a strong constraint to the gluon FFs, as demonstrated in Ref. [42] for the FFs of D^* -meson and in Ref. [43, 44] for the FFs of light charged hadrons. Corresponding jet fragmentations have been calculated at NLO in Refs. [45–49]. Finally, the scale dependence of FFs, which is evolved by the Dokshitzer-Gribov-Lipatov-Altarelli-Parisi (DGLAP) evolution equations with time-like splitting kernels, can be perturbatively calculated. The time-like splitting kernels are available at $\mathcal{O}(\alpha_s^3)$ in Refs. [50–55], where α_s is the strong coupling constant.

With the results from perturbative QCD calculations and precise experimental measurements at hand, there are several groups providing phenomenological determinations of FFs. For light charged hadrons, including π^\pm , K^\pm , and p/\bar{p} , representative efforts can be found in the works of BKK [56, 57], KKP [58], BFGW [59], S. Kretzer [60], KLC [61], DSS [62–65], HKNS [66], AKK [67], NNFF [68], MAPFF [69], JAM [70] and NPC23 [43, 44, 71]. They are carried out at NLO in QCD with global data sets and different theoretical prescriptions. There also exist determinations of FFs at NNLO with SIA data only [72–76], and at approximate NNLO with SIA and SIDIS data [77, 78]. The full NNLO analysis of light charged hadron FFs using SIA and SIDIS is recently completed in [71]. For light neutral hadrons, for instance, K_S^0 , Λ , and η , their FFs are less known due to the lack of precision data. The K_S^0 meson FFs have been extracted in the past by BKK96 [79], AKK05 [80], AKK08 [67], SAK20 [81], LAXZ [82] and FF24 [83] using SIA data only (except AKK08 that used pp data as well). The Λ baryon FFs have been extracted by DSV [28], AKK05 [80], AKK08 [67] and SAK20 [81], also using only SIA data (with the exception of AKK08 which also used pp data). The η meson FFs have been fitted in the past by AESSS [84] with SIA and pp data, and by LAXZ [82] with SIA data using NNLO formula and higher twist effects.

In this work, we present a global analysis at NLO in QCD for the FFs of light neutral hadrons, namely K_S^0 , Λ ,

η , and π^0 . We include for the first time the SIDIS data from ZEUS [85], and for the first time hadron-in-jet data from SIA three jet production. The inclusion of the latter dataset has been made feasible by the development of the FMNLO program [46, 86]. This advancement has resulted in a noticeable constraint on the gluon FFs. This analysis extends our previous work on FFs of light charged hadrons (NPC23) [43, 44, 71] and allows a further test on the sum rules of FFs. We are also able to study the isospin symmetry in the FFs of light hadrons, which is found to be valid for pions. On the other hand, our analysis reveals that the current experimental data are insufficient to draw definitive conclusions regarding isospin symmetry in kaon FFs. To address this limitation, we propose several decisive measurements that could be carried out in existing experimental facilities.

The remainder of the paper is organized as follows. Section II provides an overview of the NPC23 FFs, and lists the experimental data included in the fit. In Section III, we discuss the theoretical aspect of our global QCD analysis, including the parameterization of FFs and the goodness-of-fit criterion. In Section IV, we provide the physics quantities of interest, predicted by the fitted FFs of the neutral hadrons. Section V presents the quality of fit to the data by listing the χ^2 values and showing detailed comparisons between theory and data. In Section VI, we provide alternative fits by subtracting a certain group of data to demonstrate constraints and pulls on FFs from different experiments. Finally, in Section VII, we present a summary of our findings and draw conclusions based on the results and discussions presented throughout the paper.

II. OVERVIEW OF THE NPC23 ANALYSIS OF FFs

In this section, we provide an overview of our FFs obtained from an NLO analysis of global data sets, for K_S^0 meson, Λ baryon, η meson and π^0 meson. We summarize the main features of the NPC23 FFs in Section II A, and list the fitted data in Section II B.

A. Executive Summary

The extracted fragmentation functions for K_S^0 , Λ and η are given in Figs. 1 to 3 together with their uncertainties. The FFs are plotted as functions of the light-cone momentum fraction z at an initial scale $Q_0 = 5$ GeV. Both the actual values and ratios to the central values are shown in the plots. We have set $D_q^h = D_q^h$ for $h = K_S^0$, Λ and η , with q being all the active quark flavors. The detailed reason for making this choice will be given later in Section III A. The FFs are in general well constrained within $z \sim (0.1, 0.5)$. Otherwise the FFs exhibit large uncertainties due to either precision of the data or the lack of power on flavor separation. It is especially the case for the FFs of η meson from gluon and heavy quarks (b and c).

In Fig. 1, we show the fitted K_S^0 FFs in blue bands for the gluon and all five active quarks. It should be noted that with SIA data only, one cannot discriminate FFs from d and s quarks. This limitation arises because both quark types possess identical electric and weak charges, leading to indistinguishable contributions to the observed hadron production in SIA processes. On the other hand, current data on neutral hadrons from SIDIS and pp collisions are also not sufficient for separating d and s quarks due to limited measurements as well as the large uncertainties. Thus we have applied a prior constraint on the ratio of FFs from s to d quarks, which is motivated by the relatively larger mass of strange quark, with further details given in Sections III A and V A. With the aforementioned prior constraint, the K_S^0 FFs are well constrained for all parton flavors in a wide kinematic region.

We also show the K_S^0 FFs constructed from K^\pm FFs in orange bands, labeled with “iso” in Fig. 1, assuming isospin symmetry. The formulae for constructing K_S^0 FFs from isospin symmetry read

$$D_q^{K_S^0} = \frac{1}{2} \left(D_q^{K^0} + D_q^{\bar{K}^0} \right) = \frac{1}{2} \left(D_{q'}^{K^+} + D_{q'}^{K^-} \right), \quad (1)$$

where $q(q') = u(d)$ or $d(u)$. While for flavors $q = s, c, b$ and gluon, we have:

$$\begin{aligned} D_q^{K_S^0} &= \frac{1}{2} \left(D_q^{K^0} + D_q^{\bar{K}^0} \right) = \frac{1}{2} \left(D_q^{K^+} + D_q^{K^-} \right), \\ D_g^{K_S^0} &= \frac{1}{2} \left(D_g^{K^0} + D_g^{\bar{K}^0} \right) = \frac{1}{2} \left(D_g^{K^+} + D_g^{K^-} \right). \end{aligned} \quad (2)$$

Here the K^\pm FFs are from the NPC23 NLO analysis of charged hadrons [44].

Both the fitted and constructed K_S^0 FFs exhibit a consistent pattern, with the FF originating from the s quark being slightly larger than that from the d quark. However, it is worth noting that the error bands associated with the FFs of the s quark barely overlap, indicating a degree of uncertainty in this observation. The FFs from heavy quarks

are well determined thanks to the inclusion of SLD measurements with c/b -tagging [87]. The charm quark FFs are slightly favored over those of the bottom quark, especially at large- z , probably due to its preference of decays into the strange quark. The fitted and constructed FFs from c and b quark show clear differences which are much larger than the quoted uncertainties. For u quark, we find that the fitted and constructed FFs are significantly different, with the fitted result showing a peak around $z = 0.05$, while the constructed result being relatively flat. Finally, for the FFs from gluon, the fitted results only agree with the constructed results in large- z region, and is much larger than the constructed result in middle and low z regions.

In general, the fitted and constructed FFs of K_S^0 do not coincide with each other particularly for those from gluon and u, c, b quarks. These discrepancies could indicate possible isospin symmetry violation in fragmentation to kaons. However, that can also be due to the poor quality of data or even tensions between different data sets. For instance, the smaller gluon FFs to charged kaons are predominantly pulled by the hadron-in-jet data from pp collisions which are absent in the analysis of neutral kaons. The FFs to neutral kaons from u quark are only directly constrained by a few data points from HERA with large uncertainties. Therefore, further measurements, especially data from SIDIS or pp collisions, will be needed for clarifications, as we will elaborate in Section IV C. Similar observation concerning K_S^0 FFs from a direct fit and from a construction with isospin symmetry is also reported in the SAK20 analysis [81].

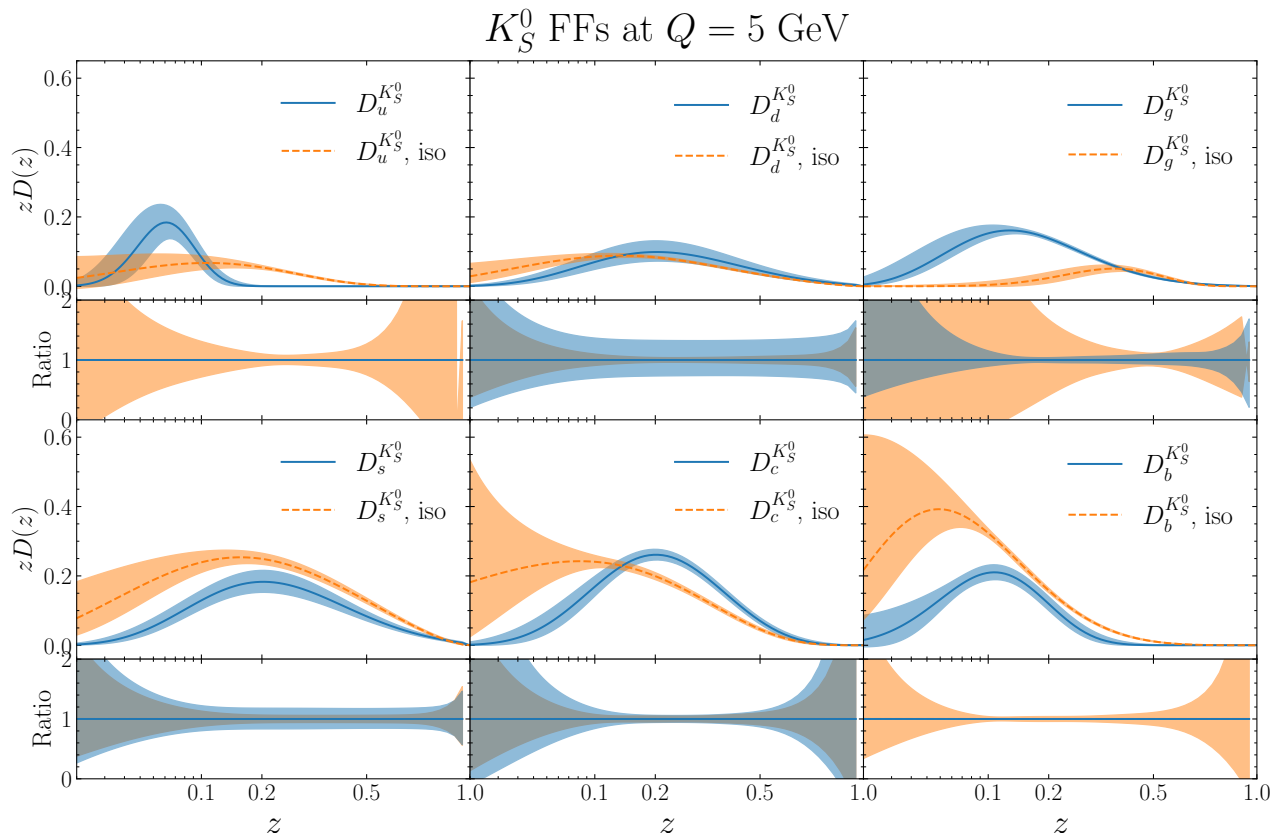


FIG. 1: The NPC23 fragmentation functions (FFs) for K_S^0 at scale $Q = 5$ GeV. The FFs are plotted with respect to z , the light-cone momentum fraction of parent parton carried by the hadron. The colored bands represent uncertainties estimated from Hessian method with 68% confidence level, with blue for the fitted K_S^0 FFs and orange for the reconstructed K_S^0 FFs. The relative uncertainties are shown correspondingly in lower panels of each subplots.

The relative uncertainties are not plotted up to $z = 1$ because the central values vanish towards the end point.

The Λ FFs are shown in Fig. 2, where a good constraint is found for all quark flavors and gluon. We have set the FFs from u and d quarks to be equal due to insufficient experimental data to constrain them independently. Additionally, it has been argued in previous studies [88, 89] that isospin symmetry holds well for fragmentation to Λ baryon, further supporting the validity of this approach.

Our study shows that strange quark is clearly favored compared to u and d quarks, despite the fact that they are all constituent quarks. This can be expected because strange quark has a much larger mass than that of u and d quarks, and this makes Λ baryon less likely to be produced from u and d quarks. As for heavy quarks, the c quark

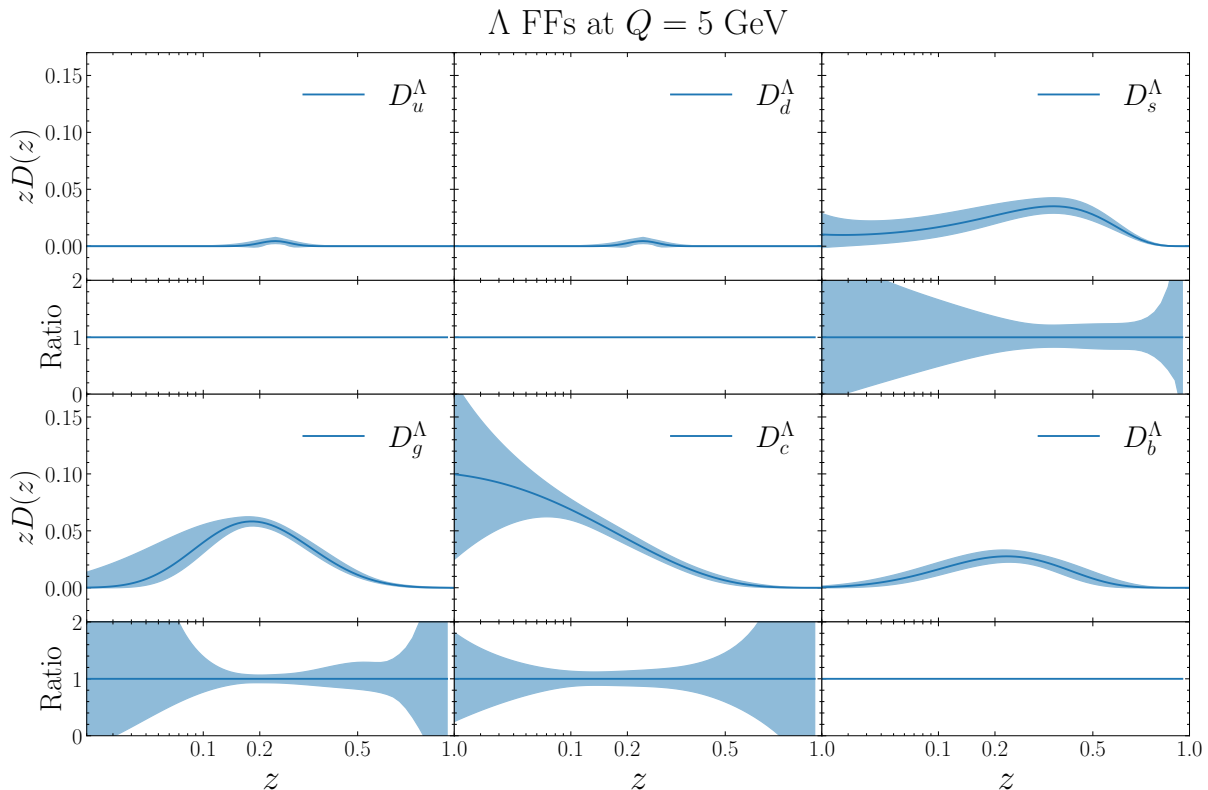


FIG. 2: Similar to Fig. 1, but for Λ FFs. We have set $D_u^\eta = D_d^\eta$.

FF exhibits a typical behavior in which the probability peaks at low z and decreases monotonically with increasing z . The b quark is clearly disfavored compared to the c quark. This is probably due to the same fact as explained in the case of K_S^0 FFs. However, we do emphasize that, due to relatively weaker constraints for Λ baryon compared to π and K mesons, the behavior of b quark FFs has to be further studied when more data are available. As for the FFs from gluon, one interesting aspect is that, compared to the case of K_S^0 meson, the FFs of Λ baryon peak at a slightly larger z value. This can be explained by the fact that a heavier hadron requires gluons to carry larger momentum fractions compared to those in lighter hadrons [66, 70, 90]. The same pattern can also be observed when comparing the FFs from bottom quark to K_S^0 and Λ .

The η FFs are shown in Fig. 3. According to the symmetries in the η wave function we have set $D_u^\eta = D_d^\eta$. Furthermore, due to lack of direct constraint from the world data with heavy quark tagging, we assume $D_c^\eta = D_b^\eta$. The FFs of the strange quark are roughly twice as large as those of the up quark, which is expected given the relatively larger mass of the strange quark and the fact that s is more favored in the η wave function $|\eta\rangle = (|u\bar{u}\rangle + |d\bar{d}\rangle - 2|s\bar{s}\rangle)/\sqrt{6}$. We observe that the FFs of η meson from heavy quarks are much less than those of the favored quarks, except at $z \sim 0.1$, where the FFs from the charm (bottom) quark are slightly higher than those of the up (down) quarks. Although relatively good constraints on quarks are obtained, the FFs for gluons remain poorly constrained in the low z region. The large uncertainties of η FFs compared to those of K_S^0 and Λ clearly indicate that further high-precision measurements of η meson production are needed.

Finally, we show our π^0 FFs in Fig. 4, which are computed via isospin symmetry from π^\pm FFs given in previous NPC23 analyses [44]:

$$D_q^{\pi^0} = \frac{1}{4} \left(D_q^{\pi^+} + D_q^{\pi^-} + D_{q'}^{\pi^+} + D_{q'}^{\pi^-} \right), \quad (3)$$

where $q(q') = u(d)$ or $d(u)$. While for gluon and the remaining quark flavors, we have:

$$D_q^{\pi^0} = \frac{1}{2} \left(D_q^{\pi^+} + D_q^{\pi^-} \right), \quad D_g^{\pi^0} = \frac{1}{2} \left(D_g^{\pi^+} + D_g^{\pi^-} \right). \quad (4)$$

By this formalism, $D_d^{\pi^0} = D_u^{\pi^0} = D_u^{\pi^0} = D_u^{\pi^0}$. The π^0 FFs from the remaining quarks and the gluon are essentially the same as those of the π^\pm . Importantly, we find that the π^0 FFs obtained in this way can describe very well the

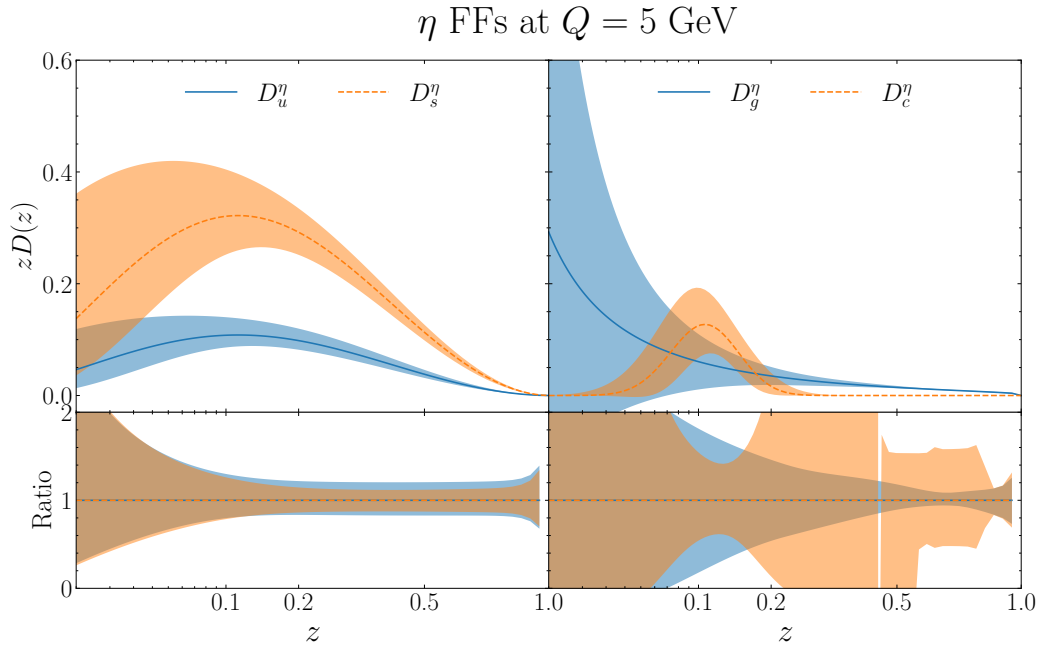


FIG. 3: Similar to Fig. 1, but for η FFs. We have set $D_u^\eta = D_d^\eta$ and $D_c^\eta = D_b^\eta$.

world data on π^0 production (see Section VD). This together with the result from our previous analysis of charged pions indicate that the isospin symmetry is well valid in fragmentation to pions.

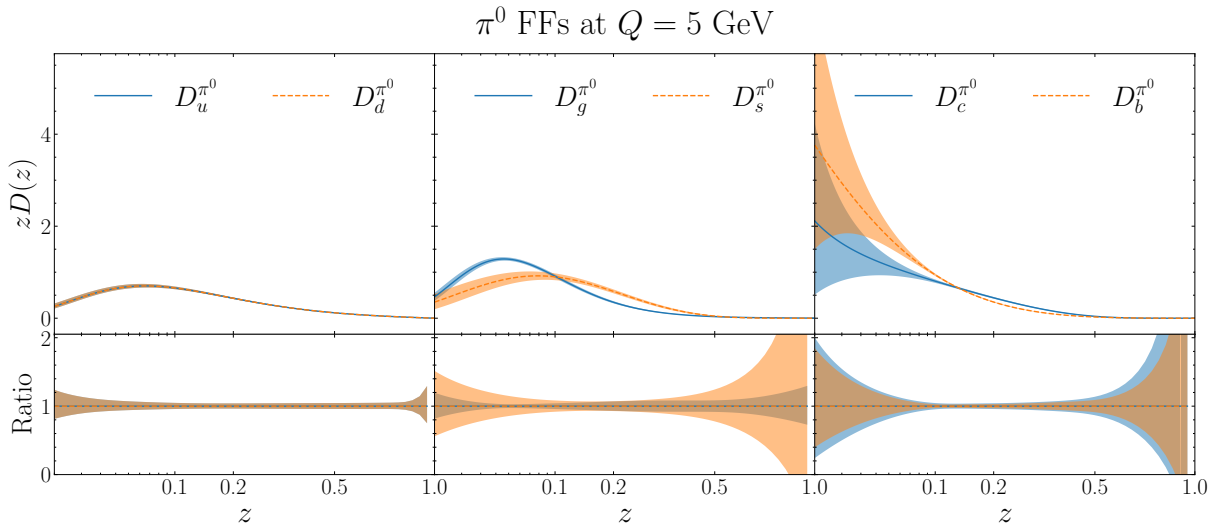


FIG. 4: Similar to Fig. 1, but for π^0 FFs. The FFs are constructed via isospin symmetry from those of charged pions.

B. Experimental data sets fitted

In this section, we summarize the experimental data used for the extraction of the K_S^0 meson, η meson and Λ baryon FFs. The π^0 FFs, on the other hand, are derived from π^\pm FFs via isospin symmetry. A list of π^0 datasets is also provided to benchmark the resulting π^0 FFs.

1. K_S^0 data

For the extraction of K_S^0 FFs, data from SIA, SIDIS, and pp collisions are incorporated. The SIA datasets for K_S^0 are summarized in Table I, with information on collaboration, year of paper publication, center-of-mass energy, identified hadrons (parton flavor tags and in-jet production are also specified), measured observable, and number of data points after applying the cuts. For SIA experiments at Z -pole, we include data from OPAL [91–93], ALEPH [94], DELPHI [95] and SLD [87]. We also include data below Z -pole from TPC [96], MARK II [97], TASSO [98, 99], HRS [100], CELLO [101] and TOPAZ [102]. Additionally, we include c -tagged and b -tagged data from SLD [87] and three-jet data from ALEPH [103]. The SLD c and b -tagged K_S^0 production data are supposed to provide sensitivity to the heavy quark distributions. On the other hand, since the third most energetic jet in three-jet events is typically a gluon jet, the ALEPH dataset [103] is expected to be sensitive to gluon FFs. The DELPHI data at the center-of-mass energies $\sqrt{s} = 183$ GeV and 189 GeV [104] are not included in our fit, since they are known to be in tension with the other world data [67, 80, 81]. We have also excluded the OPAL light flavor tagged data [105] from our fits as those data are based on leading-order analysis. The BESIII measurement on K_S^0 production [106] is not included in this fit as the treatment of mass correction at low hadron momentum is beyond the scope of this work. Moreover, we observe that the NPC23 NNLO FFs [71] yield predictions that are consistent with the data for both charged and neutral light hadrons in the large hadron momentum region [107].

In Table I, the kinematic variables in

$$\frac{1}{\beta\sigma_h} \frac{d\sigma}{dx_h}, \quad \frac{s}{\beta} \frac{d\sigma}{dx_h}, \quad \frac{1}{\sigma_h} \frac{d\sigma}{dx_h}, \quad (5)$$

are defined as $x_h \equiv 2E_{K_S^0}/\sqrt{s}$, $\beta \equiv p_{K_S^0}/E_{K_S^0}$, and σ_h is the total hadronic cross section. Here $p_{K_S^0}$ and $E_{K_S^0}$ are the momentum and energy of the identified K_S^0 , \sqrt{s} is the center-of-mass energy of the e^+e^- collision.

On the other hand, the observables that are differential in x_p or ξ :

$$\frac{1}{\sigma_h} \frac{d\sigma}{d\xi}, \quad \frac{1}{\sigma_h} \frac{d\sigma}{dx_p}, \quad \frac{1}{\sigma_{\text{jet}}} \frac{d\sigma}{dx_p}, \quad (6)$$

are converted to distributions in x_h such that they are directly computed by FMNLO without further hadron mass corrections. Here $x_p \equiv 2p_{K_S^0}/\sqrt{s}$, $\xi \equiv -\ln(x_p)$ and σ_{jet} is the total cross section for the three-jet production. For SIA we also need the kinematic variable Q^2 which is defined as the square of invariant mass of the exchanged photon.

The SIDIS and pp datasets for K_S^0 are summarized in Table II. We include experimental data for SIDIS from ZEUS [85] for the observable:

$$\frac{1}{N_{\text{DIS}}} \frac{dN_{K_S^0}}{dz_p}, \quad (7)$$

where $z_p \equiv 2p_{K_S^0}/Q$ with $p_{K_S^0}$ being the K_S^0 momentum and $Q^2 \equiv -q^2$ being the virtuality. N_{DIS} is the number of deep inelastic scattering (DIS) events in the corresponding Q^2 and z_p bins. Finally, q^2 is given by $q^2 = (\ell - \ell')^2$ in the following process:

$$e(\ell) + p(P) \rightarrow e'(\ell') + K_S^0(p_{K_S^0}) + X, \quad (8)$$

where e and e' denote the incoming and scattered electron, respectively, while p , K_S^0 and X represent the incoming proton beam, outgoing K_S^0 and unobserved particles, respectively. Their momenta are given in the parentheses. In addition, we also define the Bjorken variable $x_B \equiv Q^2/(2P \cdot q)$ and event inelasticity $y \equiv (P \cdot q)/(P \cdot \ell)$. In the calculation, we used the relation:

$$\frac{1}{N_{\text{DIS}}} \frac{dN_{K_S^0}}{dz_p} = \frac{1}{\sigma_{\text{DIS}}} \frac{d\sigma_{K_S^0}}{dz_p}, \quad (9)$$

collaboration	year	\sqrt{s} [GeV]	final state	observable	N_{pt}
TASSO [98]	1985	14, 22 & 34	K_S^0	$\frac{s}{\beta} \frac{d\sigma}{dx_h}$	9, 6 & 13
TASSO [99]	1990	14.8, 21.5, 34.5, 35 & 42.6	K_S^0	$\frac{s}{\beta} \frac{d\sigma}{dx_h}$	9, 6, 13, 13 & 13
TPC [96]	1984	29	K_S^0	$\frac{1}{\beta\sigma_h} \frac{d\sigma}{dx_h}$	8
MARK II [97]	1985	29	K_S^0	$\frac{1}{\beta\sigma_h} \frac{d\sigma}{dx_h}$	17
HRS [100]	1987	29	K_S^0	$\frac{s}{\beta} \frac{d\sigma}{dx_h}$	12
CELLO [101]	1990	35	K_S^0	$\frac{1}{\beta\sigma_h} \frac{d\sigma}{dx_h}$	9
TOPAZ [102]	1995	58	K_S^0	$\frac{1}{\sigma_h} \frac{d\sigma}{d\xi}$	4
OPAL [91]	1991	91.2	K_S^0	$\frac{1}{\beta\sigma_h} \frac{d\sigma}{dx_h}$	7
OPAL [92]	1995	91.2	K_S^0	$\frac{1}{\sigma_h} \frac{d\sigma}{dx_h}$	16
OPAL [93]	2000	91.2	K_S^0	$\frac{1}{\sigma_h} \frac{d\sigma}{dx_h}$	16
ALEPH [94]	1998	91.2	K_S^0	$\frac{1}{\sigma_h} \frac{d\sigma}{dx_p}$	16
ALEPH [103]	2000	91.2	K_S^0	$\frac{1}{\sigma_h} \frac{d\sigma}{d\xi}$	14
ALEPH [103]	2000	91.2	$K_S^0(\text{jet})$	$\frac{1}{\sigma_{\text{jet}}} \frac{d\sigma}{d\xi}$	12, 13 & 11
DELPHI [95]	1995	91.2	K_S^0	$\frac{1}{\sigma_h} \frac{d\sigma}{dx_p}$	13
SLD [87]	1999	91.2	K_S^0	$\frac{1}{\sigma_h} \frac{d\sigma}{dx_p}$	9
SLD (tagged) [87]	1999	91.2	$K_S^0(\text{tagged})$	$\frac{1}{\sigma_h} \frac{d\sigma}{dx_p}$	9 & 9

TABLE I: Summary of SIA datasets used in K_S^0 FFs analysis. In the header line, \sqrt{s} indicates the center-of-mass energy and N_{pt} denotes the number of points (after applying the kinematic cuts). The column “year” shows the year of paper publication. The kinematic variables in the observables are defined in Eqs. (5) and (6) and corresponding texts. For SLD (tagged) [87], the numbers of data points are provided respectively for c -tagged and b -tagged K_S^0 production. For ALEPH three-jet events measurement [103], the numbers of data points are listed respectively for K_S^0 in three jets, ordered by jet energies.

collaboration	year	\sqrt{s} [GeV]	final state	observable	N_{pt}
ZEUS [85]	2012	318	K_S^0	$\frac{1}{N_{\text{DIS}}} \frac{dN_{K_S^0}}{dz_p}$	5, 5 & 2
ALICE [108]	2021	13000 & 7000	K_S^0	$\frac{dN_{K_S^0}^{13 \text{ TeV}}}{dp_T} \bigg/ \frac{dN_{K_S^0}^{7 \text{ TeV}}}{dp_T}$	10
ALICE [108]	2021	13000	K_S^0 & π^\pm	$\frac{dN_{K_S^0}}{dp_T} \bigg/ \frac{dN_{\pi^\pm}}{dp_T}$	15

TABLE II: Same as Table I, but for SIDIS and pp collisions. The kinematic variables are defined in Eq. (7) and surrounding texts. For ZEUS [85], the numbers of data points are given respectively for three Q^2 bins: (160, 640) GeV^2 , (640, 2560) GeV^2 and (2560, 20140) GeV^2 .

where σ_{DIS} is the DIS cross section.

For the data of pp collisions from ALICE [108], in order to avoid dealing with various normalization, we choose to use the ratios of K_S^0 production between different center-of-mass energies, or ratios of K_S^0 production over π^\pm production at the same center-of-mass energy:

$$\frac{dN_{K_S^0}^{13 \text{ TeV}}}{dp_T} \bigg/ \frac{dN_{K_S^0}^{7 \text{ TeV}}}{dp_T}, \quad \frac{dN_{K_S^0}}{dp_T} \bigg/ \frac{dN_{\pi^\pm}}{dp_T}. \quad (10)$$

Here p_T is the transverse momentum of the identified hadron (K_S^0 or π^\pm in this case).

collaboration	year	\sqrt{s} [GeV]	final state	observable	N_{pt}
TASSO [98]	1985	14, 22 & 34	Λ	$\frac{s}{\beta} \frac{d\sigma}{dx_h}$	3, 4 & 7
SLAC [112]	1985	29	Λ	$\frac{s}{\beta} \frac{d\sigma}{dx_h}$	15
HRS [100]	1987	29	Λ	$\frac{s}{\beta} \frac{d\sigma}{dx_h}$	8
CELLO [101]	1990	35	Λ	$\frac{1}{\beta\sigma_h} \frac{d\sigma}{dx_h}$	7
DELPHI [109]	1993	91.2	Λ	$\frac{1}{\sigma_h} \frac{d\sigma}{dx_p}$	7
ALEPH [110]	1994	91.2	Λ	$\frac{1}{\sigma_h} \frac{d\sigma}{d\xi}$	14
ALEPH [94]	1998	91.2	Λ	$\frac{1}{\sigma_h} \frac{d\sigma}{dx_p}$	16
ALEPH [103]	2000	91.2	$\Lambda(\text{jet})$	$\frac{1}{\sigma_{\text{jet}}} \frac{d\sigma}{d\xi}$	13, 12 & 9
OPAL [111]	1997	91.2	Λ	$\frac{1}{\beta\sigma_h} \frac{d\sigma}{dx_h}$	12
SLD [87]	1999	91.2	Λ	$\frac{1}{\sigma_h} \frac{d\sigma}{dx_p}$	9
SLD (tagged) [87]	1999	91.2	$\Lambda(\text{tagged})$	$\frac{1}{\sigma_h} \frac{d\sigma}{dx_p}$	4 & 4

TABLE III: Same as Table I, but for SIA Λ production. The kinematic variables in the observable are defined in Section II B 1, same as those for K_S^0 . For SLD (tagged) [87], the numbers of data points are listed respectively for c -tagged and b -tagged Λ production. In ALEPH three-jet events measurement [103], the numbers of data points are listed respectively for Λ in three jets, ordered by jet energy.

In order to maintain the validity of leading-twist factorization and perturbative convergence, we apply kinematic cuts $x_h > 0.05$ for SIA, $z_p > 0.05$ for SIDIS, and $p_T > 4$ GeV for pp collisions, respectively.

2. Λ data

For Λ production only the sum of Λ and $\bar{\Lambda}$ baryons have been measured. Thus, our fitted Λ FFs should be interpreted as an average of FFs for both Λ and $\bar{\Lambda}$. The summaries of Λ production in SIA, SIDIS and pp collisions are given in Tables III and IV, respectively. The kinetic variables for Λ production in Tables III and IV are similar to those for K_S^0 productions, as given in Section II B 1. We also apply the same kinematic cut as in the K_S^0 case.

For SIA data at Z -pole, we include data from DELPHI [109], ALEPH [94, 103, 110], OPAL [111] and SLD [87]. While for data below Z -pole, we include data from SLAC [112], TASSO [98], HRS [100] and CELLO [101]. In particular, the SLD c -tagged and b -tagged Λ production data [87] are crucial in constraining c and b FFs, while the ALEPH Λ -in-jet production data (especially Λ produced in the third most energetic jet) [103] can help in pinning down the gluon FFs. The single-inclusive Λ production data from the same ALEPH paper [103], however, is not included in our fit due to its tension with the ALEPH 1998 measurement [94]. Also, the OPAL 1992 data [113] is not included in our fit as it is superseded by the OPAL 1997 measurement [111]. The DELPHI data at center-of-mass energies $\sqrt{s} = 183$ GeV and 189 GeV [104] are not included in our fit also because they are known to have tension with the other world data [67, 80, 81]. Finally, the JADE 1981 data [114] are excluded by the p_T cut of 4 GeV applied in our fit.

For SIDIS data, we include data from ZEUS [85] in three Q^2 bins. In the case of pp collision data, we include the ratio data of Λ productions at different center-of-mass energies from ALICE [108], and the yield ratio of Λ over K_S^0 at the same center-of-mass energy from CMS [115]. For the data on the ratio of type Λ/K_S^0 , special treatment has to be given, since we are not fitting the K_S^0 and Λ FFs simultaneously. In particular, we included a fully correlated uncertainty of 5% in the ratio data of the type Λ/K_S^0 so as to properly propagate the uncertainty from K_S^0 FFs. Due to the substantial discrepancy between measurements and event generator simulations observed in [108, 115], we have chosen to exclude the Λ to K_S^0 production data from ALICE 2021 at 13 TeV [108], as well as the CMS 2011 data at 7 TeV [115], from our fit.

collaboration	year	\sqrt{s} [GeV]	final state	observable	N_{pt}
ZEUS [85]	2012	318	Λ	$\frac{1}{N_{\text{DIS}}} \frac{dN_{\Lambda}}{dz_p}$	5, 3 & 1
CMS [115]	2011	900	Λ & K_S^0	$\frac{dN_{\Lambda}}{dp_T} / \frac{dN_{K_S^0}}{dp_T}$	4
ALICE [108]	2021	13000 & 7000	Λ	$\frac{dN_{\Lambda}^{13 \text{ TeV}}}{dp_T} / \frac{dN_{\Lambda}^{7 \text{ TeV}}}{dp_T}$	7

TABLE IV: Same as Table II, but for Λ SIDIS and pp data. The kinematic variables in the observable are defined in Section II B 1, same as those for K_S^0 . For ZEUS [85], the numbers of data points are provided respectively for three Q^2 bins: (160, 640) GeV^2 , (640, 2560) GeV^2 and (2560, 20140) GeV^2 .

collaboration	year	\sqrt{s} [GeV]	final state	observable	N_{pt}
ARGUS [125]	1990	9.46	η	$\frac{s}{\beta} \frac{d\sigma}{dx_h}$	6
HRS [124]	1988	29	η	$\frac{s}{\beta} \frac{d\sigma}{dx_h}$	13
JADE [121]	1985	34.4	η	$\frac{s}{\beta} \frac{d\sigma}{x_h}$	2
JADE [122]	1990	35	η	$\frac{s}{\beta} \frac{d\sigma}{dx_h}$	3
CELLO [123]	1990	35	η	$\frac{s}{\beta} \frac{d\sigma}{dx_h}$	5
L3 [118]	1992	91.2	η	$\frac{1}{\sigma_h} \frac{d\sigma}{dx_p}$	4
L3 [119]	1994	91.2	η	$\frac{1}{\sigma_h} \frac{d\sigma}{dx_h}$	10
ALEPH [116]	1992	91.2	η	$\frac{1}{\sigma_h} \frac{d\sigma}{dx_h}$	8
ALEPH [103]	2000	91.2	η	$\frac{1}{\sigma_h} \frac{d\sigma}{dx_h}$	18
ALEPH [103]	2000	91.2	$\eta(\text{jet})$	$\frac{1}{\sigma_{\text{jet}}} \frac{d\sigma}{dx_h}$	7, 6 & 4
ALEPH [117]	2002	91.2	η	$\frac{1}{\sigma_h} \frac{d\sigma}{dx_p}$	5
OPAL [120]	1998	91.2	η	$\frac{1}{\sigma_h} \frac{d\sigma}{dx_h}$	11

TABLE V: Same as Table I, but for η SIA data. The kinematic variables in the observables are defined in Section II B 1, same as those for K_S^0 . For the ALEPH three-jet events measurement [103], the numbers of data points are listed respectively for η production in three jets, ordered by jet energy.

3. η data

We have gathered a comprehensive list of datasets from both SIA and pp measurements for the global analysis of η FFs, which are summarized in Table V and Table VI, respectively. The kinetic variables presented in Table V are similar to those of the K_S^0 productions, as given in Section II B 1. We also apply the same kinematic cut as in the K_S^0 case.

In the context of SIA measurements, most of the data was collected at the Z -pole energy, with significant contributions from the ALEPH [103, 116, 117], L3 [118, 119] and OPAL [120] collaborations. As noted in the previous sections, η -in-jet measurements from ALEPH [103] can provide additional constraints on the gluon fragmentation functions. To complement the high-energy measurements, we have included lower-energy data from the JADE [121, 122], CELLO [123], HRS [124] and ARGUS [125] experiments. These low-energy datasets, particularly the ARGUS data (with a center-of-mass energy of 9.46 GeV), are significant for flavor separation, as ARGUS operates below the threshold for b quark production.

For pp collisions, high-energy data are collected primarily by the ALICE collaboration [126–128] at center-of-mass energies of 2.76, 7, and 8 TeV. Additionally, the PHENIX collaboration [129] provides lower-energy measurements at 200 GeV, which are also included in our fits. The observables from PHENIX [129] and ALICE [126–128] are all given

collaboration	year	\sqrt{s} [GeV]	final state	observable	N_{pt}
PHENIX [129]	2011	200	η & π^0	$\frac{E d^3 \sigma_\eta}{d^3 \vec{p}} \Big/ \frac{E d^3 \sigma_{\pi^0}}{d^3 \vec{p}}$	14
ALICE [127]	2017	2760	η & π^0	$\frac{E d^3 \sigma_\eta}{d^3 \vec{p}} \Big/ \frac{E d^3 \sigma_{\pi^0}}{d^3 \vec{p}}$	6
ALICE [126]	2012	7000	η & π^0	$\frac{E d^3 \sigma_\eta}{d^3 \vec{p}} \Big/ \frac{E d^3 \sigma_{\pi^0}}{d^3 \vec{p}}$	4
ALICE [128]	2018	8000	η & π^0	$\frac{E d^3 \sigma_\eta}{d^3 \vec{p}} \Big/ \frac{E d^3 \sigma_{\pi^0}}{d^3 \vec{p}}$	13
ALICE [130]	2024	13000	η & π^0	$\frac{E d^3 \sigma_\eta}{d^3 \vec{p}} \Big/ \frac{E d^3 \sigma_{\pi^0}}{d^3 \vec{p}}$	14

TABLE VI: Same as Table I, but for η pp data. The kinematic variables in the observables are defined in Section II B 1, same as those for K_S^0 .

in ratios

$$\frac{E d^3 \sigma_\eta}{d^3 \vec{p}} \Big/ \frac{E d^3 \sigma_{\pi^0}}{d^3 \vec{p}}, \quad (11)$$

where E and \vec{p} are the energy and three momentum of the identified hadron, respectively. The predictions for π^0 production are calculated using the π^0 FFs constructed from π^\pm FFs determined in the previous NPC analysis [44] via isospin symmetry. The Hessian uncertainties of the constructed π^0 FFs are very small and can be omitted.

4. π^0 data

We have gathered a comprehensive dataset on π^0 production to validate the π^0 FFs derived from NPC23 π^\pm FFs [44]. These data are summarized in Table VII and Table VIII. In the context of SIA, we have incorporated measurements at the Z -pole from ALEPH [103, 131], DELPHI [132] L3 [119], and OPAL [120]. Additionally, we included jet measurements from ALEPH [103] and b -tagged data from DELPHI [132], which contribute to flavor separation as mentioned previously. The observables are normalized by the total hadronic cross section, expressed as $1/\sigma_h \times d\sigma/dx_p$, or by the jet cross section in the case of jet measurements, represented as $1/\sigma_{\text{jet}} \times d\sigma/dx_p$. We also included low-energy SIA measurements from JADE [121, 122], CELLO [133], TASSO [134], and ARGUS [125], spanning center-of-mass energies from 9.46 GeV to 44 GeV. The observables in this range are mostly given as $s/\beta \times d\sigma/dx_h$, except for TASSO, which provides a normalized cross section. The kinematic variables β , x_h and x_p the similar to those in the K_S^0 case, defined in Section II B 1.

For pp collisions, we have included data from the ALICE collaboration [126–128] at center-of-mass energies of 2.76, 7 and 8 TeV, as well as low-energy measurements from STAR [135] and PHENIX [136] at 200 GeV, and PHENIX [137] at 510 GeV. The relevant observable for pp collisions is the invariant cross section, $E d^3 \sigma / d^3 \vec{p}$, with E and \vec{p} being the energy and three momentum of the identified π^0 , respectively.

collaboration	year	\sqrt{s} [GeV]	final state	observable	N_{pt}
ARGUS [125]	1990	9.46	π^0	$\frac{s}{\beta} \frac{d\sigma}{dx_h}$	14
JADE [121]	1985	34.4	π^0	$\frac{s}{\beta} \frac{d\sigma}{dx_h}$	10
JADE [122]	1990	35	π^0	$\frac{s}{\beta} \frac{d\sigma}{dx_h}$	9
JADE [122]	1990	44	π^0	$\frac{s}{\beta} \frac{d\sigma}{dx_h}$	6
CELLO [123]	1990	35	π^0	$\frac{s}{\beta} \frac{d\sigma}{dx_h}$	15
TASSO [134]	1989	44	π^0	$\frac{1}{\sigma_h} \frac{d\sigma}{dx_p}$	6
ALEPH [131]	1997	91.2	π^0	$\frac{1}{\sigma_h} \frac{d\sigma}{dx_p}$	20
ALEPH [103]	2000	91.2	$\pi^0(\text{jet})$	$\frac{1}{\sigma_{\text{jet}}} \frac{d\sigma}{dx_h}$	8, 8 & 6
DELPHI [132]	1996	91.2	π^0	$\frac{1}{\sigma_h} \frac{d\sigma}{dx_p}$	17
DELPHI [132]	1996	91.2	$\pi^0(b\text{-tagged})$	$\frac{1}{\sigma_h} \frac{d\sigma}{dx_p}$	15
L3 [119]	1994	91.2	π^0	$\frac{1}{\sigma_h} \frac{d\sigma}{dx_p}$	12
OPAL [120]	1998	91.2	π^0	$\frac{1}{\sigma_h} \frac{d\sigma}{dx_h}$	10

TABLE VII: Same as Table I, but for π^0 SIA data. The kinematic variables in the observable are defined in Section II B 1, same as those for K_S^0 . For the ALEPH three-jet events measurement [103], the numbers of data points are listed respectively for π^0 production in three jets, ordered by jet energy.

collaboration	year	\sqrt{s} [GeV]	final state	observable	N_{pt}
STAR [135]	2010	200	π^0	$\frac{E d^3\sigma}{d^3\vec{p}}$	8
PHENIX [136]	2007	200	π^0	$\frac{E d^3\sigma}{d^3\vec{p}}$	17
PHENIX [137]	2016	510	π^0	$\frac{E d^3\sigma}{d^3\vec{p}}$	22
ALICE [127]	2017	2760	π^0	$\frac{E d^3\sigma}{d^3\vec{p}}$	16
ALICE [126]	2012	7000	π^0	$\frac{E d^3\sigma}{d^3\vec{p}}$	13
ALICE [128]	2018	8000	π^0	$\frac{E d^3\sigma}{d^3\vec{p}}$	24

TABLE VIII: Same as Table I but for π^0 pp data.

III. THEORETICAL INPUTS TO THE NPC23 ANALYSIS

In this section, we outline the parameterization of the NPC23 fit and summarize the details of theoretical computations.

A. Parametrization

The master formula for the parameterization for FFs is given by

$$zD_i^h(z, Q_0) = z^{\alpha_i^h} (1-z)^{\beta_i^h} \exp\left(\sum_{n=0}^m a_{i,n}^h z^{n/2}\right), \quad (12)$$

where the subscript i labels different parton flavors, the superscript h labels different hadron species. By varying $m = 0, 1, 2, \dots$, one can freely choose different parameterizations. In practice, we increase the value of m until no discernible improvement in fit quality can be obtained. $\{\alpha_i^h, \beta_i^h, a_{i,n}^h\}$ are the fitted parameters, and the initial scale is chosen as $Q_0 = 5$ GeV. We use a zero-mass scheme for heavy quarks and a number of flavors $n_f = 5$.

The parameterization choice for K_S^0 is summarized in Table IX. In total, there are 21 free parameters. The parameters for favored quark FFs are made symmetric between quark and antiquark as indicated in the K_S^0 wave function $\frac{1}{\sqrt{2}}(|d\bar{s}\rangle - |s\bar{d}\rangle)$. On the other hand, since K_S^0 is neutral, we assume the unfavored light as well as heavy quark distributions equal to the distributions of their antiquark correspondence. The same choice is made in BKK96 [79], AKK05 [80], AKK08 [67] and SAK20 [81]. SIA data sets alone cannot differentiate fragmentation from d and s quarks. The SIDIS data on K_S^0 production have poor quality and also show a slight preference for a larger distribution of the d quark than that of the s quark. This is counter-intuitive since s quark has a larger mass than that of d quark, thus the probability of creating a d quark from QCD vacuum should be higher than that of creating an s quark. We therefore included an empirical penalty term,

$$\left(D_s^{K_S^0}/D_d^{K_S^0} - 3\right)^2, \quad (13)$$

into the χ^2 to enforce an appropriate ratio of fragmentation probabilities from s and d quarks based on previous studies of suppression factors of strange quark [43]. We note that a separate H1 measurement [138] of K_S^0 production at relatively low momentum transfers reveals significant discrepancies with predictions from various MC predictions, indicating the possible influence of mechanisms beyond fragmentation processes.

flavor	favored	a_0	α	β	a_1
$u = \bar{u}$	✗	✓	✓	✓	✓
$d = \bar{d}$	✓	✓	$= \alpha_u$	✓	✓
$s = \bar{s}$	✓	✓	$= \alpha_u$	$= \beta_d$	$= a_{1,d}$
$c = \bar{c}$	✗	✓	✓	✓	✓
$b = \bar{b}$	✗	✓	✓	✓	✓
g	✗	✓	✓	✓	✓

TABLE IX: Summary of the parameterization for K_S^0 FFs. Check marks under “favored” represent the flavor is favored, while cross marks denote unfavored. Check marks under each parameter mean the parameter is free to vary. There are in total 20 free parameters for K_S^0 FFs.

In the context of Λ baryon, since the data are reconstructed from averaging between Λ and its antiparticle $\bar{\Lambda}$, the parameters are also made symmetric between quarks and antiquarks, with the gluon parameters still being independent. Moreover, the quark constituents of Λ is uds , and the masses of u and d are much smaller than that of Λ which is 1.115 GeV, we assume that the u and d FFs are identical. Finally, in the absence of sufficient constraints from existing world data, we fix the parameter a_1 to zero for the FFs of c and b quarks. The parameterization of Λ FFs is summarized in Table X.

In the context of η meson, following its wave function $|\eta\rangle = (|u\bar{u}\rangle + |d\bar{d}\rangle - 2|s\bar{s}\rangle)/\sqrt{6}$, we set the antiquark FFs to be equal to the corresponding quark FFs, *i.e.*, $D_q^\eta = D_{\bar{q}}^\eta$. Since η FFs are only weakly constrained, we set the shape parameters (α , β and a_1) of s to be equal to those of u , leaving the normalization parameter a_0 to vary. Again, the gluon parameters are independent from those of the quarks. Additionally, since no flavor tagged data is available for η , we also set $D_c^\eta = D_b^\eta$. The parameterization for η FFs is summarized in Table XI.

flavor	favored	a_0	α	β	a_1
$u = \bar{u} = d = \bar{d}$	✓	✓	✓	✓	✓
$s = \bar{s}$	✓	✓	✓	✓	✓
$c = \bar{c}$	✗	✓	✓	✓	✗
$b = \bar{b}$	✗	✓	✓	✓	✗
g	✗	✓	✓	✓	✓

TABLE X: Same table as Table IX, but for Λ FFs. There are in total 18 free parameters for Λ .

flavor	favored	a_0	α	β	a_1
$u = \bar{u} = d = \bar{d}$	✓	✓	✓	✓	✓
$s = \bar{s}$	✓	✓	$= \alpha_u$	$= \beta_u$	$= a_{1,u}$
$c = \bar{c} = b = \bar{b}$	✗	✓	✓	✓	✗
g	✗	✓	✓	✓	✓

TABLE XI: Same as Table IX, but for η FFs. The parameters α , β and a_1 of s are set to be equal to those of u , while a_0 is free to vary. There are in total 12 free parameters for η .

B. Theoretical computation method

The theoretical computation techniques have been summarized in the previous NPC23 work [44], here we only recall the key elements. In the NPC framework, the two-loop timelike splitting kernels are used to evolve the fragmentation functions to higher scales, matching the NLO accuracy. The splitting functions are given in [139] and are implemented with HOPPET [140, 141]. The hard kernels are computed with FMNLOv2.0 package [44, 46, 142] which implements processes including SIA, SIDIS and pp collisions. We adopt a zero-mass scheme for heavy quarks, with number of flavors $n_f = 5$ and $\alpha_s(m_Z) = 0.118$ throughout the fit. Here $m_Z = 91.18$ GeV is the mass of Z -boson, and α_s denotes the strong coupling.

The CT14 NLO parton distribution functions (PDFs) [143] are used in the generation of hard kernels for processes involving initial-state hadrons, *i.e.*, SIDIS and pp collisions. The central factorization, renormalization and fragmentation scales ($\mu_{F,0}$, $\mu_{R,0}$ and $\mu_{D,0}$) are chosen to be the transferred momentum Q for SIA and SIDIS, and to be transverse momentum of the identified final-state hadron for pp collisions, when it is applicable as summarized in Table XII. In the case of SIA jet production the central renormalization and fragmentation scales are set to the transferred momentum Q and the energy E_j of individual jet respectively. The scale variations are estimated by the half width of the envelope of theoretical predictions based on 9 scale combinations: $\mu_F/\mu_{F,0} = \mu_R/\mu_{R,0} = \{1/2, 1, 2\}$ and $\mu_D/\mu_{D,0} = \{1/2, 1, 2\}$. The covariance matrix of χ^2 calculations incorporates scale variations as theoretical uncertainties, assumed to be fully correlated among points within each subset of the data.

reaction	SIA	SIDIS	pp	SIA jet
$\mu_{F,0}$	–	Q	p_T	–
$\mu_{R,0}$	Q	Q	p_T	Q
$\mu_{D,0}$	Q	Q	p_T	E_j

TABLE XII: Central scale choices for single inclusive hadron production in SIA, SIDIS, and pp collisions, and hadron-in-jet production in SIA.

C. Goodness of fit function and the covariance matrix

We follow [144, 145] and quantify the goodness of fit with the likelihood function:

$$\chi^2(\{\alpha, \beta, a_i\}, \{\lambda\}) = \sum_{e,j} \frac{1}{s_{e,j}^2} \left(D_{e,j} - T_{e,j} - \sum_{k=1}^{N_e^{(\beta)}} \beta_{e,j,k} \lambda_{e,k} \right)^2 + \sum_e \sum_{k=1}^{N_e^{(\beta)}} \lambda_{e,k}^2, \quad (14)$$

where $\{\alpha, \beta, a_i\}$ and $\{\lambda\}$ are the set of fitted parameters and nuisance parameters, respectively. The indices e, j and k represent the experiment, data point, and various sources of correlated uncertainties, respectively. We also denote the number of correlated uncertainties in experiment e as $N_e^{(\beta)}$. The nuisance parameter $\lambda_{e,k}$ combined with $\beta_{e,j,k}$ controls the amount of additive shift coming from the k th correlated uncertainty at the j th data point in the experiment e . Furthermore, $D_{e,j}$ denotes the j th data value of the experiment e , and $T_{e,j}$ and $s_{e,j}$ are its corresponding theoretical prediction and uncorrelated uncertainty.

In practice, the values of $\{\lambda\}$ are determined by minimizing the likelihood function $\chi^2(\{\alpha, \beta, a_i\}, \{\lambda\})$ with respect to $\{\lambda\}$, which leads to the profiled χ^2 function [144]:

$$\chi^2(\{\alpha, \beta, a_i\}, \{\hat{\lambda}\}) = \sum_e \sum_{j,j'} (D_{e,j} - T_{e,j}) \mathcal{C}_{e,jj'}^{-1} (D_{e,j'} - T_{e,j'}) \quad (15)$$

where $\hat{\lambda}$ are the best fit nuisance parameters and \mathcal{C}_e^{-1} is the inverse of the covariance matrix \mathcal{C}_e :

$$\mathcal{C}_{e,jj'} \equiv s_{e,j}^2 \delta_{jj'} + \sum_{k=1}^{N_e^{(\beta)}} \beta_{e,j,k} \beta_{e,j',k}, \quad \mathcal{C}_{e,jj'}^{-1} = \frac{\delta_{jj'}}{s_{e,j}^2} - \sum_{k,k'=1}^{N_e^{(\beta)}} \frac{\beta_{e,j,k}}{s_{e,j}^2} A_{e,kk'}^{-1} \frac{\beta_{e,j',k'}}{s_{e,j'}^2}, \quad (16)$$

and $A_{kk'}$ is defined as [144]:

$$A_{e,kk'} \equiv \delta_{kk'} + \sum_j \frac{\beta_{e,j,k} \beta_{e,j,k'}}{s_j^2}. \quad (17)$$

Note that in this analysis we have included correlated uncertainties due to normalizations in experimental measurements as well as scale variations of the NLO calculations.

IV. THE NPC23 PREDICTIONS

In this section, we provide predictions to physical observables/quantities that are of interest. We first present the truncated moments which are related to the momentum sum rule of FFs. Then we provide predictions for the in-jet production of neutral hadrons at LHC kinematics. Finally, the case of kaon production is further studied in Section IV C using fitted K_S^0 FFs and constructed K_S^0 FFs via Eqs. (1) and (2), respectively. The difference in the resulting cross sections is significant, thus it is promising that measurement of such observables will help us further test the isospin symmetry in kaon fragmentation.

A. Moments and sum rules of FFs

The FFs represent the number density of finding a hadron inside its parent parton, and they satisfy the momentum sum rule. However, the satisfaction of momentum sum rule has been questioned recently in [146]. In our global analysis, we have the most comprehensive species of FFs, including charged hadrons π^\pm , K^\pm and p/\bar{p} [44], as well as neutral hadrons π^0 , K_S^0 , Λ and η from this work. In this section, we provide a test on the momentum sum rule utilizing results on FFs of neutral hadrons. Since the experimental data only constrain the FFs down to a finite z_{\min} , we define the truncated moments as:

$$\langle z \rangle_i^h = \int_{z_{\min}}^1 dz z D_i^h(z), \quad (18)$$

where i is the flavor of the parent parton and h is the final state of the identified hadron.

In Table XIII, we present the $\langle z \rangle_i^h$ for the neutral hadron FFs fitted in this work, *i.e.*, K_S^0 , Λ and η , as well as for the π^0 FFs which are constructed from the π^\pm FFs via isospin symmetry. The $\langle z \rangle_i^h$ values are computed with fixed $z_{\min} = 0.05$ for different parton flavors. The momentum fractions for $K_S^0 + K_L^0$ are obtained by multiplying the truncated moments of K_S^0 by a factor of two, and similarly, the total momentum fractions for $\Lambda + \bar{\Lambda}$ are twice of those for Λ .

hadron	$g (z_{\min} = 0.05)$	$d (z_{\min} = 0.05)$	$u (z_{\min} = 0.05)$	$s (z_{\min} = 0.05)$	$c (z_{\min} = 0.05)$	$b (z_{\min} = 0.05)$
$K_S^0 + K_L^0$	$0.0932^{+0.0058}_{-0.0037}$	$0.0857^{+0.0285}_{-0.0229}$	$0.0187^{+0.0057}_{-0.0053}$	$0.1586^{+0.0270}_{-0.0241}$	$0.1766^{+0.0116}_{-0.0108}$	$0.0696^{+0.0092}_{-0.0079}$
$\Lambda + \bar{\Lambda}$	$0.0357^{+0.0050}_{-0.0029}$	$0.0008^{+0.0007}_{-0.0005}$	$0.0008^{+0.0007}_{-0.0005}$	$0.0331^{+0.0071}_{-0.0056}$	$0.0323^{+0.0041}_{-0.0038}$	$0.0191^{+0.0047}_{-0.0039}$
η	$0.0192^{+0.0083}_{-0.0077}$	$0.0420^{+0.0092}_{-0.0068}$	$0.0420^{+0.0092}_{-0.0068}$	$0.1247^{+0.0189}_{-0.0174}$	$0.0119^{+0.0071}_{-0.0056}$	$0.0119^{+0.0071}_{-0.0056}$
π^0	$0.1577^{+0.0072}_{-0.0072}$	$0.1829^{+0.0076}_{-0.0065}$	$0.1829^{+0.0076}_{-0.0065}$	$0.1954^{+0.0160}_{-0.0156}$	$0.1674^{+0.0076}_{-0.0076}$	$0.1636^{+0.0060}_{-0.0057}$
sum	$0.3058^{+0.0134}_{-0.0115}$	$0.3113^{+0.0309}_{-0.0248}$	$0.2443^{+0.0133}_{-0.0108}$	$0.5119^{+0.0373}_{-0.0340}$	$0.3882^{+0.0161}_{-0.0149}$	$0.2642^{+0.0139}_{-0.0119}$

TABLE XIII: The total momentum fractions of parent partons carried by various final-state hadrons, including $K_S^0 + K_L^0$, $\Lambda + \bar{\Lambda}$, η and π^0 , are presented. The momentum fractions are defined in Eq. (18), with z_{\min} values listed in the first row of this table. The central values and Hessian uncertainties at 68% confidence level are computed from our nominal fit at $Q = 5$ GeV. The last row lists the sum for all hadrons in this table. Since the neutral hadron FFs are not correlated with each other, the uncertainties of the sum are determined by combining the uncertainties of individual hadrons in quadrature.

From the results presented in Table XIII, we observe that the listed neutral hadrons carry approximately 25% ~ 38% of the momentum from gluons, u quarks, d quarks, c quarks and b quarks. A notable feature is the large fraction of momentum carried by the neutral hadrons from the strange quark, which is roughly 51% of the total s quark momentum. Of this, both π^0 and $K_S^0 + K_L^0$ contribute dominantly, suggesting a significant role for these hadrons in the fragmentation of strange quark.

In Figs. 5 and 6, we present $\langle z \rangle_i^h$ as a function of z_{\min} for the neutral hadrons K_S^0 , Λ , η , and π^0 . The plots are organized such that in each subplot, the upper panels show results for the gluon, d quark, and u quark, while the lower panels display the results for the s quark, c quark, and b quark. In addition, to see the effect of QCD evolution, in each subplot we plot the truncated moments at two different scales. In the left panel we show results at $Q = 5$ GeV, and in the right panels for $Q = 100$ GeV. We extrapolate z_{\min} down to 0.001, and use the vertical lines to indicate the kinematic limit of data used in the analysis.

As shown in Fig. 5a, the truncated moments of K_S^0 saturate at $z_{\min} \approx 0.06$ at $Q = 5$ GeV. However, at $Q = 100$ GeV, the FFs are pushed toward smaller z and thus the truncated moments flatten at much smaller z_{\min} values. A similar

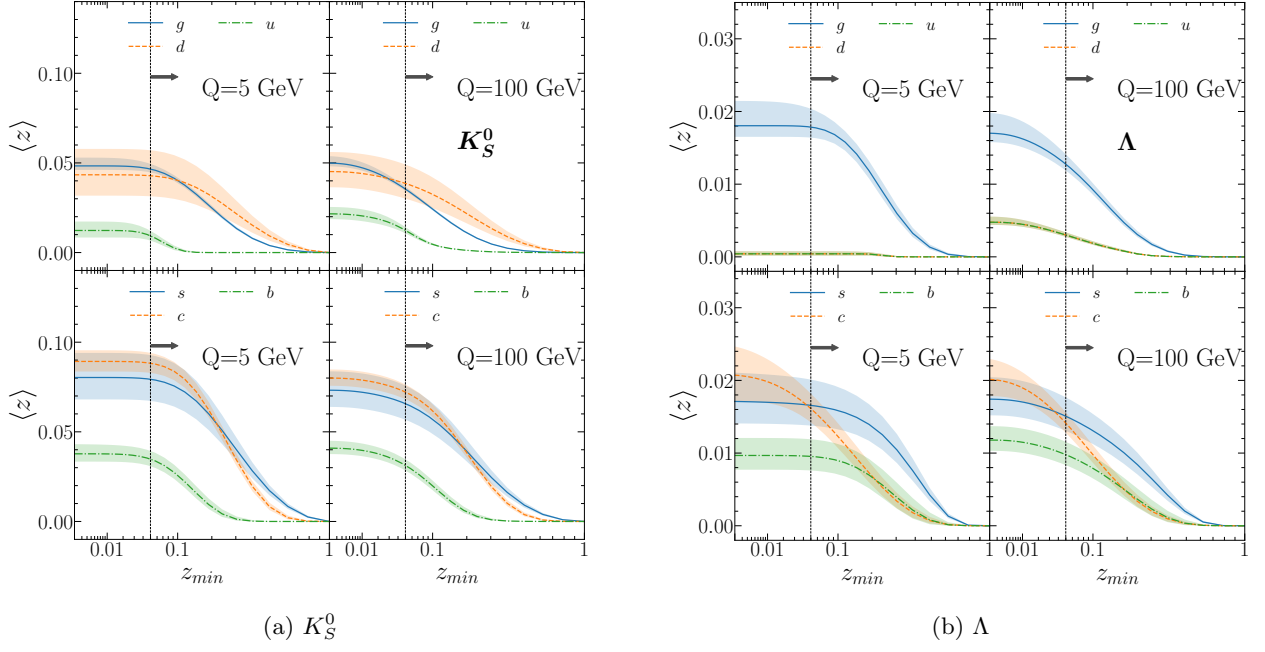


FIG. 5: Average momentum fraction carried by different neutral hadrons (K_S^0 and Λ) fragmented from various partons including u , d , s , c , b and g as a function of z_{\min} . Notice in this plot, instead of $K_S^0 + K_L^0$ or $\Lambda + \bar{\Lambda}$, we show the truncated moments for K_S^0 and Λ alone. In order to better visualize both ends of z_{\min} spectrum, we made the plot in $z_{\min}^{1/3}$ scale. The central values and uncertainties at 68% C.L. are calculated from our best-fit and Hessian error FFs at $Q = 5$ GeV and 100 GeV. The vertical lines indicate the kinematic coverage of experimental data.

behavior is also observed for Λ . The momentum sharing to K_S^0 for d and s quarks, as well as momentum sharing to Λ for gluon, s and b quarks are not well constrained by the data, indicating the need for future high-precision measurements.

In Fig. 6, the truncated moments for η and π^0 are presented. Since the η FFs from strange quark and gluon are not well constrained by data, they show relatively larger uncertainties at both $Q = 5$ GeV and $Q = 100$ GeV in Fig. 6a. Since we have set $D_u^\eta = D_d^\eta$ and $D_c^\eta = D_b^\eta$ in our fits, their curves overlap with each other. The η FFs from u , d , c and b quarks are relatively better constrained, thus their moments show smaller uncertainties. In the context of π^0 , the truncated moments saturate at $z_{\min} \approx 0.02$ at $Q = 5$ GeV, except for c and b which are not well constrained at small z values. At $Q = 100$ GeV, the π^0 FFs are pushed toward smaller z , and the saturation happens at a much smaller z_{\min} .

Finally, in Fig. 7 we present the momentum sum of all neutral hadrons from this work, as well as the momentum sum of both charged hadrons and neutral hadrons. From Fig. 7a, it can be seen that at the initial scale, the momentum sum of neutral hadrons for gluon and d , u , s quarks stabilizes at z_{\min} slightly above 0.01. In contrast, for c and b quarks, the momentum fractions continue to grow at $z_{\min} = 0.01$, although with large uncertainties. At $Q = 100$ GeV, again, all curves flatten at much smaller z_{\min} values. What is much more interesting is the total truncated moment of all available hadrons shown in Fig. 7b. These include π^\pm , K^\pm , $p + \bar{p}$, $K_S^0 + K_L^0$, $\Lambda + \bar{\Lambda}$, η and π^0 . We can see that these hadrons take approximately 80% ~ 90% of momentum from gluon, u and d quarks in the fragmentation. On the other hand, the total momentum fraction taken by these hadrons can exceed 100% for s , c and b quarks when extrapolated into small z_{\min} values, especially for the strange quark. This violation of the momentum sum rule could be due to the lack of constraints from the data. That includes, for example, the poor flavor separation concerning fragmentation from the d and s quarks, and the lack of data as small z . A definitive conclusion cannot be drawn at this point and will require future precision measurements, especially from future electron-ion colliders. In order to better visualize the numerical values of the truncated moments, in Table XIV we list the sum of truncated moments for the neutral hadron FFs from this work, the charged hadron FFs from the previous work [44], as well as the total sum for both neutral and charged hadron FFs.

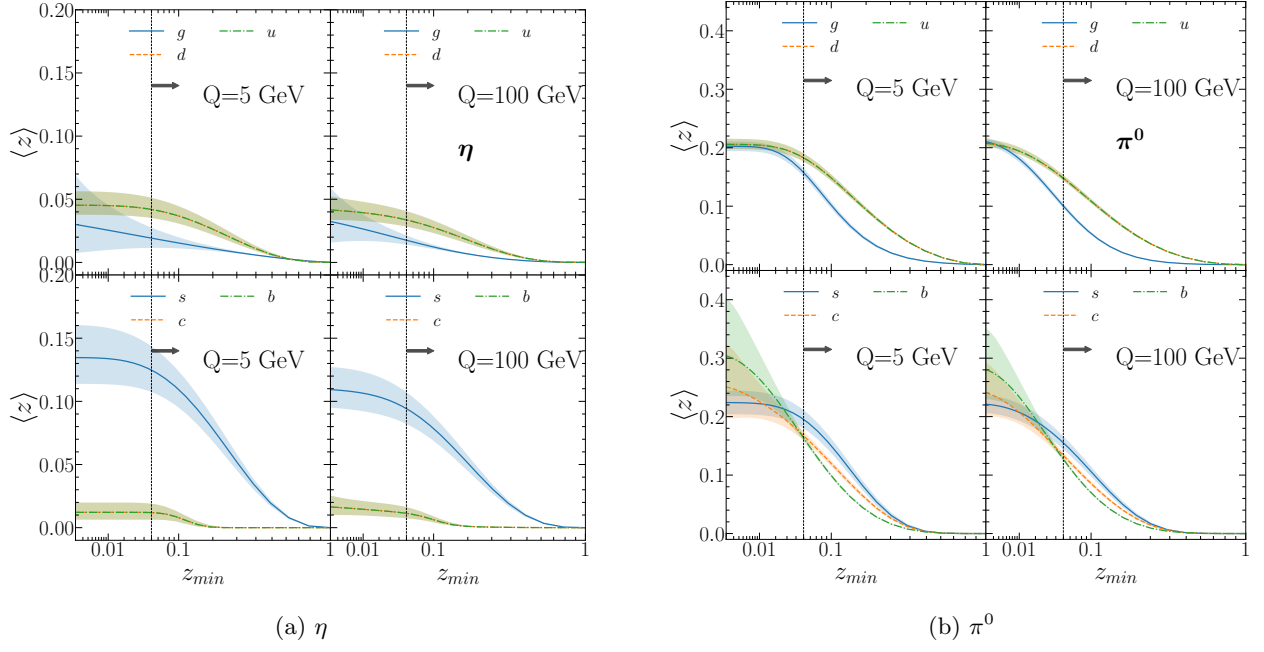


FIG. 6: Same as Fig. 5 but for η and π^0 . The spectra of u and d , as well as c and b in Fig. 6a completely overlap with each other because we have set $D_u^\eta = D_d^\eta$ and $D_c^\eta = D_b^\eta$ in our fits (see Section III A for more discussion).

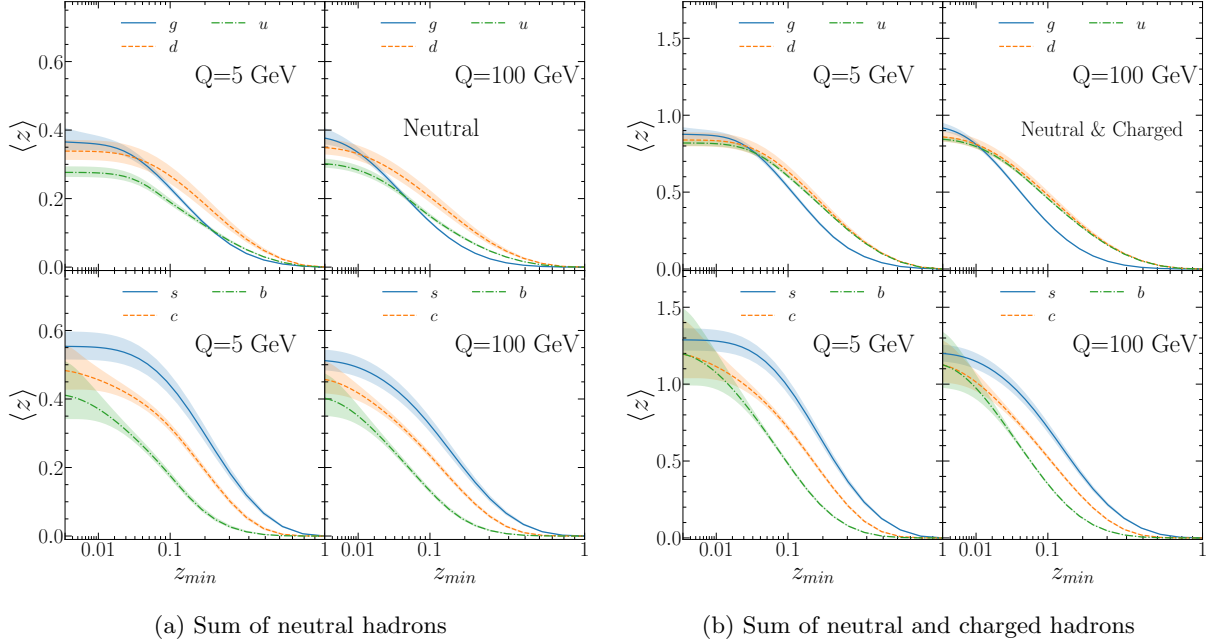


FIG. 7: Same as Fig. 5 but for sums of neutral hadrons, and for sums of charged hadrons from previous work [44] and neutral hadrons from this work.

hadron	$g (z_{\min} = 0.01)$	$d (z_{\min} = 0.01)$	$u (z_{\min} = 0.01)$	$s (z_{\min} = 0.01)$	$c (z_{\min} = 0.01)$	$b (z_{\min} = 0.01)$
neutral	$0.3587^{+0.0243}_{-0.0184}$	$0.3370^{+0.0322}_{-0.0256}$	$0.2749^{+0.0173}_{-0.0133}$	$0.5504^{+0.0424}_{-0.0377}$	$0.4561^{+0.0350}_{-0.0325}$	$0.3711^{+0.0465}_{-0.0376}$
charged	$0.5068^{+0.0145}_{-0.0133}$	$0.5066^{+0.0420}_{-0.0367}$	$0.5306^{+0.0150}_{-0.0135}$	$0.7293^{+0.0440}_{-0.0416}$	$0.6581^{+0.0655}_{-0.0572}$	$0.7033^{+0.0903}_{-0.0723}$
total	$0.8655^{+0.0306}_{-0.0251}$	$0.8436^{+0.0591}_{-0.0500}$	$0.8056^{+0.0214}_{-0.0171}$	$1.2797^{+0.0728}_{-0.0678}$	$1.1142^{+0.0974}_{-0.0868}$	$1.0744^{+0.1350}_{-0.1080}$

TABLE XIV: Same as Table XIII, but for sums of neutral FFs, charged FFs as well as all FFs available from previous [44] and current NPC works. In particular, the neutral hadrons included are $K_S^0 + K_L^0$, $\Lambda + \bar{\Lambda}$, η and π^0 , and the charged hadrons included are π^\pm , K^\pm and $p + \bar{p}$. The last row lists the sum of neutral and charged hadrons in this table. The π^0 FFs and all charged FFs are correlated with each other, hence their error sets are added together for computation of uncertainties.

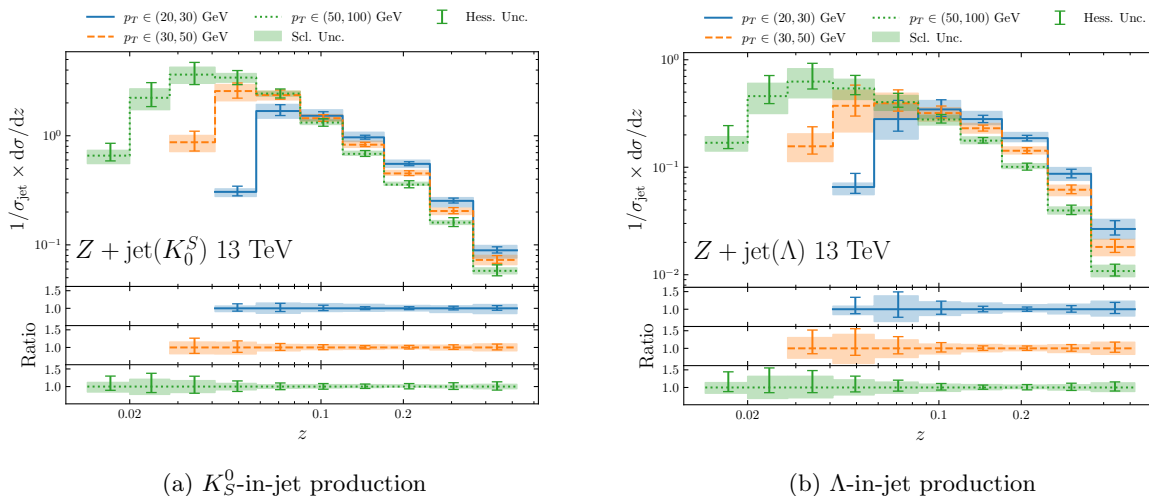


FIG. 8: Prediction of K_S^0 -in-jet and Λ -in-jet production in $pp \rightarrow Z + \text{jet}$ at LHCb kinematics with $\sqrt{s} = 13$ GeV. In the y -label, the σ_{jet} in the denominator represents the total $pp \rightarrow Z + \text{jet}$ cross section. The jet and Z -boson rapidity ranges are chosen respectively as $y_J \in (2.5, 4)$ and $y_Z \in (2, 4.5)$. The jet cone parameter is chosen as $R = 0.5$. Jets are detected with transverse momentum range $p_T \in (20, 30)$ GeV (blue), $p_T \in (30, 50)$ GeV (orange) and $p_T \in (50, 100)$ GeV (green). For all three different p_T ranges, the scale uncertainties are depicted with error bands, while the Hessian uncertainties are shown with error bars. In the lower three panels, the distributions, together with the uncertainties, are normalized to their corresponding central values. The cross sections and ratios are drawn with respect to the momentum fraction z of jet carried by the fragmented hadron.

B. Neutral hadrons in jet fragmentation

In this section, we provide predictions for hadron-in-jet production for $pp \rightarrow Z + \text{jet}$ at the LHCb. In particular, we follow the kinematics in Ref. [147] and set the center-of-mass energy to $\sqrt{s} = 13$ TeV. In addition, the rapidity ranges for the jet and Z -boson are set to $y_J \in (2.5, 4)$ and $y_Z \in (2, 4.5)$, respectively. The jet cone parameter is chosen as $R = 0.5$. The central values for the factorization scale and renormalization scale are set to half the sum of the transverse mass of all final state particles. The central value for the fragmentation scale is set to the transverse momentum of the jet. Differential cross sections in z are presented for three different jet transverse momentum p_T ranges, namely $(20, 30)$ GeV, $(30, 50)$ GeV and $(50, 100)$ GeV. The Z -boson transverse momentum $p_{T,Z}$ is chosen to be in the same range as the jet p_T , ensuring the back-to-back configuration. The hadron-in-jet cross sections, expressed as functions of the momentum fraction of the jet carried by the identified hadron, denoted as z , are predicted and presented in Figs. 8 and 9 for all neutral hadrons investigated in this study, *i.e.*, K_S^0 , Λ , η and π^0 .

In Fig. 8a, K_S^0 -in-jet production rate is shown for $pp \rightarrow Z + \text{jet}$ in a back-to-back configuration. Since an accurate prediction in the low hadron transverse momentum region requires resummation corrections that are beyond the scope of this work, we cut the hadron transverse momentum $p_{T,h} > 0.7$ GeV to exclude such scenarios. The curves for different p_T ranges exhibit behavior similar to that observed for the charged hadrons in Ref. [147]. Specifically, the production rates in different p_T ranges are nearly identical in the high- z region, with deviations becoming apparent as $z \lesssim 0.06$. This can be understood as a result of scaling violation, as z becomes lower, the TMD effects will start to play a more important role. For low p_T jets, the TMD effects appear earlier (at relatively larger z) than for jets with higher p_T . Another interesting observation is that the peak positions for K_S^0 -in-jet production are similar to those for K^\pm -in-jet production in [147], for each p_T range, respectively.

In Fig. 8b, Λ -in-jet production is predicted. Compared to the case of K_S^0 production, we observe that the theoretical uncertainties for Λ production are larger in the low z region. This indicates that the Λ FFs are less constrained at small z . Consequently, measurements in this region will contribute to improving the constraints on the Λ FFs.

In Fig. 9a, η -in-jet production is predicted. The Hessian uncertainty in this case is larger in the low z region, which again reflects the relatively less constrained η FFs. In this case, the scale uncertainty is smaller than that predicted for K_S^0 and Λ in Fig. 8. The scale uncertainties for K_S^0 and Λ are relatively larger due to the significant contribution of gluon distributions to the scale evolution. However, for η production, the gluon distribution is smaller than the light quark distributions in the region $z \gtrsim 0.1$, making the scale variation less pronounced. Additionally, the observable shown in Fig. 9a is normalized to the total $pp \rightarrow Z + \text{jet}$ cross section, further suppressing the scale uncertainty.

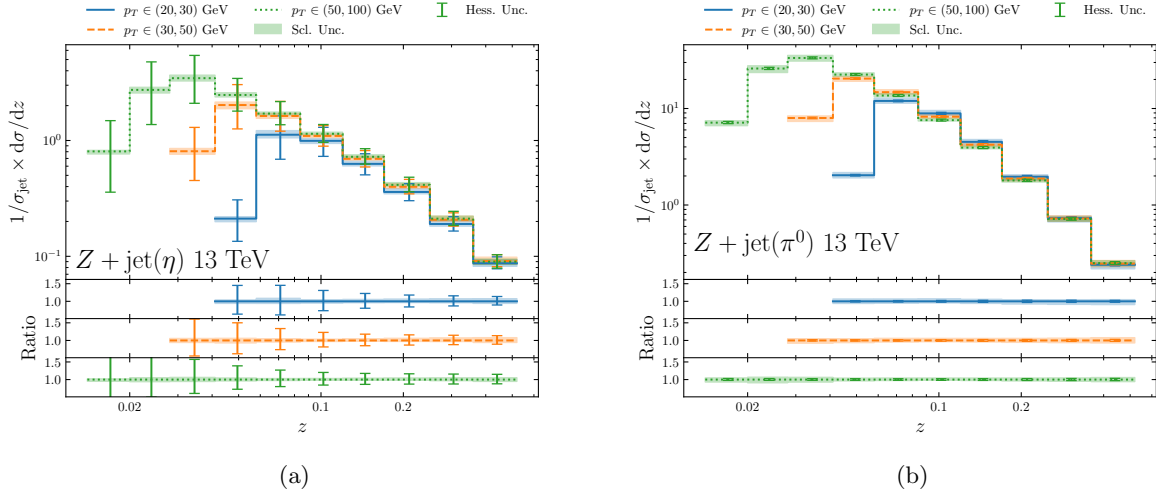


FIG. 9: Same as Fig. 8 but for η -in-jet and π^0 -in-jet production.

Finally, π^0 -in-jet production is predicted in Fig. 9b. Since the π^0 FFs are well constrained, the calculated observable has small uncertainties.

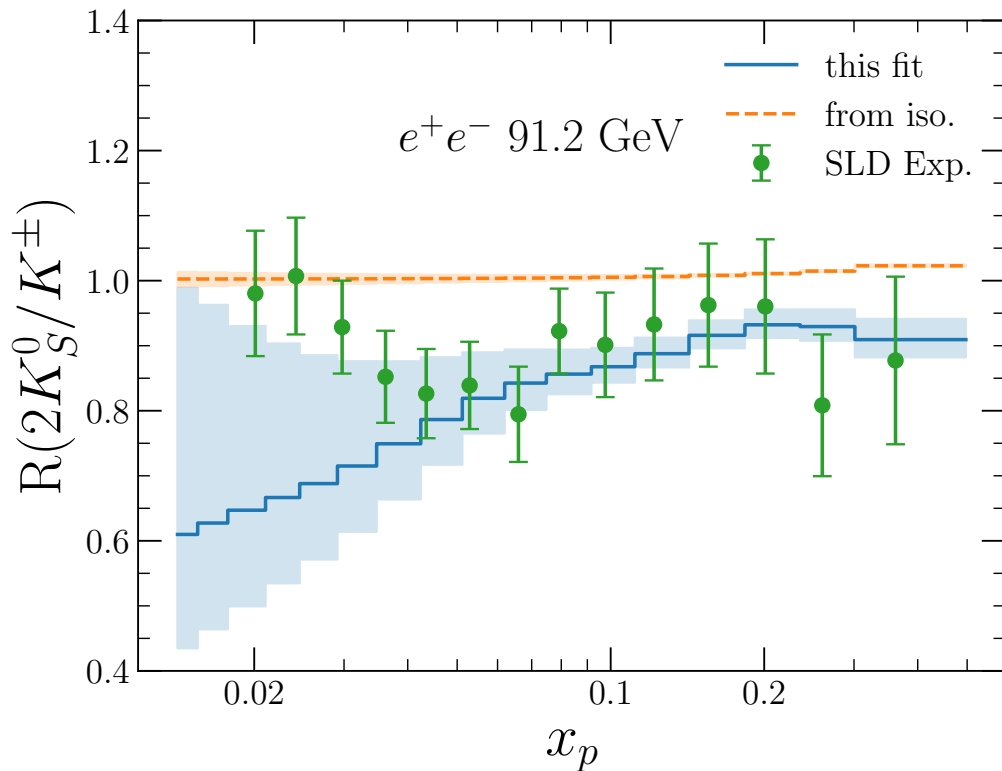


FIG. 10: Theoretical predictions of R_K^{fit} (blue) and R_K^{iso} (orange) in e^+e^- collisions at $\sqrt{s} = 91.2$ GeV. The green data points and error bars are provided by SLD measurement [87].

C. Ratios of neutral and charged kaon production

In this section, we provide predictions for K_S^0 over the K^\pm production rate:

$$R(2K_S^0/K^\pm) \equiv \frac{2d\sigma_{K_S^0}}{dx} \bigg/ \frac{d\sigma_{K^\pm}}{dx}, \quad (19)$$

where $x = x_p, z_p$ or p_T for SIA, SIDIS or pp collisions, respectively. Throughout this section, we adopt the abbreviated notation $R_K \equiv R(2K_S^0/K^\pm)$ in the main text for brevity. Here, the K^\pm production rate is calculated by the fitted K^\pm fragmentation functions [43], while the K_S^0 yield is based on either the K_S^0 FFs fitted in this work (with the observable denoted by R_K^{fit}) or the K_S^0 FFs constructed via isospin symmetry by Eqs. (1) and (2) (with the observable denoted by R_K^{iso}). In the following, we will illustrate the discrimination power of R_K in clarifying if the isospin symmetry in kaon FFs is violated, by comparing theoretical predictions R_K^{fit} with R_K^{iso} in SIA, SIDIS or pp collisions.

In Fig. 10, we provide the predictions of R_K^{fit} and R_K^{iso} as functions of x_p for SIA at the Z -pole, together with the results from the SLD measurement [87]. The K_S^0 FFs extracted in this work correctly reproduce the ratio in both high and intermediate x_p regions. In the low x_p region, although the theory prediction and data are consistent within uncertainties, their central values deviate substantially from each other. On the other hand, the K_S^0 FFs constructed via isospin symmetry predict a ratio R_K^{iso} that is close to unity across the entire x_p range. To comprehend this phenomenon, we begin by recognizing that the constructed $2 \times K_S^0$ FFs and K^\pm FFs differ solely by an interchange of the u and d quark distributions. Additionally, the parton-level production rates of u and d quarks are similar at the Z -pole. These factors result in R_K^{iso} being very close to unity. Although moderate tension is observed between R_K^{iso} and the SLD measurement around $x_p \sim 0.05$, it is not sufficient to conclude the violation of the isospin symmetry in kaon fragmentation. In Fig. 11, we present the predictions for R_K^{fit} and R_K^{iso} at $\sqrt{s} = 10.52$ GeV, together with the Belle measurement at the same energy scale [148]. We observe that R_K^{fit} and R_K^{iso} roughly describe the Belle data equally well in the region $0.2 < x_p < 0.8$. In the large x_p region, the K_S^0 FFs are not well constrained. In the small x_p region, there is tension between K_S^0 FFs fitted in this work and the Belle measurement, which is not included in our K_S^0 fit.

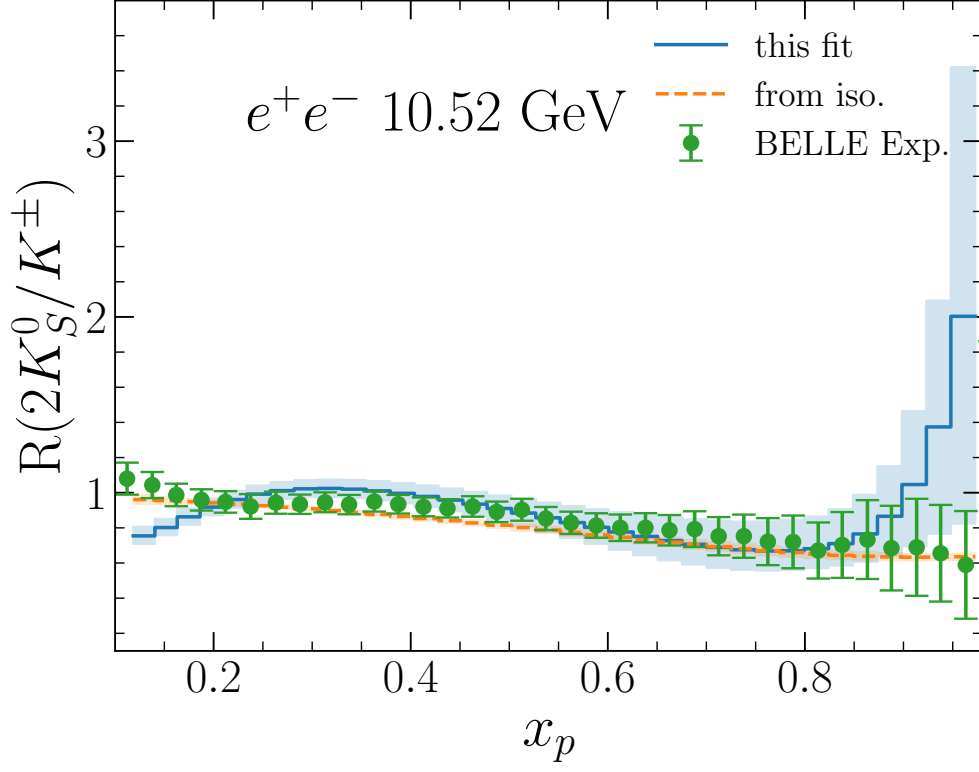


FIG. 11: Same as Fig. 10 but at Belle kinematics with $\sqrt{s} = 10.52$ GeV. The data points are taken from Ref. [148].

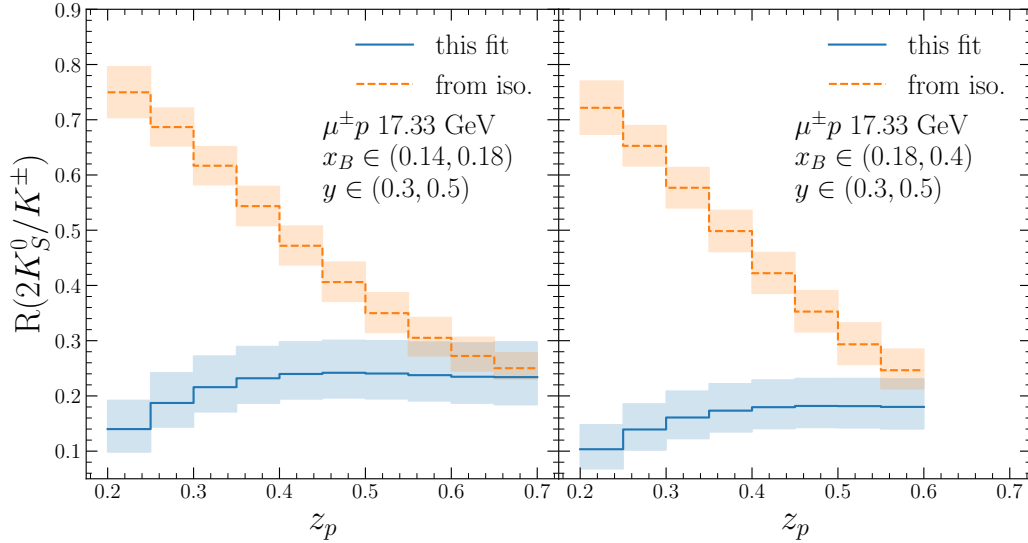


FIG. 12: Same as Fig. 10 but for SIDIS off a proton target at COMPASS kinematics with $\sqrt{s} = 17.33$ GeV. The variables x_B and y denote the Bjorken- x variable and event inelasticity, respectively. The cross section is differential in z_p . The variables x_B , y and z_p are all defined in Section II B 1.

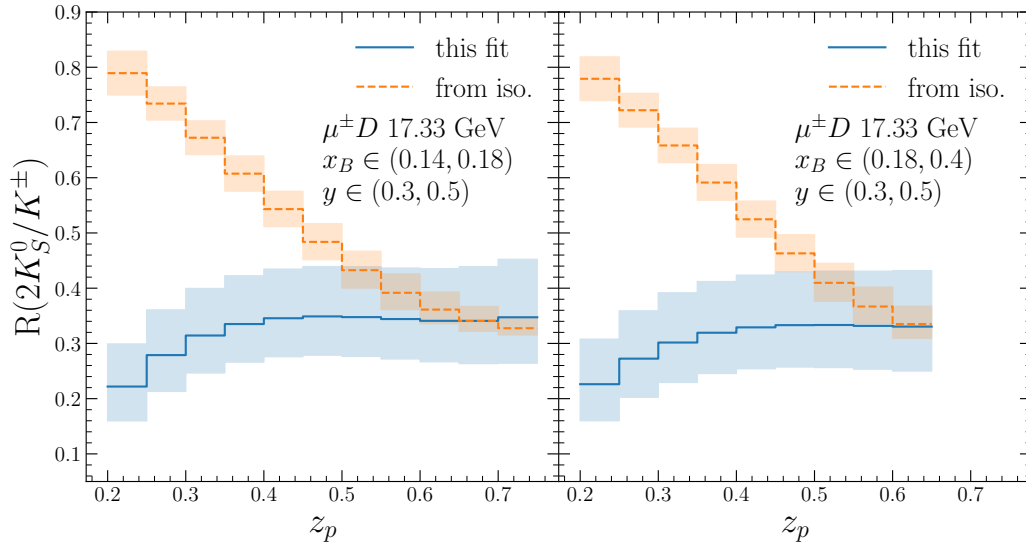


FIG. 13: Same as Fig. 12 but for SIDIS off a deuteron target.

In Fig. 12, we present the predicted R_K^{fit} and R_K^{iso} , as a function of z_p , for SIDIS off a proton target with COMPASS kinematics. In particular, the center-of-mass energy is set to $\sqrt{s} = 17.33$ GeV, the x_B ranges are set to (0.14, 0.18) and (0.18, 0.4) for the left and right panels, respectively. Finally, the event inelasticity y range is (0.3, 0.5) for both panels. Although the prediction is still at relatively low \sqrt{s} , the two curves (blue and orange) are well separated from each other, unlike what is observed in Fig. 11. This is because the SIDIS process has the advantage for flavor separation, which contributes to the discrimination between the two scenarios. Similar behavior is observed in Fig. 13 for SIDIS off a deuteron target in the same kinematic region. Future SIDIS measurements on K_S^0 production, especially in the middle and small z_p regions, can be essential to test the isospin symmetry in kaon FFs.

In Fig. 14, the ratios R_K^{fit} and R_K^{iso} are presented as functions of the transverse momentum of the identified hadron for inclusive hadron production in pp collisions. Following ALICE kinematics [108], we set $\sqrt{s} = 13$ TeV and the hadron rapidity range as $(-0.5, 0.5)$. The orange curve, which is plotted from the K_S^0 FFs constructed by isospin symmetry, remains close to unity. In contrast, the theoretical predictions based on the fitted K_S^0 FFs (blue) deviate slightly from unity and exhibit larger uncertainties.

Since hadron-in-jet production measurements provide a direct probe of FFs as a function of z , we also present predictions of the ratio between $pp \rightarrow Z + \text{jet}(K_S^0)$ and $pp \rightarrow Z + \text{jet}(K^\pm)$ in Fig. 15. We follow Section IV B and set the kinematics according to the LHCb measurement [147] at 13 TeV. The predictions for R_K^{fit} and R_K^{iso} are provided in three jet p_T bins, *i.e.*, $p_T \in (20, 30)$ GeV, $p_T \in (30, 50)$ GeV and $p_T \in (50, 100)$ GeV. Here again, the Z -boson $p_{T,Z}$ ranges and the jet p_T ranges are set to be identical in order to maintain the back-to-back configuration. This ratio observable clearly serves a better role in distinguishing the K_S^0 FFs fitted from global datasets (blue) and the K_S^0 FFs constructed from isospin symmetry (orange).

In summary, in this section predictions for the ratio of production rates of K_S^0 and K^\pm in SIA, SIDIS and pp collisions are presented. We find that future measurements of the proposed observable, especially for SIDIS or for hadron-in-jet production, demonstrate significant potential for testing isospin symmetry in kaon fragmentations.

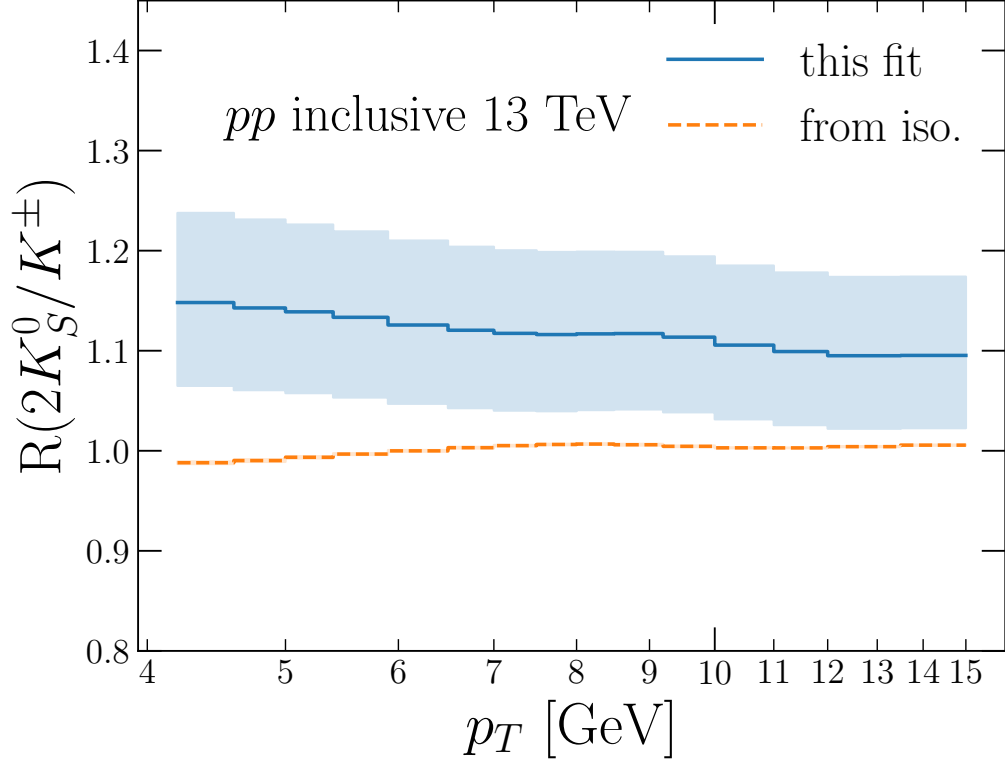


FIG. 14: Same as Fig. 10 but for inclusive hadron production in pp collisions at ALICE kinematics with $\sqrt{s} = 13$ TeV. The ratios are drawn as functions of hadron transverse momentum p_T .

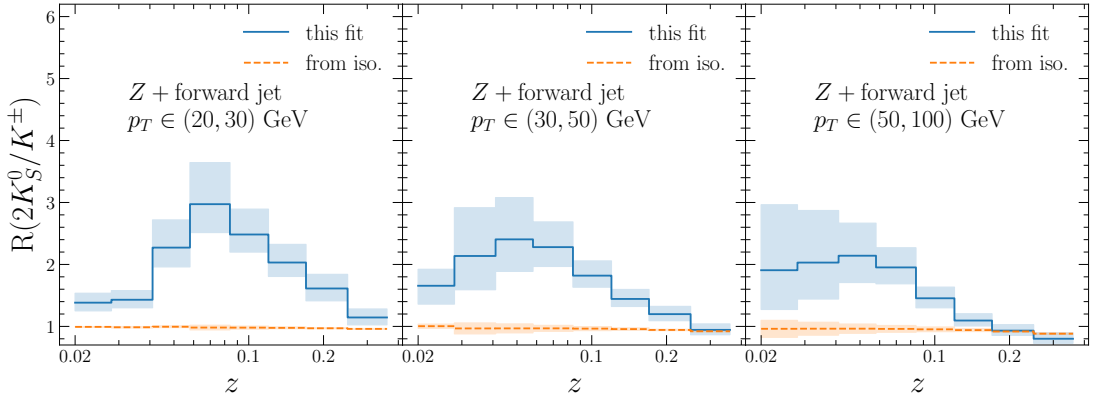


FIG. 15: Same as Fig. 10 but for hadron-in-jet production in $pp \rightarrow Z + \text{jet}$ at LHCb kinematics with $\sqrt{s} = 13$ TeV. The kinematics used in this figure are the same as those used in Fig. 8.

V. QUALITY OF FIT TO DATA

In this section, we present the predictions of FMNLO-nominated FFs compared to the experimental data. The quality of fit to K_S^0 , Λ and η data is discussed in dedicated sections. Furthermore, the quality of predictions for the π^0 data using the FFs constructed from the π^\pm FFs via isospin symmetry is also discussed. Overall, a good description is found for all hadron productions, with a few exceptions that will be pointed out.

A. K_S^0 production

In Table XV, we present the χ^2 values together with the corresponding χ^2/N_{pt} values for each experimental dataset, comparing our best-fit predictions with the experimental measurements. Furthermore, we provide the sum of the χ^2 values for the SIA, SIDIS, pp collisions, and the total fitted datasets to give an overall perspective on the fit quality across these different categories. The global fit to all datasets yields a total χ^2 of 304.68 for 314 data points, giving a χ^2/N_{pt} value of 0.97, signifying solid agreement between the theoretical predictions and the measured data. For the SIA datasets, the overall χ^2/N_{pt} is 1.03 for 277 data points, showing a generally good match between theory and experiment. However, some datasets show larger discrepancies, such as the TASSO 1990 dataset [99] at 42.6 GeV with χ^2/N_{pt} of 2.58 and HRS 1987 dataset [100] at 29 GeV with χ^2/N_{pt} of 2.76. While the HRS data was generally not well fitted in previous analyses [67, 81, 82], the TASSO 42.6 GeV data was well fitted in AKK05 [80], AKK08 [67], SAK20 [81] and FF24 [83]. Additionally, the SLD c -tagged data [87] has a relatively large $\chi^2/N_{\text{pt}} = 1.94$ and this is due to the few outliers of the data (see Fig. 16). For the SIDIS data, the agreement between theory and data is also very good, showing a χ^2/N_{pt} of 0.87 over 12 data points. The pp collision data also aligns well between theory and experiment, with a χ^2/N_{pt} of 0.35 over 25 data points. In general, most datasets are well described by theoretical predictions, with the majority of χ^2/N_{pt} values close to 1, indicating a successful fit, despite a few cases where larger deviations arise.

Fig. 16 presents comparisons between theoretical predictions and experimental data for K_S^0 production in SIA at the Z -pole, including measurements from OPAL [91–93], SLD [87], ALEPH [94, 103] and DELPHI [95] collaborations. The figure presents twelve panels with all results normalized to our best-fit predictions. Scale uncertainties and Hessian uncertainties are represented by blue and orange bands, respectively. The OPAL measurements from 1991 [91], 1995 [92] and 2000 [93] show agreement with theoretical predictions throughout the x_h range, with some fluctuations in the intermediate x_h region, but generally within experimental uncertainties. For SLD measurements [87], three different datasets are presented: inclusive, c -tagged and b -tagged events. The c -tagged and b -tagged measurements show larger Hessian uncertainties compared to the inclusive case, reflecting the relatively weak constraint of the data caused by the large experimental uncertainties. The ALEPH data from 1998 [94] and 2000 [103] are well described by the theory. Although a slightly upward trend in the high- x_h region is observed, it remains within the experimental uncertainties. The DELPHI 1994 [95] data points are notably consistent with theoretical predictions and show small experimental uncertainties throughout the measured x_h range. The last column of Fig. 16 shows the prediction of ALEPH three-jet data [103], respectively, for jet 1, 2, and 3. It is noticed that the scale uncertainties now become discernible. This is attributed to the fact that in the jet production process, α_s enters at tree level, and thus scale variation via running of the strong coupling constant can contribute at leading order (LO).

Fig. 17 shows a comparison between theoretical predictions and experimental data for K_S^0 production in SIA with a center-of-mass energy below Z mass, with all results normalized to our best-fit predictions. The figure consists of thirteen panels, among them the first two rows show TASSO data-theory agreement with center-of-mass energies ranging from 14 to 42.6 GeV [98, 99], while the remaining panels present TPC [96], HRS [100], MARK II [97], CELLO [101] and TOPAZ [102] measurements. The values and uncertainties are displayed the same way as in Fig. 16. For most TASSO measurements, the data points show relatively larger fluctuations around the theoretical predictions, particularly in the high- x_h region, but the theory is in general within experimental uncertainties. The measurements from TPC [96] at 29 GeV are well described by our theoretical predictions. For HRS [100] and MARK II [97] measurements at 29 GeV, the data exhibits some fluctuations around the theory predictions, but are generally within the experimental uncertainties. The CELLO measurement [101] at 35 GeV has larger experimental uncertainties, particularly at high x_h , yet a good description is still achieved. The TOPAZ data [102] is measured at 58 GeV, with four points in the low x_h region, and they show good agreement with the theoretical predictions.

Fig. 18 presents comparisons between theoretical predictions and SIDIS measurements from ZEUS [85] for K_S^0 production in three different Q^2 ranges: (160, 640) GeV^2 , (640, 2560) GeV^2 and (2560, 10240) GeV^2 . For the lowest Q^2 range, (160, 640) GeV^2 , the theoretical predictions show excellent agreement with data across the entire x_h range, with experimental uncertainties generally comparable to or smaller than the theoretical uncertainties. In the intermediate Q^2 range, (640, 2560) GeV^2 , the data exhibits larger fluctuations around the theory predictions, particularly in the high- x_h region, though the theory values generally remain within the experimental uncertainties. For the highest

collaboration	year	\sqrt{s} [GeV]	χ^2	N_{pt}	χ^2/N_{pt}
TASSO [98]	1985	14	5.65	9	0.63
TASSO [98]	1985	22	5.87	6	0.98
TASSO [98]	1985	34	16.03	13	1.23
TASSO [99]	1990	14.8	12.56	9	1.40
TASSO [99]	1990	21.5	3.78	6	0.63
TASSO [99]	1990	34.5	17.51	13	1.35
TASSO [99]	1990	35	14.76	13	1.14
TASSO [99]	1990	42.6	33.60	13	2.58
TPC [96]	1984	29	2.75	8	0.34
MARK II [97]	1985	29	12.65	17	0.74
HRS [100]	1987	29	33.16	12	2.76
CELLO [101]	1990	35	2.71	9	0.30
TOPAZ [102]	1995	58	0.29	4	0.07
OPAL [91]	1991	91.2	7.75	7	1.11
OPAL [92]	1995	91.2	13.63	16	0.85
OPAL [93]	2000	91.2	8.62	16	0.54
ALEPH [94]	1998	91.2	6.39	16	0.40
ALEPH [103]	2000	91.2	12.72	14	0.91
ALEPH jet 1 [103]	2000	91.2	14.91	12	1.24
ALEPH jet 2 [103]	2000	91.2	8.21	13	0.63
ALEPH jet 3 [103]	2000	91.2	8.55	11	0.78
DELPHI [95]	1995	91.2	7.55	13	0.58
SLD [87]	1999	91.2	7.39	9	0.82
SLD c -tagged [87]	1999	91.2	17.44	9	1.94
SLD b -tagged [87]	1999	91.2	11.12	9	1.24
SIA sum			285.60	277	1.03
ZEUS $Q^2 \in (160, 640) \text{ GeV}^2$ [85]	2012	318	4.41	5	0.88
ZEUS $Q^2 \in (640, 2560) \text{ GeV}^2$ [85]	2012	318	3.26	5	0.65
ZEUS $Q^2 \in (2560, 10240) \text{ GeV}^2$ [85]	2012	318	2.74	2	1.37
SIDIS sum			10.41	12	0.87
ALICE $(N_{K_S^0}^{13 \text{ TeV}}/N_{K_S^0}^{7 \text{ TeV}})$ [108]	2021	13000 & 7000	2.88	10	0.29
ALICE $(N_{K_S^0}/N_{\pi^\pm})$ [108]	2021	13000	5.79	15	0.39
pp sum			8.67	25	0.35
total sum			304.68	314	0.97

TABLE XV: The χ^2 , number of data points (N_{pt}) and χ^2/N_{pt} for the global datasets of K_S^0 production. Additional details, including information on collaboration, the year of publication, and center-of-mass energy, are also provided. Sum of χ^2 is also given for SIA, SIDIS and pp collision subgroups, as well as for grand total of all datasets.

Q^2 range, (2560, 10240) GeV^2 , the prediction and data show larger deviations. However, due to the relatively larger experimental uncertainties, the theoretical values remain roughly within the 1σ region. Both scale and Hessian uncertainties are relatively stable across all three Q^2 ranges and the entire x_h range. Finally, we elaborate on the results related to the lowest Q^2 -bin data. During iteration of the fits, we observe that without the penalty term described in Eq. (13), this particular dataset favors a d distribution that is slightly larger than the s distribution, which is unphysical. In accordance with the physics considerations discussed in Section III A, we included the aforementioned penalty term in order to correct this behavior. As a result, the s distribution becomes larger than that of d and the increase in χ^2 is only marginal (total $\Delta\chi^2 = 3.66$ for a total of 314 data points, and $\Delta\chi^2 = 2.17, 1.13$ for

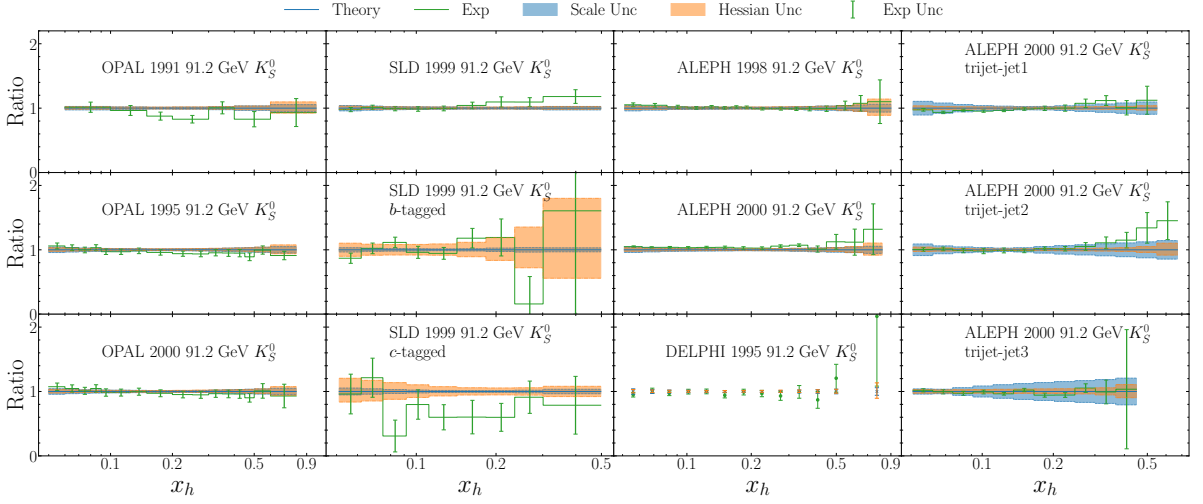


FIG. 16: The data over theory plot for K_S^0 production in SIA at Z -pole energy. The x -axis is plotted in logarithmic scale for x_h defined in Section II B 1. The data and experimental uncertainties are shown in green error bars, while the scale and Hessian uncertainties are shown in blue and orange bands, respectively. The data, scale and Hessian uncertainties are normalized to our best-fit theory values.

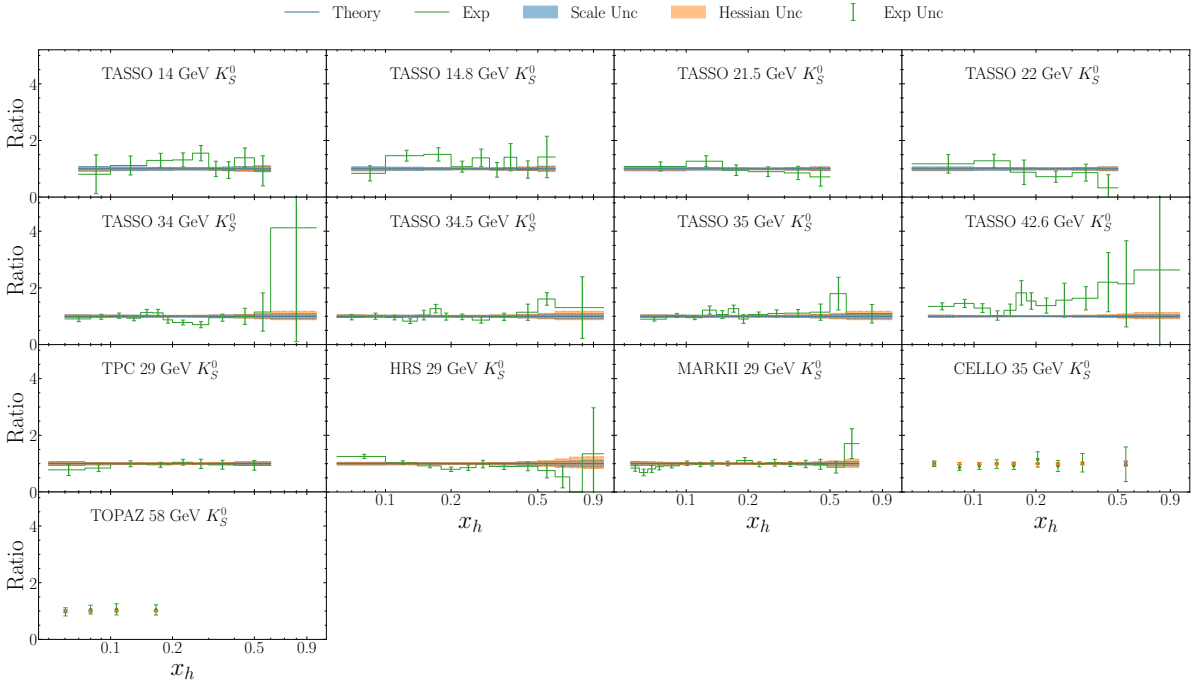


FIG. 17: Same as Fig. 16 but for K_S^0 production in SIA below Z -pole energy.

ZEUS at $Q^2 \in (160, 640) \text{ GeV}^2$ and HRS at 29 GeV, respectively). Although in the NPC23 nominal results, the d and s distributions follow the physical picture, we emphasize that to achieve flavor separation between the d and s distributions purely based on data, more precise SIDIS measurements are still needed.

In Fig. 19 the comparisons between the theoretical predictions and the ALICE measurements [108] are shown. The data in the left panel is the ratio of K_S^0 production cross sections between $\sqrt{s} = 13 \text{ TeV}$ and $\sqrt{s} = 7 \text{ TeV}$, while the data in the right panel is the ratio of K_S^0 production to π^\pm production at $\sqrt{s} = 13 \text{ TeV}$. In the left panel, the theoretical predictions are slightly larger than the data across the entire p_T range, though the theoretical values are

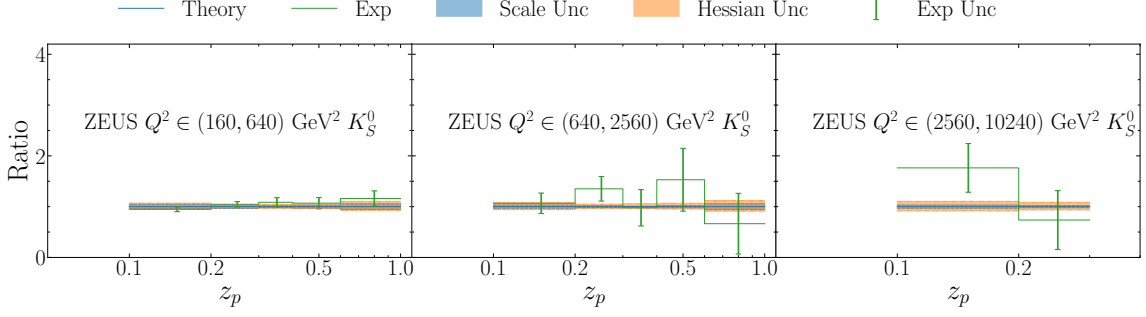


FIG. 18: Same as Fig. 16 but for K_S^0 production in SIDIS process. The ranges of photon virtuality, Q^2 , are also labeled in each panel.

generally within the experimental uncertainties. This indicates a tension between the ALICE K_S^0 production ratio data (13 TeV / 7 TeV) and the other world data, and further measurements could help us better understand it. The scale uncertainties are larger than the Hessian uncertainties in the low- p_T region and decrease with increasing p_T . This is caused by the fact that the running of strong coupling constant is more steep at lower scales. On the other hand, the Hessian uncertainties remain relatively stable across the entire p_T range. For the K_S^0/π^\pm ratio data at $\sqrt{s} = 13$ TeV, which is compared to the theoretical prediction in the right panel, good agreement between theory and data is observed at low and intermediate p_T values. However, some fluctuations are observed in the high- p_T region and this is understood as a result of the lower statistics when p_T gets larger. Both scale and Hessian uncertainties are relatively small for this observable, with scale uncertainties slightly more prominent in the low- p_T region.

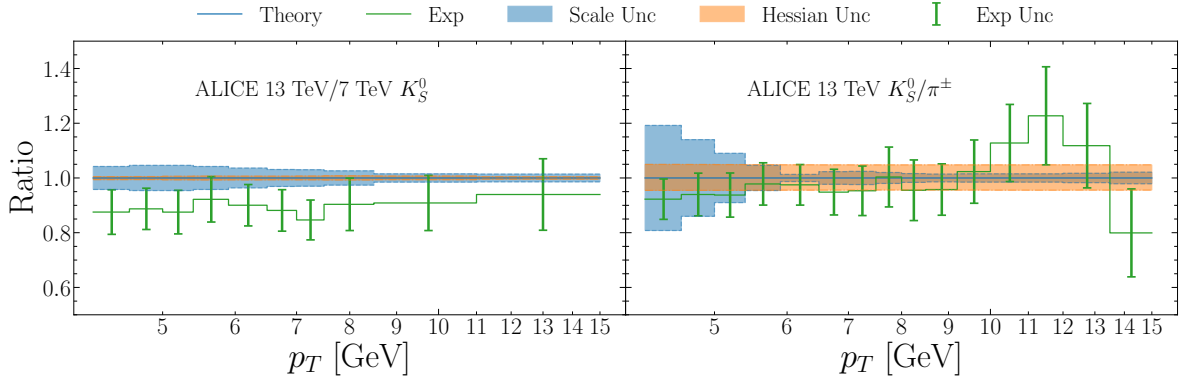


FIG. 19: Same as Fig. 16 but for K_S^0 production in pp collisions. The first panel shows the data-theory comparison for the ALICE data of K_S^0 production ratio between $\sqrt{s} = 13$ TeV and $\sqrt{s} = 7$ TeV. The second panel shows the data-theory comparison for the data of K_S^0 production over π^\pm production at $\sqrt{s} = 13$ TeV.

collaboration	year	\sqrt{s} [GeV]	χ^2	N_{pt}	χ^2/N_{pt}
TASSO [98]	1985	14	1.45	3	0.48
TASSO [98]	1985	22	2.93	4	0.73
TASSO [98]	1985	34	3.95	7	0.56
SLAC [112]	1985	29	19.16	15	1.28
HRS [100]	1987	29	5.57	8	0.70
CELLO [101]	1990	35	3.49	7	0.50
DELPHI [109]	1993	91.2	9.58	7	1.37
ALEPH [110]	1994	91.2	7.40	14	0.53
ALEPH [94]	1998	91.2	4.43	16	0.28
ALEPH jet 1 [103]	2000	91.2	16.50	13	1.27
ALEPH jet 2 [103]	2000	91.2	3.08	12	0.26
ALEPH jet 3 [103]	2000	91.2	3.72	9	0.41
OPAL [111]	1997	91.2	5.83	12	0.48
SLD [87]	1999	91.2	8.08	9	0.90
SLD c -tagged [87]	1999	91.2	13.96	4	3.49
SLD b -tagged [87]	1999	91.2	0.75	4	0.19
SIA sum			109.88	144	0.76
ZEUS $Q^2 \in (160, 640)$ GeV ² [85]	2012	318	14.44	5	2.89
ZEUS $Q^2 \in (640, 2560)$ GeV ² [85]	2012	318	1.26	3	0.42
ZEUS $Q^2 \in (2560, 10240)$ GeV ² [85]	2012	318	0.01	1	0.01
SIDIS sum			15.70	9	1.74
CMS ($N_\Lambda/N_{K_S^0}$) [115]	2011	900	2.99	4	0.75
ALICE ($N_\Lambda^{13 \text{ TeV}}/N_\Lambda^7 \text{ TeV}$) [108]	2021	13000 & 7000	1.59	7	0.23
pp sum			4.58	11	0.42
total sum			130.16	164	0.79

TABLE XVI: Same as Table XV but for Λ production data.

B. Λ production

In Table XVI, we present the χ^2 , χ^2/N_{pt} values and summary for different categories similar to that in the K_S^0 fit. In summary, we have obtained a good fit with total $\chi^2/N_{\text{pt}} = 0.79$. For individual processes, a good description is found for SIA and pp collisions, each giving a χ^2/N_{pt} of 0.76 and 0.42, respectively. However, for SIDIS data, the description is slightly worse with $\chi^2/N_{\text{pt}} = 1.74$. This is caused by the large $\chi^2/N_{\text{pt}} = 2.89$ from the ZEUS measurement [85] in the Q^2 bin of (160, 640) GeV², and it will be discussed later in this section.

In Fig. 20 we show the data-theory comparison for Λ production in the SIA process at the Z -pole, including measurements from DELPHI [109], ALEPH [94, 103, 110], OPAL [111] and SLD [87] collaboration. The experimental data and their uncertainties, as well as the theoretical uncertainties (scale and Hessian), are normalized to our best-fit theoretical results. The comparison with ALEPH 1994 [110] and ALEPH 1998 [94] data is given in the first two panels in column 1. A good agreement between theory and data is found, with reasonable scale and Hessian uncertainty bands. The Hessian uncertainty becomes larger at the high- x_h end, reflecting the growth of experimental uncertainties. The comparison to ALEPH 2000 Λ -in-jet data [103] is shown in column 2 of Fig. 20, for jet 1, 2 and 3 from the top to bottom panels, respectively. A good description is also found for all three cases, with some fluctuations in the high- x_h region. This can be understood as a result of the decreasing experimental precision with lower statistics in the high x_h region. Similarly to the case of the ALEPH K_S^0 -in-jet production data shown in Fig. 16, the scale uncertainties for the Λ -in-jet production are discernibly larger compared to other scenarios. Again, this is caused by the fact that α_s enters at LO for jet production (see comments on Fig. 16). As for the SLD 1999 data [87], shown in the third panel of Fig. 20, we find a good description for both inclusive and b -tagged Λ productions. The exception is for the SLD c -tagged data, which has a χ^2/N_{pt} of 3.49. This is caused by the second point which is an outlier. Larger Hessian uncertainties are also observed in c/b -tagged scenarios, this reflects the relatively larger experimental

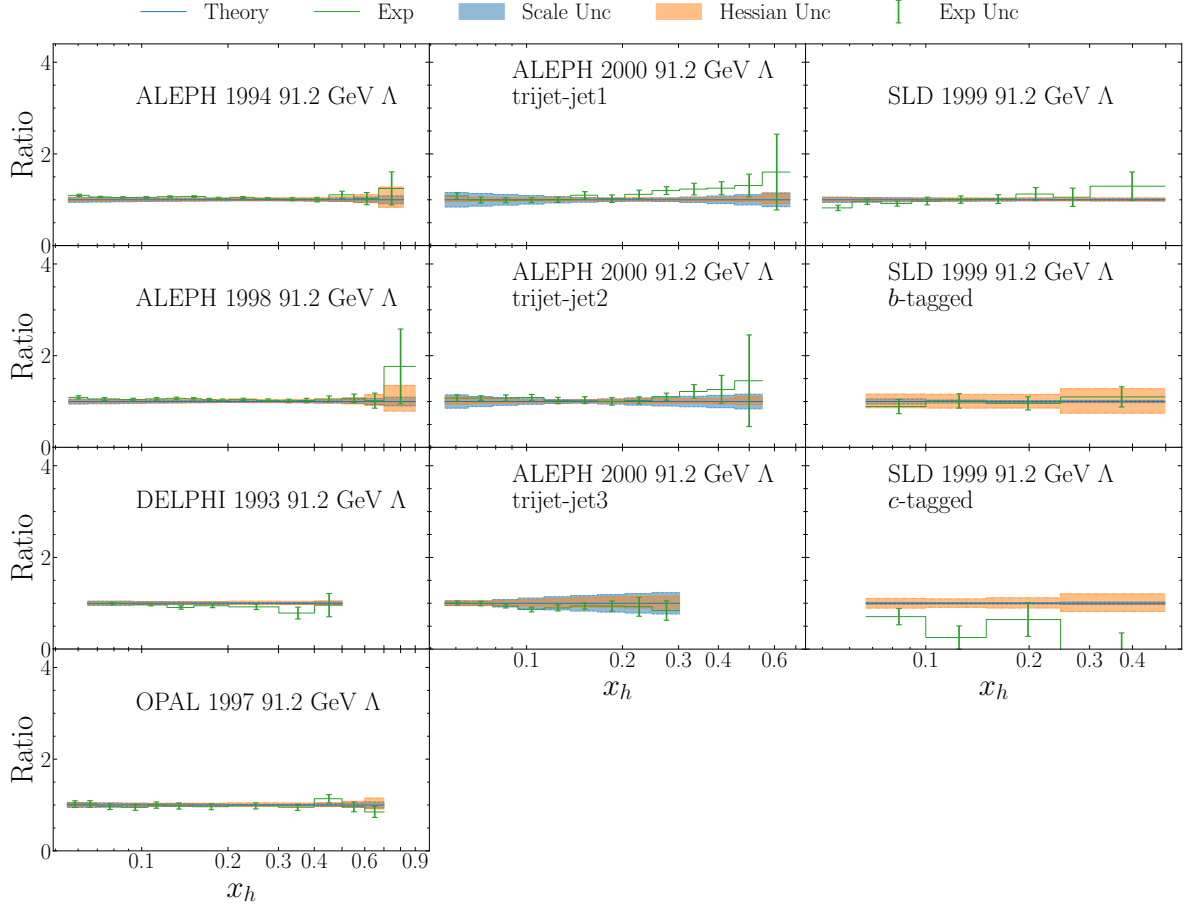


FIG. 20: Same as Fig. 16 but for Λ production in SIA at Z -pole energy.

uncertainties again. The DELPHI [109] and OPAL [111] data are compared to our theory in the last two panels of column 1. Except for a few fluctuations at large x_h , a good alignment is found. Finally, we would like to mention that the inclusive Λ production from ALEPH 2000 paper [103] is not included in our fit, because we observe that the ALEPH 2000 [103] data has some tension with the ALEPH 1998 [94] measurements.

In Fig. 21, we show the data-theory comparison for Λ production in SIA at center-of-mass energies below the Z -boson mass. In particular, data from the TASSO [98], SLAC [112], HRS [100], and CELLO [101] collaborations are included. Starting with the first panel, which compares the CELLO 1990 data [101] to the theoretical predictions, we find that the experimental results are well described, except for the last point, where the data and theory lie outside the 1σ error bands. The second panel presents the comparison with HRS 1987 data [100]. Except for some fluctuations at low x_h , the theory is consistent with the data. We also observe that the Hessian uncertainty is noticeably larger for HRS, which reflects the larger experimental uncertainties. The third panel in the first row compares the data-theory results for the SLAC 1985 data [112], showing good agreement, with only a few differences at low x_h . Finally, the TASSO 1985 data [98] at center-of-mass energies of 14, 22, and 34 GeV are compared to the theoretical predictions in the second panels, from left to right, respectively. A good description is also achieved in these cases.

In Fig. 22, we show the data-theory comparison for the SIDIS process measured by the ZEUS collaboration [85]. The data is grouped into three different Q^2 ranges: $(160, 640) \text{ GeV}^2$, $(640, 2560) \text{ GeV}^2$ and $(2560, 10240) \text{ GeV}^2$. A good description is achieved for datasets in the intermediate and highest Q^2 ranges. However, we find that the data in the lowest Q^2 range can not be well described due to the first and last data points, which deviate significantly from theoretical predictions. For the first point in the lowest Q^2 bin, it is realized that the momentum of the Λ baryon is around $3 \sim 4.5 \text{ GeV}$, approaching the mass of Λ which is 1.115 GeV . At this point, the mass corrections might become more important, which is not implemented in this work. As for the last data point in the lowest Q^2 bin, it has much smaller uncertainty compared to the second-to-last point and it might be an outlier. Thus, further precision measurements from SIDIS remain important, not only for resolving the tension between datasets, but also for better

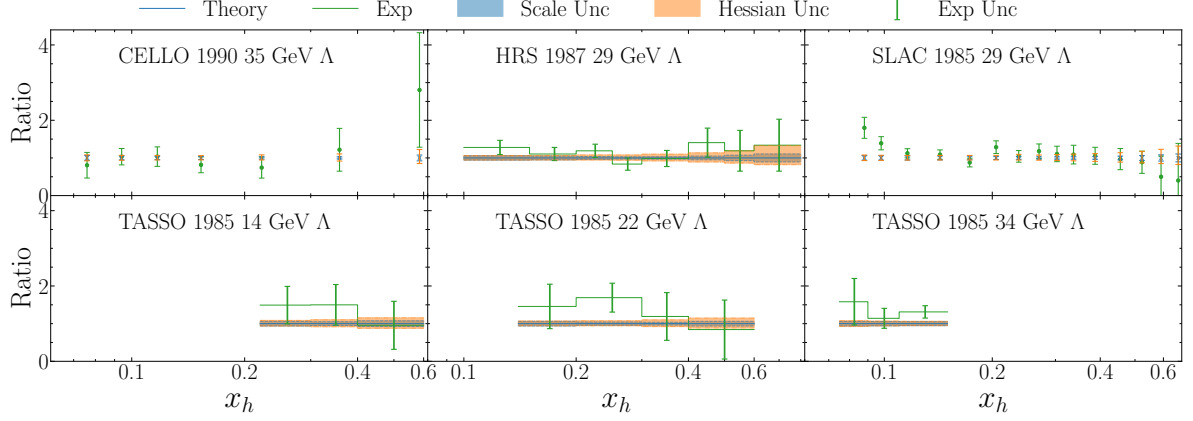


FIG. 21: Same as Fig. 16 but for Λ production in SIA below Z -pole energy. Notice the data points and theory values are only connected horizontally if the measurement is provided with x_h bins.

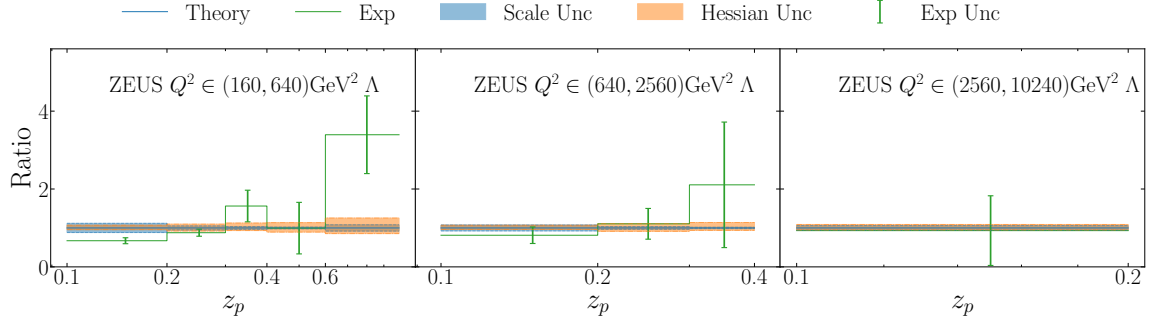


FIG. 22: Same as Fig. 16 but for Λ production in SIDIS process. The ranges of photon virtuality, Q^2 , are also labeled in each panel.

flavor separation in the extraction of Λ FFs.

In Fig. 23 the data-theory comparison is shown for CMS [115] and ALICE [108] measurements. The data in the left panel is the ratio of Λ production cross sections between $\sqrt{s} = 13$ TeV and $\sqrt{s} = 7$ TeV from ALICE, while the data in the right panel is the ratio of Λ production over K_S^0 production at $\sqrt{s} = 900$ GeV from CMS. In the left panel, the theoretical predictions are slightly above the data in the low and high p_T regions, but are always within experimental uncertainties. The scale uncertainties in this case are larger than the Hessian uncertainties in the entire p_T range, while the Hessian uncertainties remain relatively stable across the p_T range. Again, this is due to the difference of slope in running of α_s at different scales (see comments on Fig. 19). For the Λ/K_S^0 ratio data at $\sqrt{s} = 13$ TeV, which is compared to the theory in the right panel, a good agreement between theory and data is achieved in general. However, some fluctuations are observed in the middle- p_T region but the theory remains within the experimental uncertainty. The relatively larger Hessian uncertainty also reflects the weaker constraints of the experimental data.

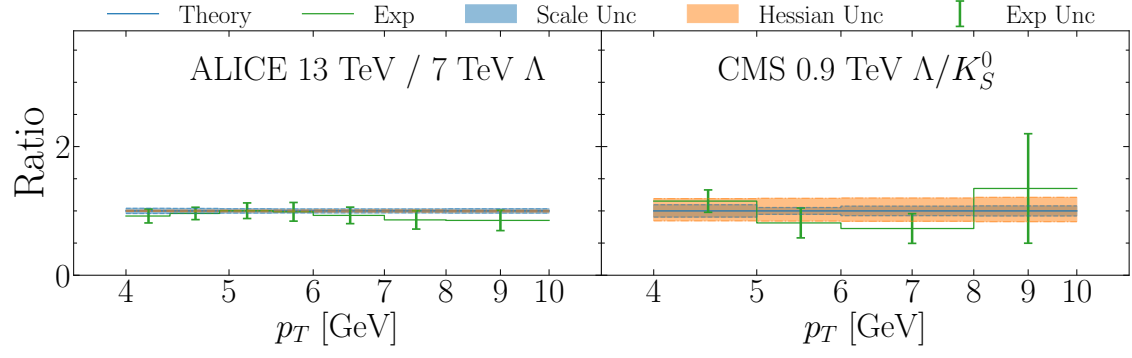


FIG. 23: Same as Fig. 16 but for K_S^0 production in pp collisions. The first panel shows the data-theory comparison for the ALICE data of Λ production ratio between $\sqrt{s} = 13$ TeV and $\sqrt{s} = 7$ TeV. The second panel shows the data-theory comparison for the data of Λ production over K_S^0 production at $\sqrt{s} = 900$ GeV.

collaboration	year	\sqrt{s} [GeV]	χ^2	N_{pt}	χ^2/N_{pt}
ARGUS [125]	1990	9.46	5.94	6	0.99
HRS [124]	1988	29	18.07	13	1.39
JADE [121]	1985	34.4	2.29	2	1.14
JADE [122]	1990	35	3.29	3	1.09
CELLO [123]	1990	35	3.47	5	0.69
L3 [118]	1992	91.2	5.83	4	1.46
L3 [119]	1994	91.2	10.46	10	1.05
ALEPH [116]	1992	91.2	1.48	8	0.18
ALEPH [103]	2000	91.2	18.39	18	1.02
ALEPH jet 1 [103]	2000	91.2	11.26	7	1.61
ALEPH jet 2 [103]	2000	91.2	1.95	6	0.33
ALEPH jet 3 [103]	2000	91.2	10.49	4	2.62
ALEPH [117]	2002	91.2	17.18	5	3.44
OPAL [120]	1998	91.2	7.12	11	0.65
SIA sum			117.20	102	1.15
PHENIX [129]	2011	200	7.61	14	0.51
ALICE [127]	2017	2760	5.37	6	0.90
ALICE [126]	2012	7000	1.26	4	0.32
ALICE [128]	2018	8000	12.64	13	0.97
ALICE [130]	2024	13000	7.11	14	0.51
pp sum			34.00	51	0.67
total sum			151.21	153	0.99

TABLE XVII: Same as Table XV but for η production data.

C. η production

In Table XVII, we present the χ^2 , χ^2/N_{pt} values and summary for different categories similar to that in the K_S^0 fit. For the global dataset, we obtain a total χ^2 value of 151.21 for 152 data points, resulting in a χ^2/N_{pt} of 0.99, which indicates good overall agreement between the theoretical predictions and the experimental data. Examining different experimental categories, we find that the SIA measurements are well described with $\chi^2/N_{\text{pt}} = 1.15$ for 102 data points. Moreover, a good agreement with the pp collision data is also achieved with $\chi^2/N_{\text{pt}} = 0.68$ across 50 data points. For individual experiments, most datasets are well described with $\chi^2/N_{\text{pt}} \approx 1$. However, the η -in-jet production (the third jet in particular) from the ALEPH 2000 data [103], and the inclusive η production from the ALEPH 2002 data [117] can not be described very well. The fit quality to these two datasets will be discussed in more detail later.

In Fig. 24, the ratio of experimental data to theoretical predictions for η meson production at the Z -pole is presented, including data from ALEPH [103, 116, 117], L3 [118, 119] and OPAL [120] collaborations. Notice that for η production in SIA at Z -pole, the cross sections are differential in x_p instead of x_h . The predictions to ALEPH 2002 [117] underestimate the data, while the predictions to ALEPH 2000 [103] overshoot the data, indicating a possible inconsistency between these two measurements. Here we note that neither AESSS [84] nor LAXZ [82] can describe the ALEPH 2002 well, which further confirms the tension between the ALEPH 2002 data and the other world data. The ALEPH 1992 data [116], on the other hand, is very well described with $\chi^2/N_{\text{pt}} = 0.18$. The comparisons to L3 1992 [118] and L3 1994 [119] data are shown in the first two panels of the second column in Fig. 24, in which a generally good description is achieved, with some fluctuations that are mostly within the experimental uncertainties. For OPAL data [120] a good description is found with $\chi^2/N_{\text{pt}} = 0.65$.

Fig. 24 also shows the comparison between the experimental data and the theoretical predictions for η meson production in tri-jet events at the Z -pole energy, with measurement conducted by ALEPH [103]. With η produced in the first, second, and third jet shown from top to bottom of the last column in Fig. 24, respectively. For jet 1, the theoretical predictions are consistent with the data in the range $x_p > 0.3$, however, the theory values are found to be higher than the data in the low- x_p region. For jet 2, in the low- x_p region, the data is underestimated by the

theory, but both are within the uncertainties. Jet 3 shows the worst agreement, with the data significantly exceeding the theoretical prediction in the low- x_p region. The Hessian uncertainties in this case are also significantly larger than those in other experiments, indicating a weak constraining power from the data. We also notice that the scale uncertainties in predictions for the tri-jet experiment are again more pronounced than those in other experiments, as previously discussed for the case of K_S^0 and Λ in Sections V A and V B.

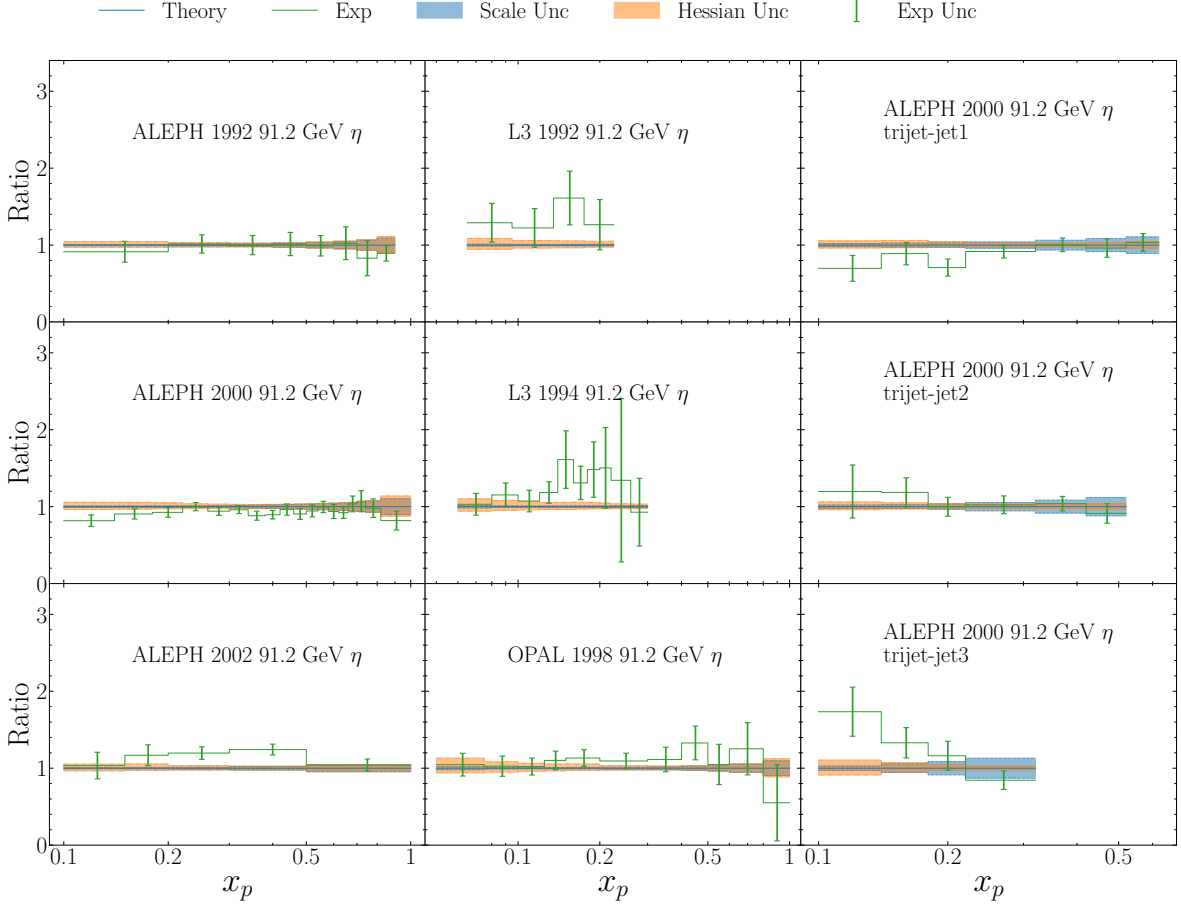


FIG. 24: Same as Fig. 16 but for η production in SIA at Z -pole energy.

In Fig. 25, the theory and data for SIA are compared with center-of-mass energies below the Z -boson mass. These include ARGUS at 9.46 GeV [125], HRS at 29 GeV [124], JADE at 34.4 GeV [121] and 35 GeV [122], as well as CELLO at 35 GeV [123]. For the JADE and CELLO datasets, the experimental data are generally well described by the theoretical predictions, with slight deviations at high x_p values. For the ARGUS and HRS datasets, most of the data falls within the theory predicted bounds, except for minor deviations in the intermediate- x_p regions.

In Fig. 26, a comparison between the best-fit predictions and the data is shown. Results from ALICE at 2.76 TeV [127], 7 TeV [126], and 8 TeV [128], as well as from PHENIX at 200 GeV [129], are presented. From the figure, it can be observed that most data points are very well described by the theory, with only a few exceptions that are generally within experimental uncertainty. In the low- p_T regions, we observe that the scale uncertainties can become significant, which has been discussed for the case of K_S^0 and Λ in Sections V A and V B.

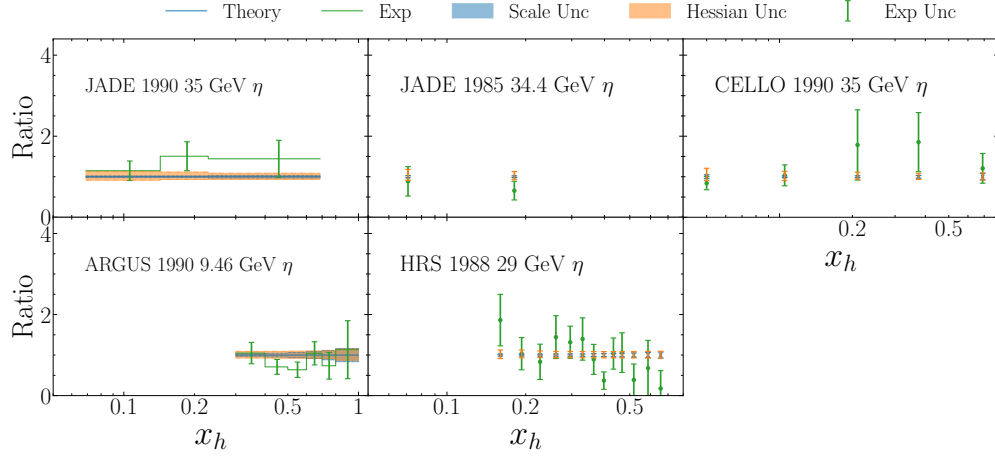


FIG. 25: Same as Fig. 16 but for η production in SIA below Z -pole energy.

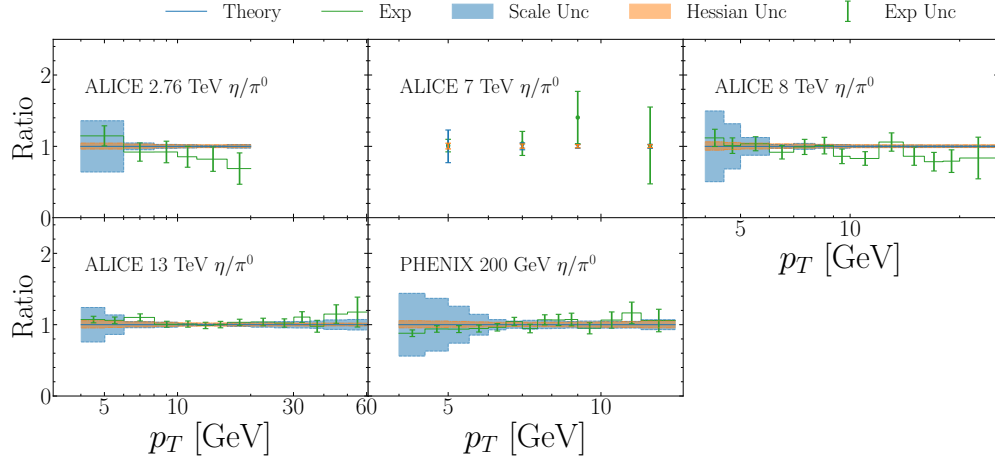


FIG. 26: Same as Fig. 16 but for data of η production over π^0 production at various center-of-mass energies in pp collisions.

collaboration	year	\sqrt{s} [GeV]	χ^2	N_{pt}	χ^2/N_{pt}
ARGUS [125]	1990	9.46	20.12	14	1.44
JADE [121]	1985	34.4	7.92	10	0.79
JADE [122]	1990	35	8.66	9	0.96
JADE [122]	1990	44	7.30	6	1.22
CELLO [133]	1990	35	31.31	15	2.09
TASSO [134]	1989	44	1.66	6	0.28
ALEPH [131]	1997	91.2	14.85	20	0.74
ALEPH jet 1 [103]	2000	91.2	2.43	8	0.30
ALEPH jet 2 [103]	2000	91.2	11.69	8	1.46
ALEPH jet 3 [103]	2000	91.2	34.65	6	5.77
DELPHI [132]	1996	91.2	4.86	17	0.29
DELPHI b -tagged [132]	1996	91.2	9.12	15	0.61
L3 [119]	1994	91.2	27.34	12	2.28
OPAL [120]	1998	91.2	2.73	10	0.27
SIA sum			184.64	156	1.18
STAR [135]	2009	200	6.09	8	0.76
PHENIX [136]	2007	200	45.76	17	2.69
PHENIX [137]	2016	510	66.95	22	3.04
ALICE [127]	2017	2760	13.98	16	0.87
ALICE [126]	2012	7000	29.27	13	2.25
ALICE [128]	2017	8000	46.42	24	1.93
pp sum			208.47	100	2.08
total sum			393.11	256	1.54

TABLE XVIII: Same as Table XV but for π^0 production data. Notice in this situation we only predict the data using the π^0 FFs that are constructed from π^\pm FFs, *i.e.*, a global analysis is *not* performed for π^0 .

D. π^0 production

In Table XVIII, we show the χ^2 values for π^0 production in SIA and pp collisions, with π^0 FFs constructed from the NPC fitted π^\pm FFs [44] in Eq. (3). This table does not represent a direct fit to the π^0 data; instead, it evaluates the compatibility of the π^\pm -based predictions with the observed π^0 distributions across various experimental setups.

For the SIA datasets, the total χ^2/N_{pt} is 1.18 over 156 data points, reflecting a generally acceptable match between the π^\pm -based predictions and π^0 measurements. However, individual experiments exhibit different levels of agreement. Notably, the ALEPH 2000 (jet number 3 in three-jet events) dataset [103] displays a relatively high χ^2/N_{pt} of 5.77 due to the high precision of the data. This suggests potentially different constraints on gluon FFs from hadron-in-jet measurements in SIA versus pp collisions, both of which contribute to the determination of charged pion FFs. Other datasets, such as those from JADE 1985 [121], TASSO 1989 [134], DELPHI 1996 [132] and OPAL 1998 [120], yield χ^2/N_{pt} values well below 1, indicating better alignment.

For the pp collision datasets, unlike the π^\pm fit where ratios of different hadrons at the same energy or the same hadron at different energies are used (resulting in reduced relative errors), here we rely on invariant cross sections, $E d^3\sigma / d^3\vec{p}$, and they generally have larger experimental uncertainties. Despite this, several pp datasets demonstrate a strong alignment with the theoretical predictions. Specifically, the STAR 200 GeV data [135] and ALICE 2.76 TeV data [127] exhibit χ^2/N_{pt} values of 0.76 and 0.87, respectively. However, some datasets, such as PHENIX 2007 [136] and 2016 [137], show higher χ^2/N_{pt} values of 2.69 and 3.04, respectively, suggesting greater deviations. The combined χ^2/N_{pt} for the pp group is 2.08 across 100 points, reflecting the varied levels of agreement between theory and data.

Fig. 27 show the comparison between theoretical calculations and SIA measurements at the Z -pole energy. These comparisons encompass inclusive π^0 production data from four LEP experiments (ALEPH [131], DELPHI [132], L3 [119] and OPAL [120]), as well as the specialized tri-jet measurements from ALEPH [103] and b -tagged π^0 production from DELPHI [132]. The experimental data from ALEPH, DELPHI and OPAL demonstrate remarkable consistency with theoretical predictions, maintaining ratios close to unity across the measured x_p range. A notable exception

appears in the L3 data, which shows data-theory ratios of ~ 0.75 , accompanied by substantial experimental uncertainties. In the context of jet-specific analyses, the scale uncertainties dominate over their Hessian counterparts and show a characteristic increase with x_p , as previously discussed in Sections V A and V B. The theoretical predictions align well with ALEPH tri-jet measurements (for the first two jets), with most theoretical values falling within the experimental uncertainty bands. The exception is on the third jet of the tri-jet events, in which a larger disagreement is found. However, these differences remain comparable to the size of scale variations in general. The b -tagged measurements from DELPHI show particularly good agreement in the intermediate and high x_p regions ($x_p > 0.1$), though some fluctuations are evident in the low x_p region. The large Hessian uncertainties in this case reflect the large experimental uncertainties.

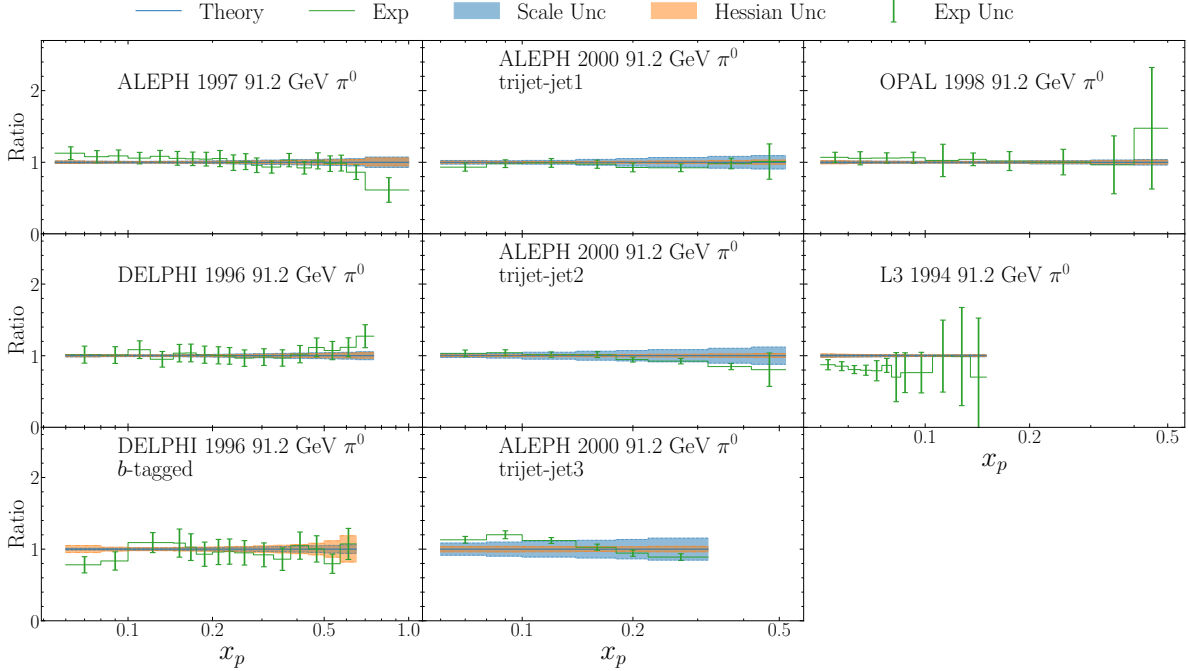


FIG. 27: Same as Fig. 16 but for π^0 production in SIA at Z -pole energy.

Fig. 28 illustrates the comparison between theoretical predictions and SIA measurements at various low-energy scales, spanning from 9.46 GeV to 44 GeV. These datasets include ARGUS [125] at 9.49 GeV, JADE at 34.4 GeV [121], 35 and 44 GeV [122], CELLO [133] at 35 GeV and TASSO [134] at 44 GeV. The JADE 35 GeV data is well described by theoretical predictions, while the JADE 34.4 GeV data is not well described at low x_p values. The JADE 44 GeV data is well described at low x_p , but a large deviation is found at large x_p values. However, due to the large experimental uncertainties, the χ^2/N_{pt} for JADE experiments are all around 1. The measurements from CELLO, TASSO and ARGUS, while showing some statistical fluctuations, are generally well described by the theoretical predictions. Most data points and theoretical values fall within the 1σ bands of each other. The occasional excursions outside these uncertainty bands are consistent with expected statistical variations, suggesting that there are no significant systematic discrepancies between theory and experiment across these energy scales.

Fig. 29 presents a comparison between theoretical calculations and experimental measurements for π^0 production in pp collisions. Each panel displays the ratio between experimental data and theoretical predictions, where the measurements and uncertainties are normalized to the theoretical central values. The analysis encompasses data from multiple experiments: STAR measurements at 200 GeV [135], PHENIX results at 200 GeV [136] and 510 GeV [137], as well as ALICE measurements at 2.76 TeV [127], 7 TeV [126] and 8 TeV [128]. A striking feature of these comparisons is the substantial scale uncertainty, especially in the low- p_T region. This occurs because of both the low energy scales and the need to extrapolate the FFs below their parametrization scale during evolution. In contrast, the Hessian uncertainties exhibit remarkable stability and remain relatively modest across all transverse-momentum ranges. Most experimental datasets are generally better described in the high p_T region, and are greatly underestimated in the low p_T region. That is a typical feature as already observed in our previous analysis of charged pions [44]. This behavior suggests a systematic tension that persists across different experimental conditions and collision energies. The STAR data, on the other hand, are not well described across the entire p_T range.

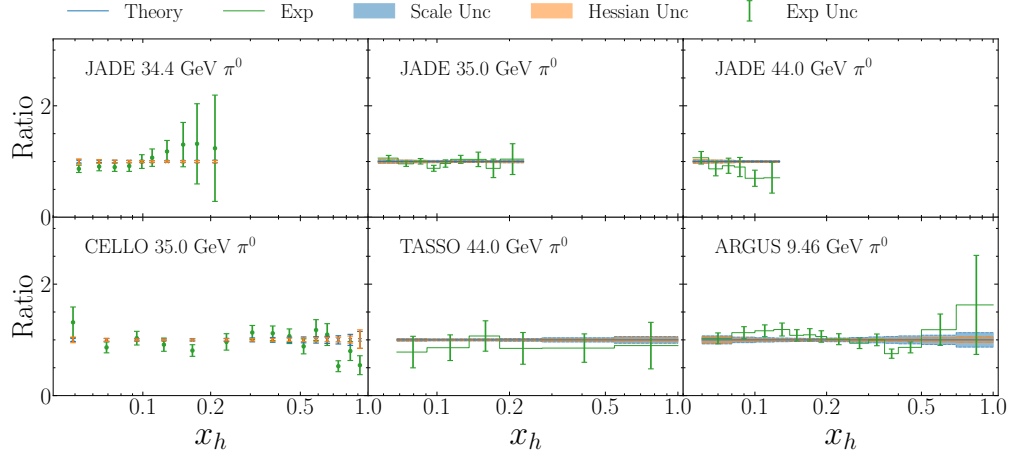


FIG. 28: Same as Fig. 16 but for π^0 production in SIA below Z -pole energy.

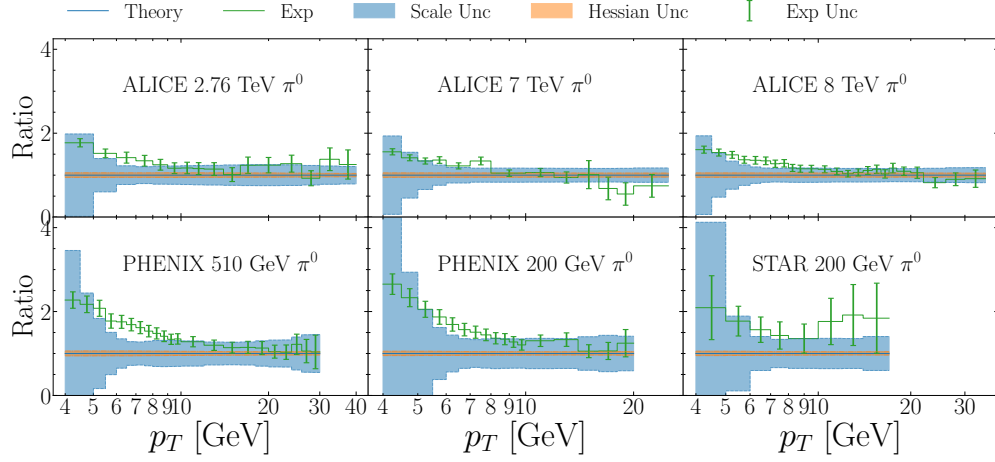


FIG. 29: Same as Fig. 16 but for π^0 production in pp collisions.

VI. ALTERNATIVE FITS

In this section, we perform some variations on the nominal NPC23 fits, in order to study in detail the constraints coming from each dataset. This is done by systematically subtracting different experiments from the nominal fit (baseline), while keeping other settings, including the kinematic cuts and treatment of experimental uncertainties, intact. By doing this, we can learn the impact of a certain experiment on the final extracted FFs. The global datasets are categorized into five distinct groups based on the types of reaction: SIA measurements at the Z -pole (excluding hadron-in-jet productions), SIA hadron-in-jet measurements, SIA measurements below the Z -pole, SIDIS measurements and pp collisions. This study is performed for the FFs of K_S^0 and Λ . As for η FFs, due to the limited constraint provided by existing world data, we plan to defer this analysis to a future time when more high-precision data on η production become available.

We would like to emphasize that when analyzing the subtraction diagrams, one needs to realize that when the subtracted result prefers a relatively larger distribution than that of the baseline result, it indicates that the subtracted datasets prefer a smaller distribution and vice versa.

A. K_S^0 production

In this section, we present the data subtraction analysis for the K_S^0 production. The comparison between each alternative fit and the baseline fit is shown in Figs. 30 to 34. The figures show the comparison of FFs between the baseline fit and subtracted fit for each parton flavor in separate panels, with FFs plotted at scale $Q^2 = 25 \text{ GeV}^2$. For each flavor we plot the actual $zD(z)$ values along with their uncertainties normalized to the corresponding central values in baseline and subtracted fits. The baseline results are plotted in blue, while the subtracted results are plotted in orange. The bands represent Hessian uncertainties at a confidence level of 68%. The impact of removing each subgroup can be visualized as deviations from the baseline results.

The results after the removal of the SIA data at Z -pole energy are presented in Fig. 30. The distributions that undergo significant change are those of u , c and b quarks. The d , s , and gluon distributions also experience an enlargement of uncertainties; however, the shape and central values are generally within 1σ from those of the baseline fit. Clearly, the SIA data provides the most constraints to the u quark distribution, putting both its shape and the uncertainty under control. For the c and b quark distributions, a significant increase in uncertainty is observed. This is caused by the subtraction of SLD c/b -tagged data [87].

The impact of removing SIA K_S^0 -in-jet data at Z -pole energy is displayed in Fig. 31. Significant effect is observed primarily in the gluon FFs, this is expected as the third jet in the tri-jet event is usually a gluon-initiated jet. The gluon distributions from the subtracted fit and the baseline fit agree with each other (within 1σ) in the region $z \gtrsim 0.15$, with the subtracted fit showing significantly larger Hessian uncertainties. In the region where $z \lesssim 0.1$, on the other hand, the gluon distribution of the subtracted result is less constrained. As for the quark distributions, we notice that the u and b quark FFs also show some changes in the low z region, but the central values are within 1σ of the baseline results. Finally, the changes in d , s and c distributions are only marginal, and this is understandable as the tri-jet data is mainly sensitive to the gluon distributions.

The results after the removal of the SIA data below Z -pole energy are illustrated in Fig. 32. The u quark distribution after subtraction is still consistent with the baseline result within uncertainties, so are the gluon and b quark distributions. However, for the s and d quark distributions, we notice that they are both dramatically different from those of the baseline fit. This indicates that the SIA data below Z -pole energy are crucial in constraining the favored quark distributions in K_S^0 . Apart from the constituent quarks, the c quark distribution also shifts downward after subtraction, especially in the mid- z region.

The impact of removing SIDIS measurements is presented in Fig. 33. The u -quark fragmentation shows the most pronounced response, and by comparing with Fig. 30, we find that the u quark distribution is mainly constrained by the SIA data at Z -pole energy as well as SIDIS data. The c quark distribution is also affected in the region $z \lesssim 0.2$, showing the flavor separating capability of SIDIS data for u and c . Interestingly, the d and s remain relatively stable after subtraction of SIDIS data, despite the fact that the SIDIS data was expected to help in discriminating the two flavors. This again urges further precision SIDIS measurement for K_S^0 production, so that we can achieve flavor separation between the two constituent quark flavors of K_S^0 . Lastly, the gluon and b quark distribution are fairly stable after removal of SIDIS datasets, and this is expected since gluon contribution starts at NLO and bottom quark is not copiously produced in SIDIS.

As shown in Fig. 34, the removal of pp data has minimal impact on most flavors, with significant effects observed only on gluon FFs. This can be expected as the quark distributions are already well constrained by the SIA data (including c/b -tagged K_S^0 production data and K_S^0 -in-jet data), as well as SIDIS data, the pp collision data can only

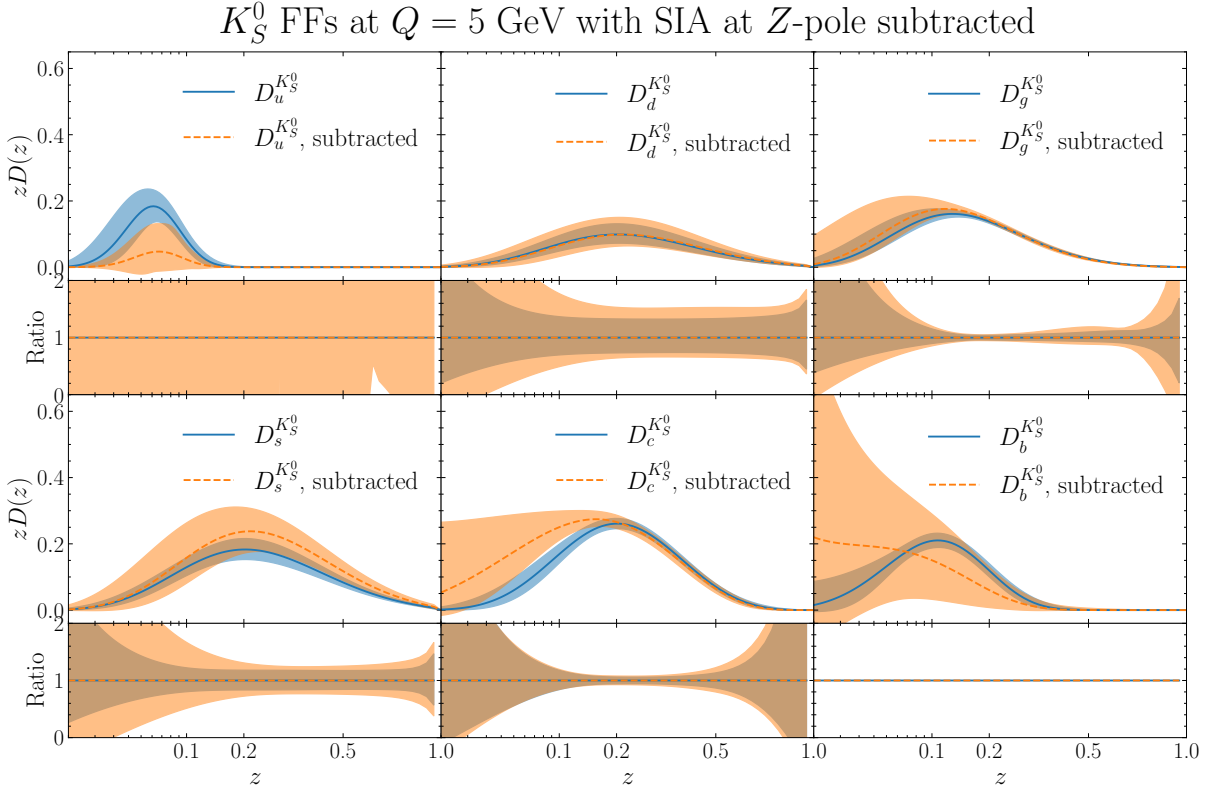
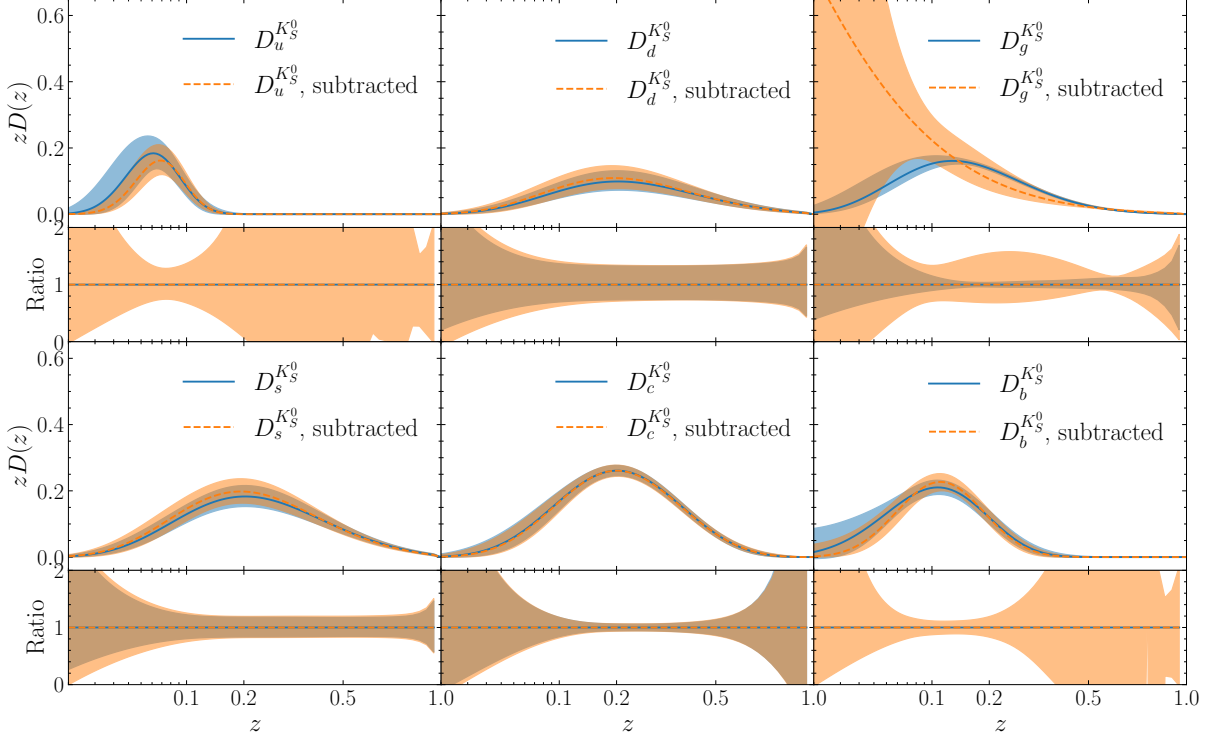
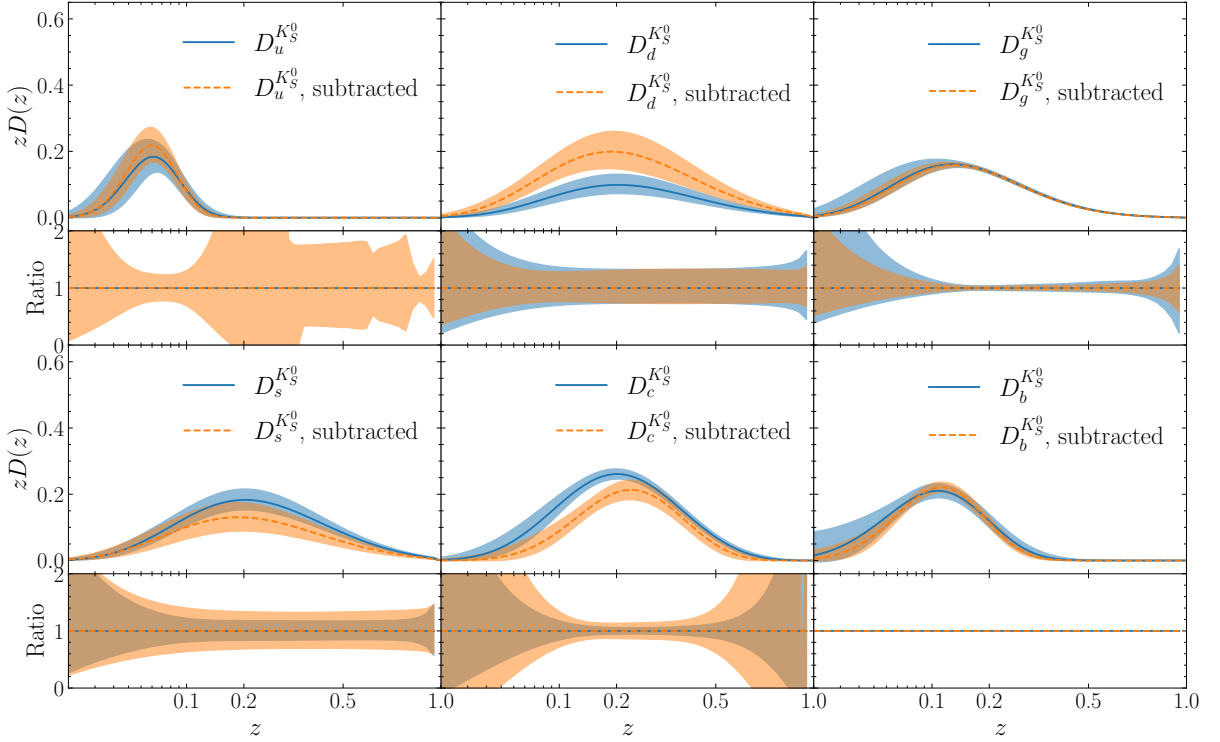
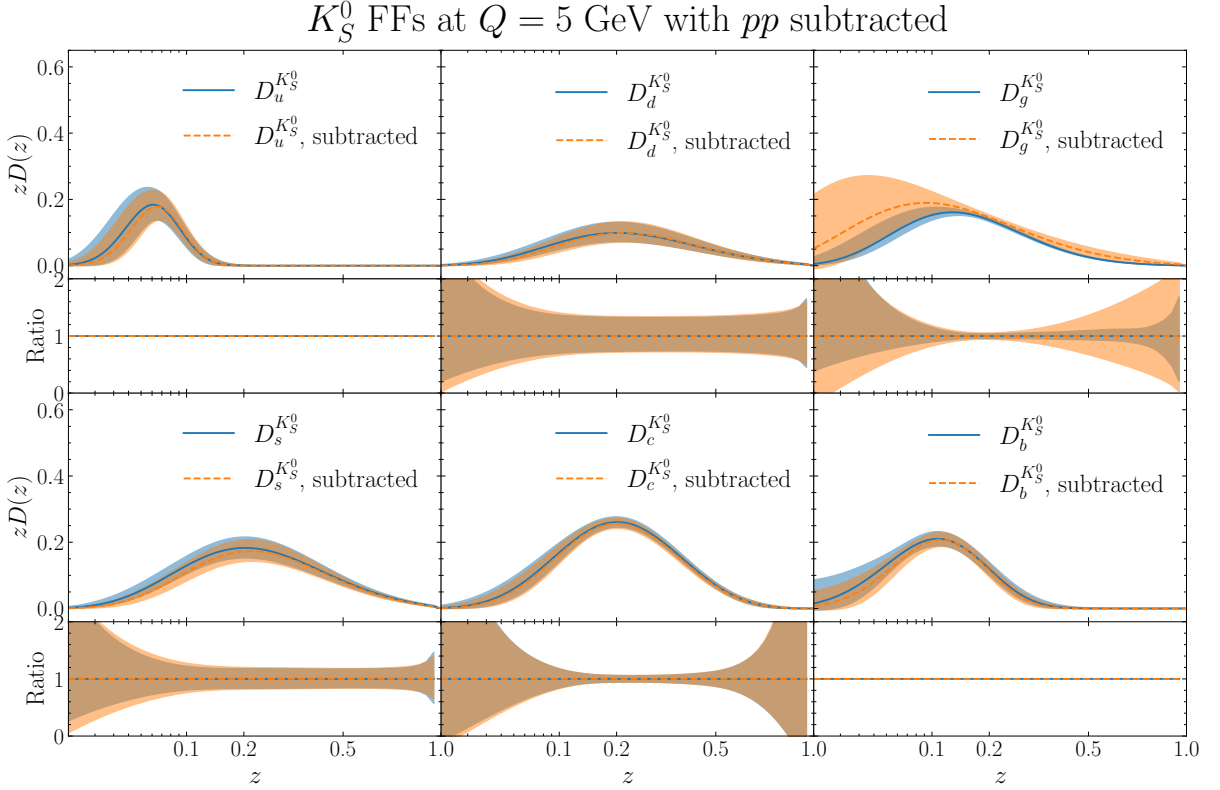
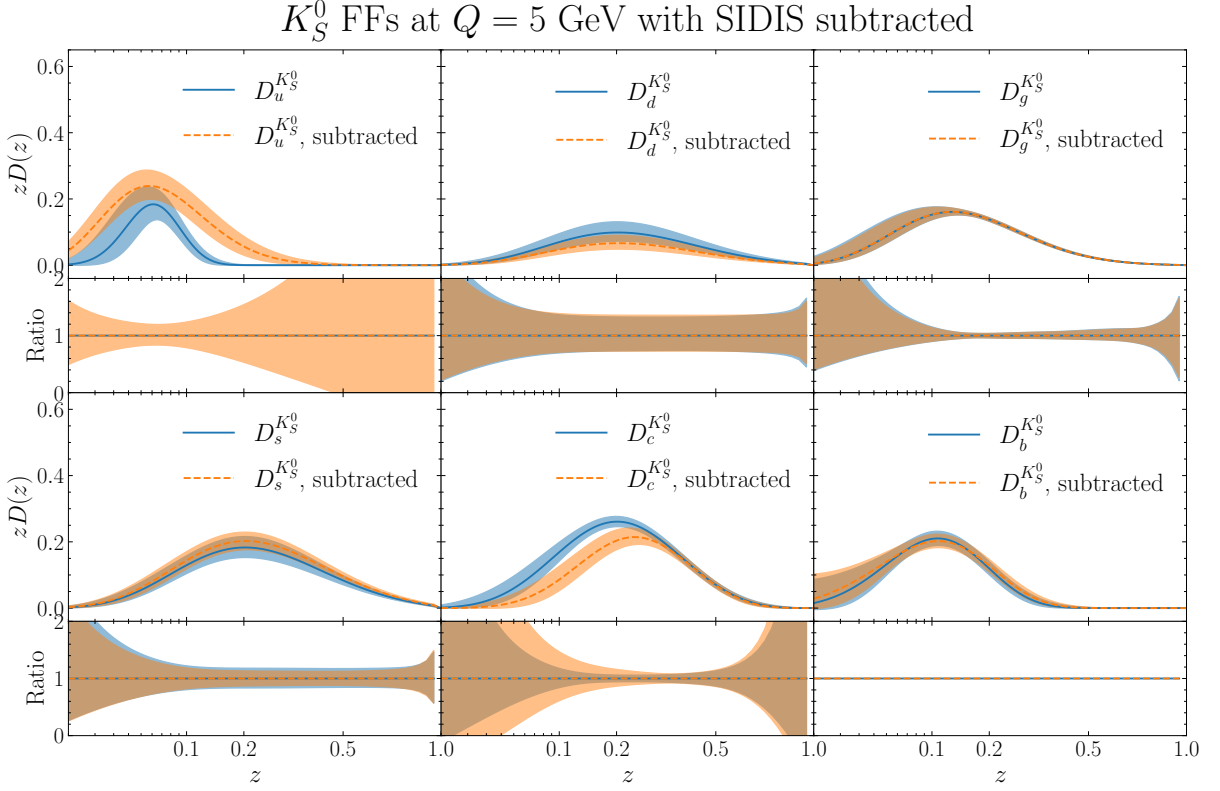


FIG. 30: Comparison of the baseline fit (blue) and the alternative fit (orange) that subtracts the SIA data at Z -pole energy (the K_S^0 -in-jet data are not subtracted). FFs and their uncertainties for different partons are plotted in each panel. Relative errors are plotted in the lower pannel of each parton. The FFs are plotted at $Q^2 = 25$ GeV² with respect to the momentum fraction z . In order to better display the behaviour of FFs at both low and high z regions, we made the plot in $z^{1/3}$ scale. The uncertainty bands represent Hessian uncertainties at confidence level of 68%.

provide limited additional constraints. However, for the gluon FFs, since gluon channels start contributing at LO in pp collisions, a discernible amount of constraints can be expected from pp data.

K_S^0 FFs at $Q = 5$ GeV with SIA jet subtracted

 FIG. 31: Same as Fig. 30 but for subtraction of K_S^0 -in-jet production in SIA at Z -pole energy.

 K_S^0 FFs at $Q = 5$ GeV with SIA below Z -pole subtracted

 FIG. 32: Same as Fig. 30 but for subtraction of K_S^0 production in SIA below Z -pole energy.



B. Λ production

In this section, we present the data subtraction analysis for Λ production. The comparison between each alternative fit and the baseline fit is shown in Figs. 35 to 37. The labels and meaning of the colored bands are the same as in the case of K_S^0 subtraction, and are given in Section VIA.

In Fig. 35, the Λ production in SIA at Z -pole energy is eliminated from the global datasets, and the FFs fitted with these modified datasets are compared to the baseline FFs. Notably, the Λ -in-jet data remain unchanged in this context. Taking into account u and d FFs, it is evident that the SIA data at the Z -pole exert a notable influence, favoring smaller (almost negligible) distributions of u and d . For the s distribution, a significant impact is also observed from the SIA data at the Z -pole, with a similar preference for a reduced distribution. Specifically, the strange distribution is more effectively constrained at low momentum by SIA data at the Z -pole owing to their elevated center-of-mass energies. In contrast, SIA data at Z -pole exhibit a preference for a more extensive gluon distribution than those inferred from other global datasets. Moreover, the SIA data at the Z -pole impose tighter constraints on the c distribution derived from SLD c -tagged data [87]. In contrast, the subtraction of SLD b -tagged data does not exhibit a pronounced effect, probably because the b quark distribution has already been accurately determined through other global data.

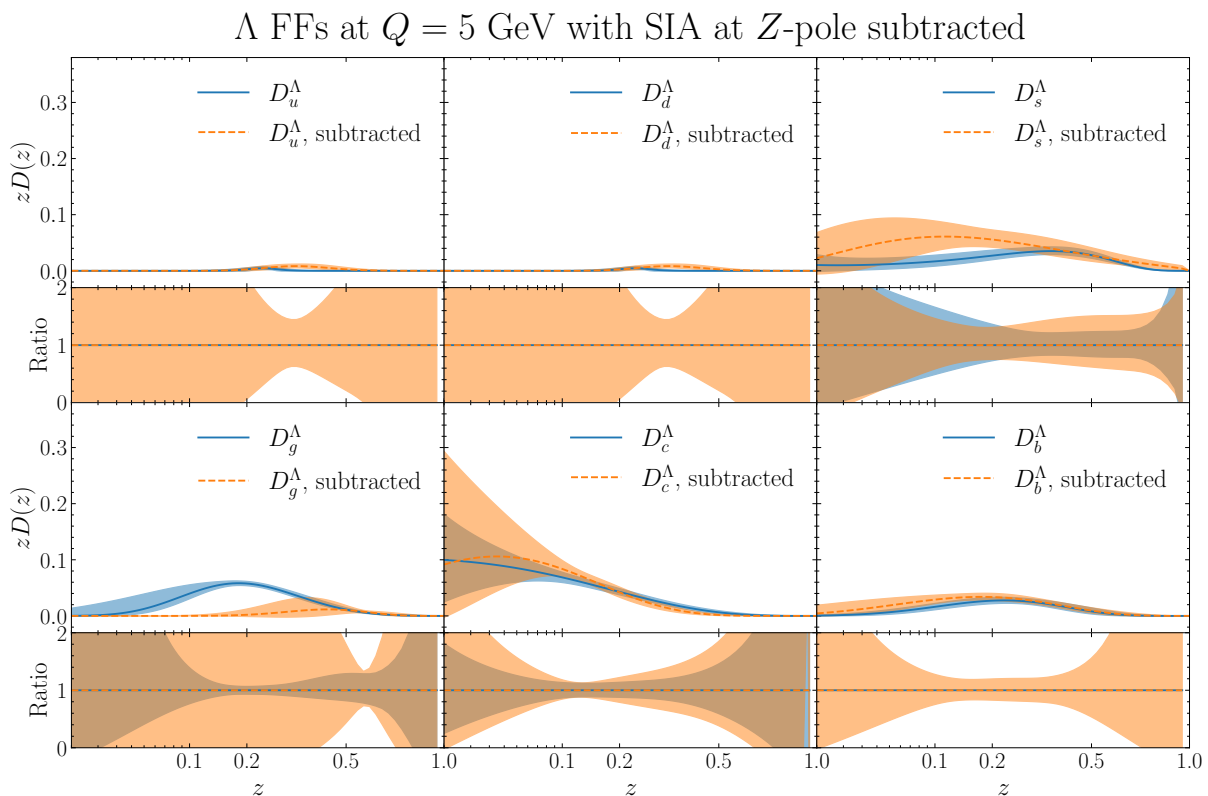


FIG. 35: Same as Fig. 30 but for subtraction of Λ production in SIA at Z -pole energy. (The Λ -in-jet data are not subtracted.)

The subtraction of SIA Λ -in-jet data at Z -pole energy is demonstrated in Fig. 36. First, we observe that the u and d distributions exhibit minimal change, suggesting that an effective constraint is provided by the remaining global data. The strange distribution, while aligning with the baseline outcome in the large z region, has its uncertainty potentially reducible with the inclusion of jet data. The constraint on the gluon distribution is also enhanced by incorporating jet data, which aligns with the expectation that the third jet in a three-jet event is typically a gluon jet. Lastly, the c quark distribution is more significantly affected in low momentum fraction regions, whereas the b quark distribution remains stable upon the subtraction of Λ -in-jet data.

In Fig. 37, we present the results from subtraction of the SIA data below the Z -pole energy. The SIA data below Z -pole energy has almost no impact on the u , d , b and gluon distributions, however, they do provide significant constraints for the strange and charm production rates at low z region.

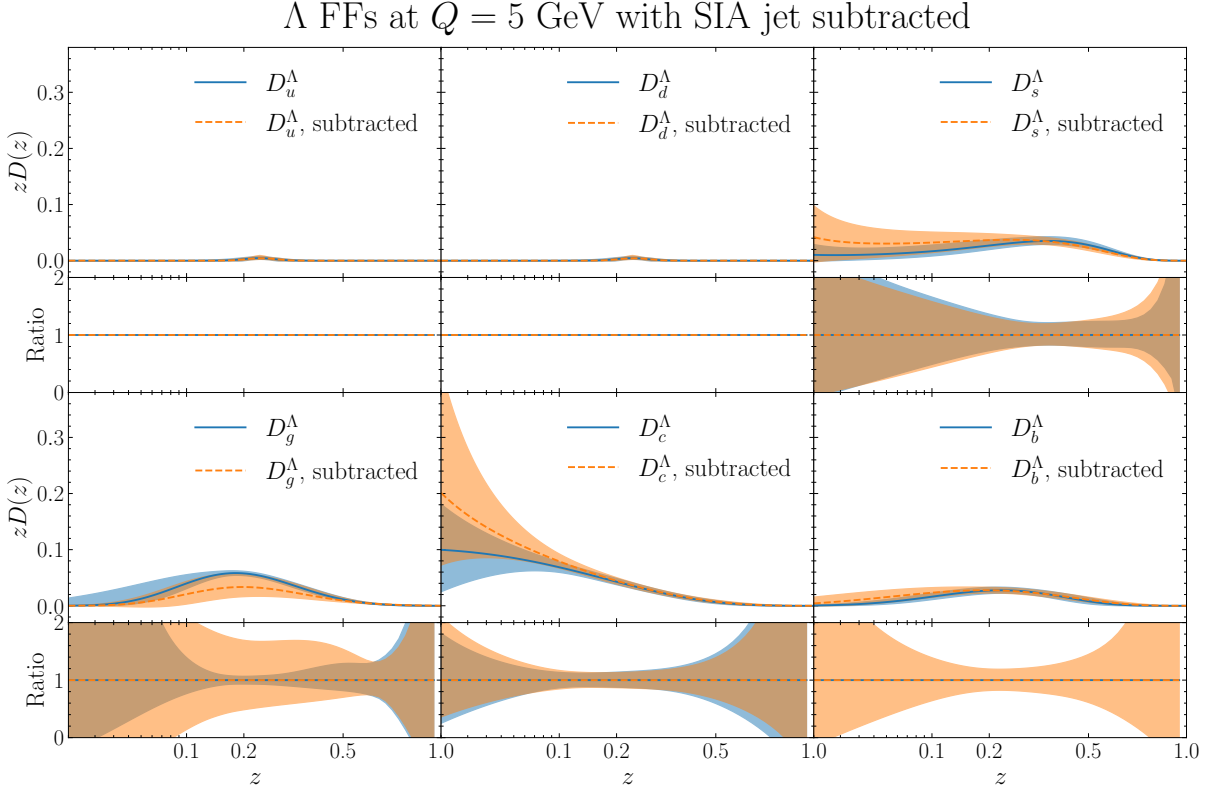


FIG. 36: Same as Fig. 30 but for subtraction of Λ -in-jet production in SIA at Z -pole energy.

The subtraction of SIDIS and pp data has almost no impact compared to the baseline results. Figures are omitted for the sake of brevity. This indicates that the Λ FFs are already well determined by the SIA data, while the SIDIS and pp data, with relatively larger experimental uncertainties, do not provide further constraints.

Λ FFs at $Q = 5$ GeV with SIA below Z -pole subtracted

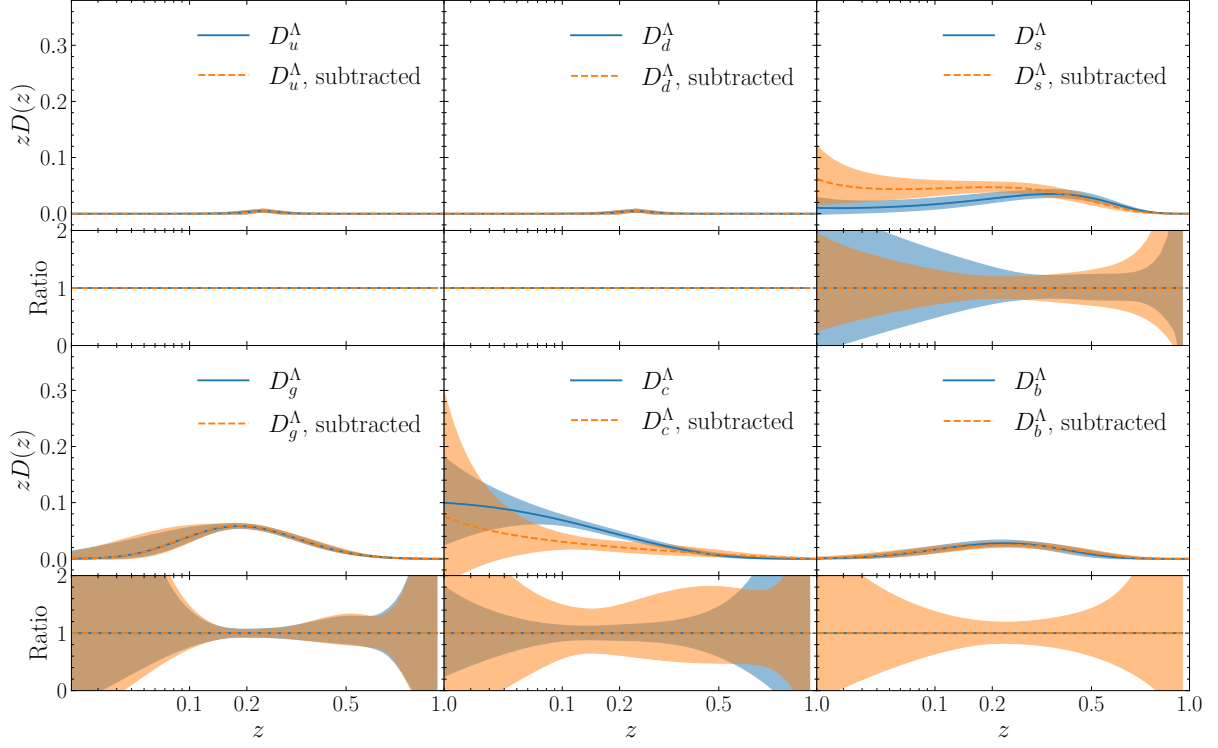


FIG. 37: Same as Fig. 30 but for subtraction of Λ production in SIA below Z -pole energy.

VII. DISCUSSION AND CONCLUSIONS

In this paper, we have presented the extraction of fragmentation functions (FFs) for light neutral hadrons including K_S^0 meson, Λ baryon and η meson from global analysis of world data. In addition, we provide the π^0 meson FFs constructed from those of π^\pm via isospin symmetry. In the region $z \sim (0.1, 0.5)$, where precise data are available, the extracted FFs are in general well constrained. As for the quality of the fit, good χ^2 values are found for most datasets from various processes, including SIA, SIDIS and pp collisions. With the most comprehensive datasets included in the fit to neutral hadrons, we are able to deliver the state-of-art neutral hadron FFs. In particular, with the K_S^0 -in-jet data incorporated, the extracted gluon FFs get better constrained. In addition, thanks to the FMNLO framework, we are able to provide the Λ FFs and η FFs with uncertainties that are not available in previous global analyses. In identifying the direction of future measurements, uncertainties of FFs will be of important reference, since larger uncertainty implies areas of valuable future exploration. Furthermore, with the uncertainties now available for Λ and η FFs, future predictions of related observables can include theoretical uncertainties as well. Finally, in order to analyze the constraints from different experiments, we also perform alternative fits with a particular group of datasets subtracted during the fit.

As applications of the extracted FFs, we provide several predictions to physical quantities that are of interest. We first calculate the fraction of momentum carried by the fragmented hadrons from the final-state partons, for each hadrons analyzed in this paper as well as all the charged and neutral hadrons from this and previous NPC analyses. The neutral hadrons are found to carry approximately 25% \sim 38% of the momentum from gluon and u , d , c and b quarks, while about 51% of the momentum from the s quark. Moreover, the total momentum carried by neutral and charged hadrons generally obeys the momentum sum rule. Though moderate violation is observed for the s quark, a definitive conclusion will require future high precision data.

Furthermore, we predict the hadron-in-jet production rates for $pp \rightarrow Z + \text{jet}$ process with LHCb kinematics. Since the hadron-in-jet observable is differential in the momentum fraction z , future measurements of such observable will greatly help in further constraining the FFs of neutral hadrons. Lastly, we provide predictions on ratios of K_S^0 and K^\pm production rates dedicated to current and future measurements at SLD, Belle, COMPASS, ALICE and LHCb experiments. Such ratios are of great importance in studying the isospin symmetry in kaon fragmentation.

In our analysis, we find that certain distributions are not very well constrained by current data. For K_S^0 FFs, the strange and down quark distributions can only be separated with certain prior assumptions. The η FFs from the gluon also show large uncertainties, especially in the low z region. Such limitations highlight the necessity of future high precision measurements, with emphasis on flavor separation. For example, the FFs of K_S^0 from the strange and down quark can be better constrained by future measurements of the SIDIS process, and the FFs of η from the gluon can benefit from future measurements of hadron-in-jet productions, both in SIA and pp collisions. In addition, the c and b -tagged SIA data can help improve the determination of η FFs.

This work is a continuation of the previous NPC analysis in which the light charged hadron FFs are determined. As a collective endeavor into providing comprehensive and accurate fragmentation functions, our work has made an important step forward into the less constrained realm of light neutral hadron FFs. In addition, we provide comparisons of our FFs with the determination of other groups in Appendix A. The impact of recent released measurements on neutral hadron production from the Belle experiment is studied in Appendix B. The impact of recent measurements on the η/π^0 ration from LHCb is shown in Appendix C. The FFs presented in this work are publicly available in LHAPDF format with the details given in Appendix D.

Acknowledgments.

The work of J.G. is supported by the National Natural Science Foundation of China (NSFC) under Grant No. 12275173, Shanghai Municipal Education Commission under Grant No. 2024AIZD007, and open fund of Key Laboratory of Atomic and Subatomic Structure and Quantum Control (Ministry of Education). H.X. is supported by the NSFC under Grants No. 12475139 and Guangdong Major Project of Basic and Applied Basic Research Nos. 2020B0301030008. Y. Zhao is supported by the NSFC under Grant No. U2032105 and the CAS Project for Young Scientists in Basic Research No. YSBR-117. X.S. is supported by the Helmholtz-OCPC Postdoctoral Exchange Program under Grant No. ZD2022004. Y. Zhou is supported by the European Union “Next Generation EU” program through the Italian PRIN 2022 grant n. 20225ZHA7W.

Appendix A: Comparison to other groups

In this section, we present the comparison between our fitted FFs and the FFs obtained by other groups. The comparison is conducted at two energy scales: $Q = 5$ GeV and $Q = 91.2$ GeV.

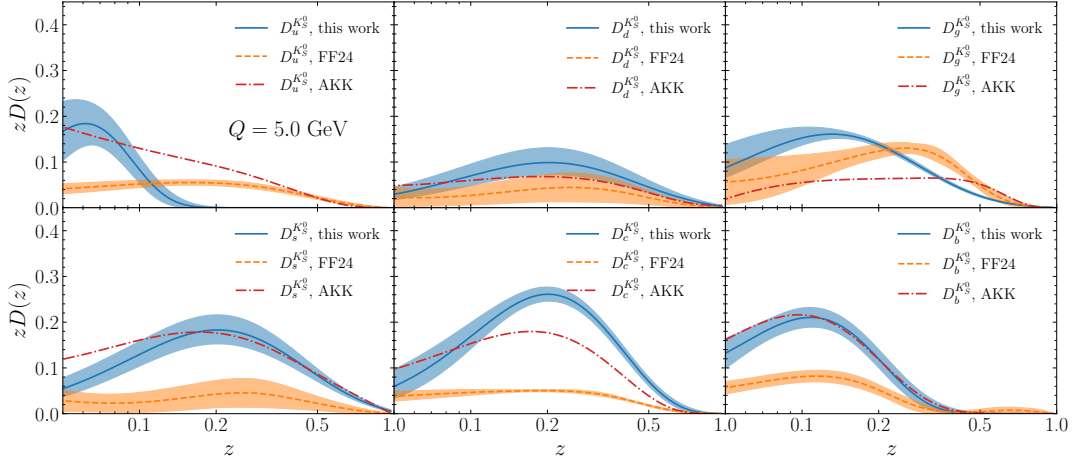


FIG. 38: Comparison of our K_S^0 FFs at $Q = 5$ GeV with AKK08 [67] and FF24 [83].

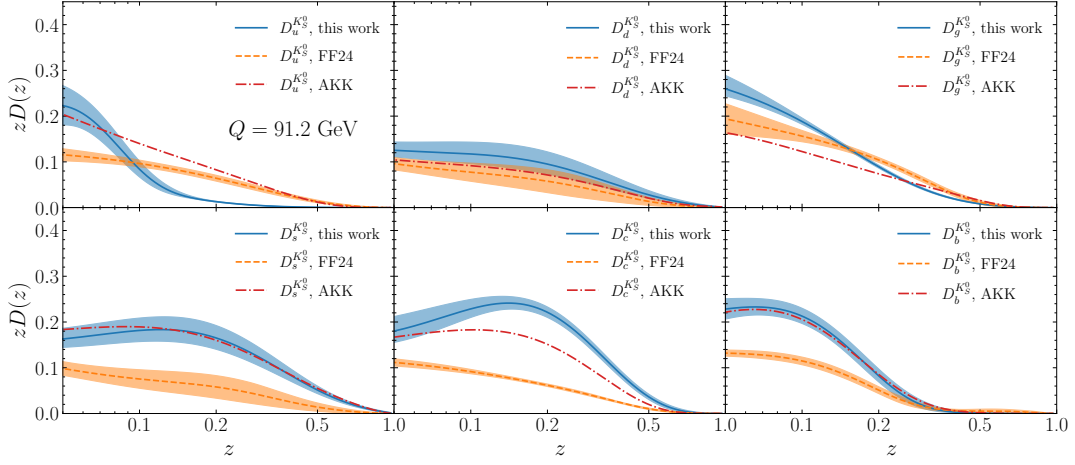


FIG. 39: Same as Fig. 38 but at $Q = 91.2$ GeV.

The comparison for K_S^0 with AKK08 [67] and FF24 [83] is given in Fig. 38, at $Q = 5$ GeV. The u quark distribution derived in this study exhibits a distinct peak at $z \approx 0.06$ and rapidly declines to zero as z increases. In contrast, the FF24 u distribution is more uniform, while the u quark distribution from AKK08 remains comparatively larger over the entire z range. For the d distribution, although our result tends to be larger than those of FF24 and AKK08, all three extractions are generally consistent within their respective uncertainties. The gluon distribution obtained in this work exhibits a peak around $z = 0.15$, whereas FF24 shows a peak around $z = 0.3$, and AKK08 remains relatively flat until $z \approx 0.5$. Regarding the distributions of s , c and b quarks, our results are in close agreement with those of AKK08, except for the c distribution in the intermediate and high z regions. In contrast, the FF24 results yield a smaller distribution across the entire z range. Finally, as illustrated in Fig. 39, when evolved to $Q = 91.2$ GeV, the shapes and magnitudes of the aforementioned distributions undergo some changes, but the relative behavior among them remains largely consistent.

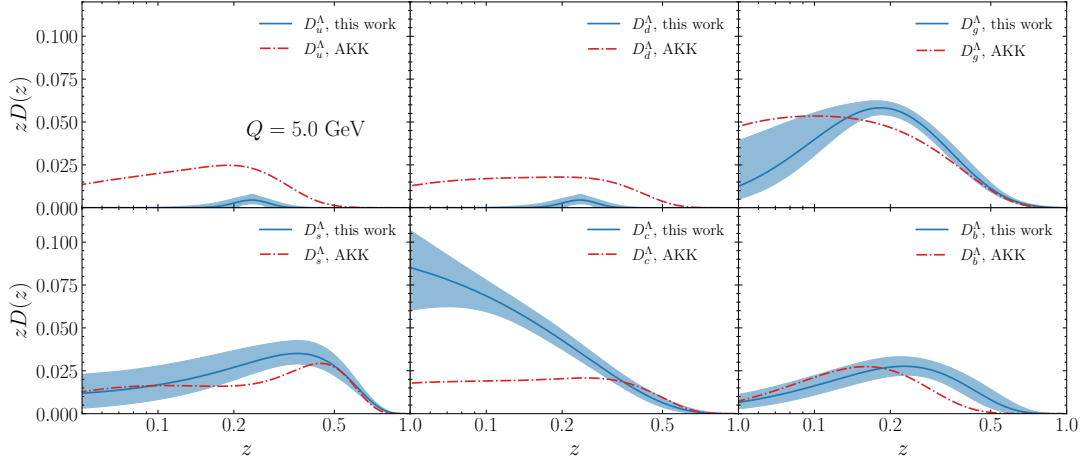


FIG. 40: Comparison of our Λ FFs at $Q = 5$ GeV with AKK08 [67].

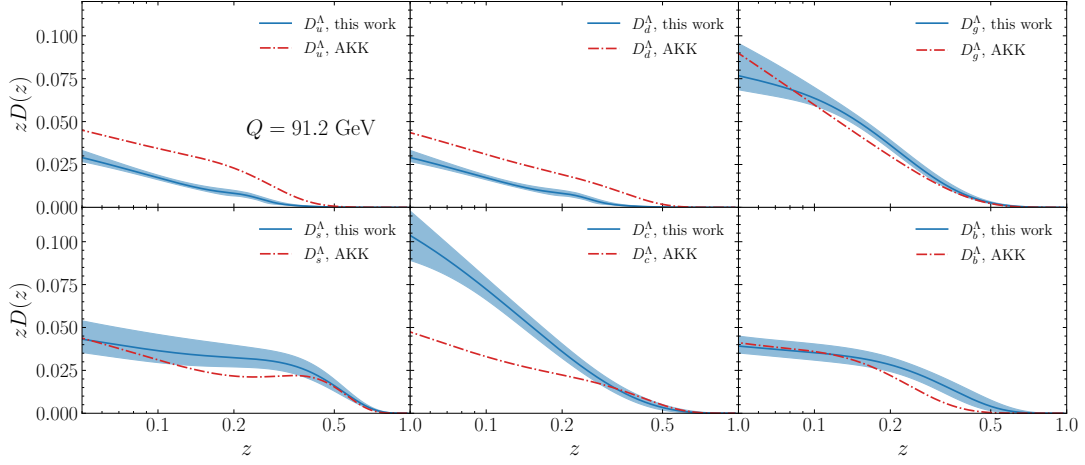


FIG. 41: Same as Fig. 40 but at $Q = 91.2$ GeV.

For Λ , the u and d quark distributions from AKK08 [67] are notably larger than those in this work, across the entire z range. As for the distributions of gluon, s and b quarks, the results from this work are in good agreement with those from AKK08, with some exception in the intermediate z region. Regarding the c quark distribution, a significant difference between our result and the AKK08 result is observed at low and intermediate z regions. However, some agreement is found in the large z region is observed for the c distribution. Again, as demonstrated in Fig. 41, when evolved to $Q = 91.2$ GeV, the shapes and magnitudes of the Λ FFs exhibit changes, but the relative behavior among them stays the same in general.

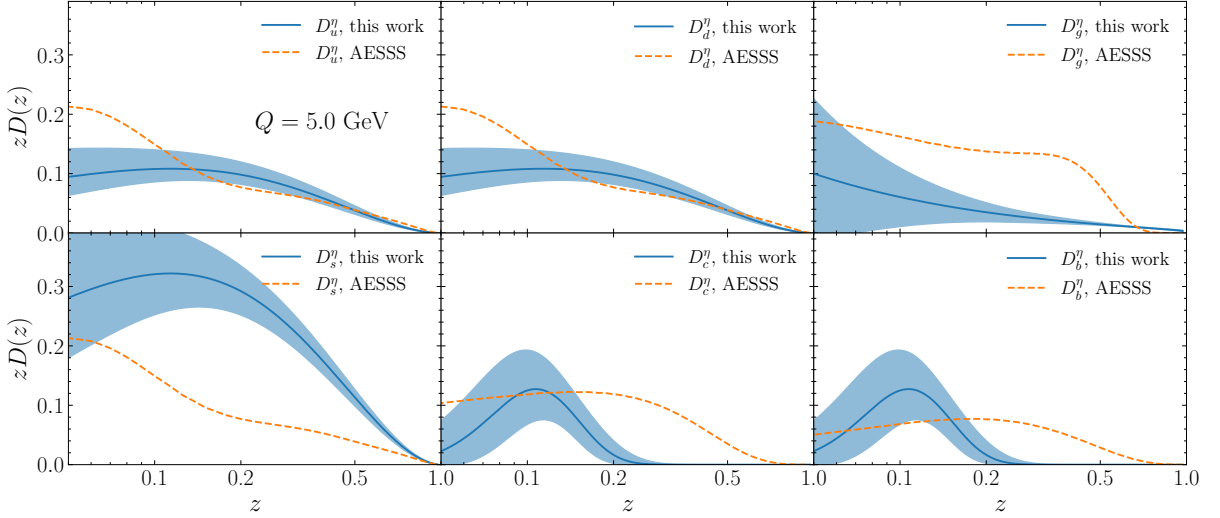


FIG. 42: Comparison of our η FFs at $Q = 5$ GeV with AESSS [84].

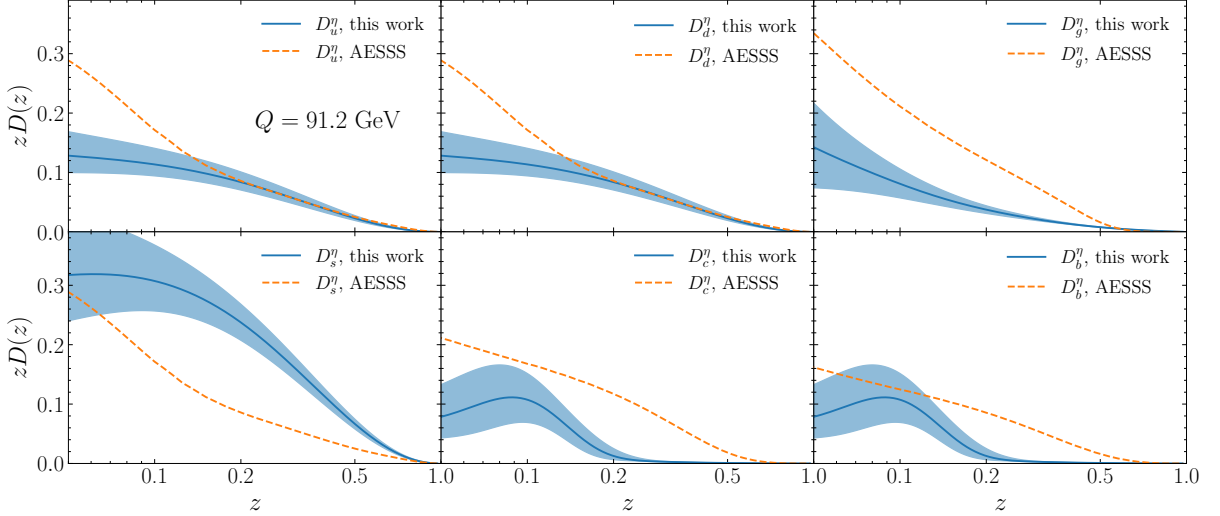


FIG. 43: Same as Fig. 42 but at $Q = 91.2$ GeV.

For the η FFs, the u and d quark distributions fitted in this work are in good agreement with those from AESSS [84] at $z \gtrsim 0.2$. In the lower z region, however, the u and d distributions obtained from AESSS are discernibly larger than those obtained in this work. As for the gluon distribution, we observe that the AESSS result is generally larger than that obtained in this work. On the contrary, the strange distribution obtained in this work is generally larger than that from AESSS, compensating the relative smallness of the gluon distribution fitted in this analysis. Furthermore, this study identifies the c and b quark distributions with a prominent peak at $z \approx 0.1$, whereas the corresponding AESSS distributions remain generally flat across the most of the z region before decreasing at $z \approx 0.3$. Finally, as shown in Fig. 43, when evolved to $Q = 91.2$ GeV, the shapes and magnitudes of the η FFs exhibit changes, but the relative behavior among them generally stays the same.

Appendix B: Impact of the Belle measurements

Recently, the Belle collaboration released a new set of measurements [148] for light and charmed mesons, including K_S^0 and η , which are of particular interest to us.

collaboration	year	\sqrt{s} [GeV]	χ^2	N_{pt}	χ^2/N_{pt}
ARGUS [125]	1990	9.46	21.79	6	3.63
HRS [124]	1988	29	34.35	13	2.64
JADE [121]	1985	34.4	7.13	2	3.57
JADE [122]	1990	35	0.57	3	0.19
CELLO [123]	1990	35	2.17	5	0.43
Belle [148]	2024	10.52	12.65	32	0.40
sum			78.66	61	1.29

TABLE XIX: The χ^2 , number of data points (N_{pt}) and χ^2/N_{pt} for the SIA datasets of η production with Belle dataset [148] added. Additional details, including information on collaboration, the year of publication, and center-of-mass energy, are also provided. Sum of χ^2 is also given for all the datasets listed in this table.

The experiment was conducted at center-of-mass energies of 10.58 GeV and 10.52 GeV, just below the threshold for b -quark production. The dataset features numerous data points with reduced uncertainties, making it a valuable resource for enhancing constraints and enabling more precise flavor separation.

In order to study the impact of the Belle data, we performed an additional fit under the same conditions as our baseline analysis, this time including the Belle data [148] alongside the existing dataset. After the inclusion of the Belle data, we found that the χ^2 values deteriorated for some datasets, particularly for the SIA data measured below the Z -pole energy, as listed in Table XIX. From the table, it is evident that the χ^2/N_{pt} has increased significantly for ARGUS [125], HRS [124] and JADE [121] compared to that in Table XVII. The Belle data, however, shows a good χ^2/N_{pt} of 0.4.

In Fig. 44, we present the experimental data normalized to theoretical predictions for the datasets listed in Table XIX. The legends used in this figure are the same as those in Fig. 25. From the figure, it can be seen that for most experiments (ARGUS at 9.46 GeV [125], HRS at 29 GeV [124] and JADE at 34.4 GeV [121]), the data points tends to lie below the theoretical predictions. In contrast, the Belle data points are generally above the theoretical predictions, with a deviation typically exceeding 10%. This indicates a significant tension between Belle and other low-energy SIA measurements.

Additionally, we compare the η FFs from our baseline fit with those from the alternative fit with Belle data included in Fig. 45. The Belle data appears to favor a larger u quark fragmentation while suppressing the s quark distribution compared to the baseline fit. For gluon fragmentation, although the central values exhibit suppression in the low z region and enhancement in the high z region, the two results are generally consistent within uncertainties. Finally, the c quark distribution remains generally unchanged even with inclusion of the Belle data.

Following the same procedure as for the η fragmentation, we conducted an alternative analysis incorporating the Belle K_S^0 production data [148]. We first list the χ^2 in Table XX. Comparing with χ^2 values from the baseline fit given in Table XV, we find that the fit quality of the SIA data below Z -pole generally stay the same. Additionally,

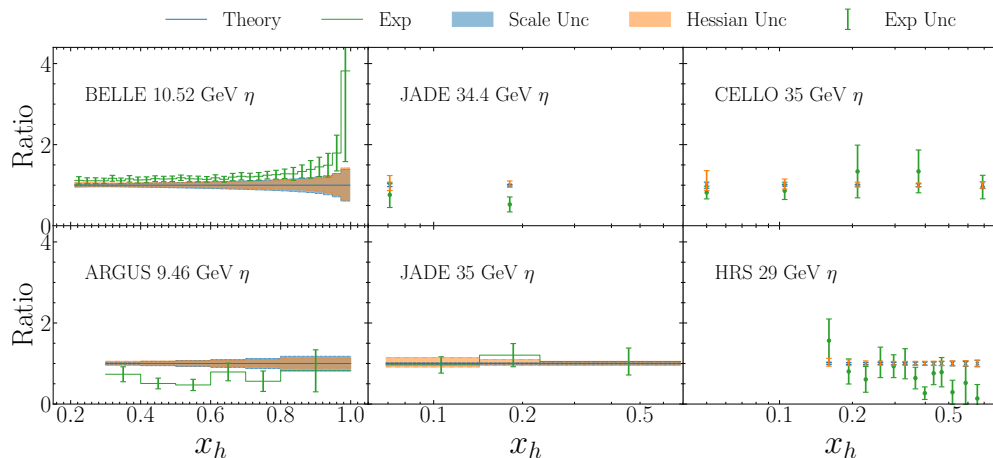


FIG. 44: Same as Fig. 25 but with inclusion of the Belle data [148].

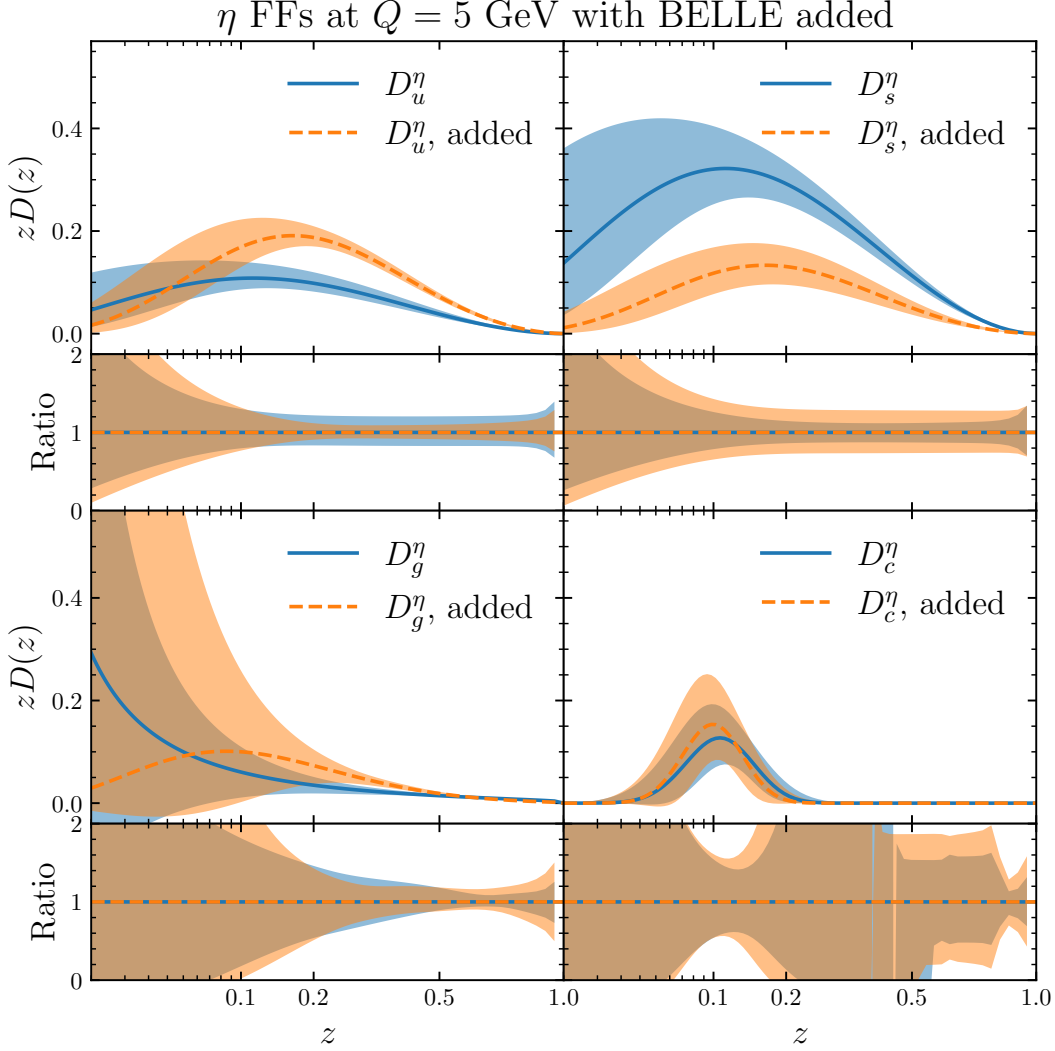


FIG. 45: Comparison of our nominal η FFs (blue) and the alternative fit (orange) with Belle data [148] added, at $Q = 5$ GeV. The setup of the plot follows the same as Fig. 1.

the Belle data [148] is well fitted with $\chi^2/N_{\text{pt}} = 0.43$. Consequently, the total χ^2/N_{pt} for the SIA below Z -pole is 1.04, indicating a good fit after inclusion of the Belle data.

In order to better visualize the fit quality with the Belle data added, we plot in Fig. 46 the experimental data normalized to theoretical predictions for the datasets listed in Table XX. Whereas the existing SIA data from the baseline fit are very well described, the Belle experimental data are still slightly underestimated by the theoretical predictions. The same behavior, however, is found for TASSO at 42.6 GeV [99] as well.

In Fig. 47, we present comparison of K_S^0 FFs from our baseline fit with those from the alternative fit with the Belle data added. It is evident that the changes in K_S^0 FFs are generally negligible and the distributions from the two scenarios are consistent within uncertainties.

In summary, due to the tension found between the η production data from Belle [148] and the other world data including ARGUS [125], HRS [124] and JADE [121], we decide not to include the Belle measurement in our nominal fit for η FFs. In order to maintain consistency with the η data selection and considering that the improvement in FFs is not substantial, we decided not to include the Belle K_S^0 data in our nominal results either.

collaboration	year	\sqrt{s} [GeV]	χ^2	N_{pt}	χ^2/N_{pt}
TASSO [98]	1985	14	5.12	9	0.57
TASSO [98]	1985	22	5.54	6	0.92
TASSO [98]	1985	34	14.86	13	1.14
TASSO [99]	1990	14.8	10.89	9	1.21
TASSO [99]	1990	21.5	3.40	6	0.57
TASSO [99]	1990	34.5	19.54	13	1.50
TASSO [99]	1990	35	13.52	13	1.04
TASSO [99]	1990	42.6	32.01	13	2.46
TPC [96]	1984	29	3.02	8	0.38
MARK II [97]	1985	29	11.06	17	0.65
HRS [100]	1987	29	36.33	12	3.03
CELLO [101]	1990	35	3.48	9	0.39
TOPAZ [102]	1995	58	0.18	4	0.05
BELLE [148]	2024	10.52	14.90	35	0.43
sum			173.85	167	1.04

TABLE XX: Same as Table XIX but for K_S^0 production in SIA below Z -pole.

Appendix C: Impact of the LHCb measurements

In this section, we examine the influence of the LHCb measurement for the η/π^0 production ratio $R(\eta/\pi^0)$ at 5.02 TeV and 13 TeV [149]. Here $R(\eta/\pi^0)$ is defined as:

$$R(\eta/\pi^0) \equiv \frac{d\sigma_\eta}{dp_T} \bigg/ \frac{d\sigma_{\pi^0}}{dp_T}, \quad (\text{C1})$$

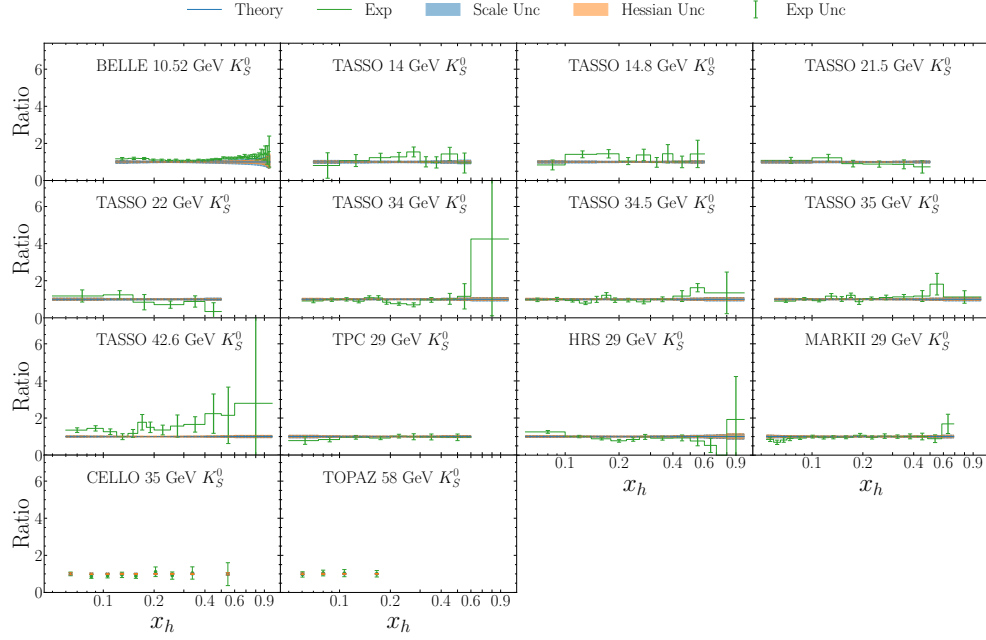


FIG. 46: Same as Fig. 17 but with inclusion of the Belle data [148].

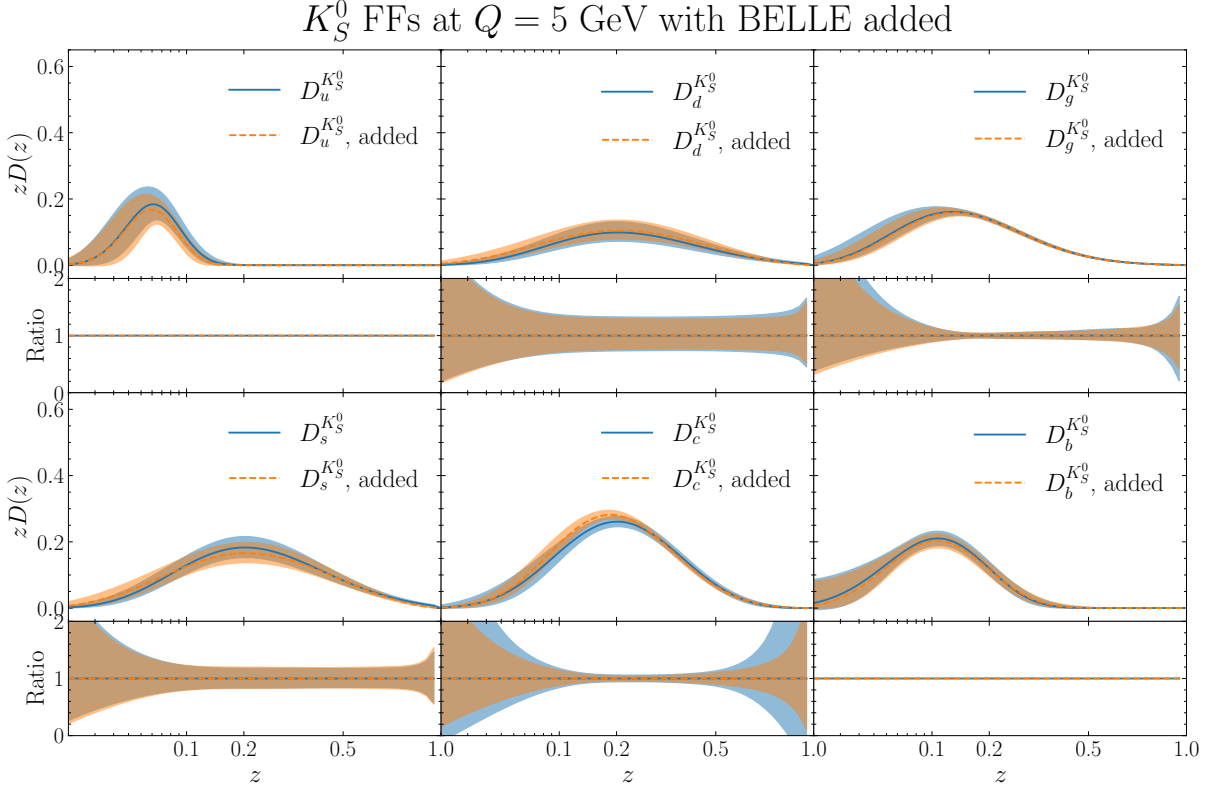


FIG. 47: Comparison of our nominal K_S^0 FFs (blue) and the alternative fit (orange) with Belle data [148] added, at $Q = 5$ GeV. The setup of the plot follows the same as Fig. 1.

First, we provide theoretical predictions for the LHCb data using the nominal NPC23 η and π^0 FFs. Then we assess the impact of this measurement by including it in an alternative fit.

Figs. 48 and 49 display the comparison between theoretical predictions and experimental data for center-of-mass energies of 5.02 TeV and 13 TeV, respectively. The theoretical predictions are drawn with solid blue lines, along with their corresponding uncertainty bands. The Hessian uncertainties at the 68% confidence level are represented by orange bands, while the scale uncertainties are shown as blue bands. The scale uncertainty is calculated following the approach outlined in Section III B. The experimental values and uncertainties are shown as green error bars, which incorporates both statistical and systematic uncertainties. In the FMNLO grid generation, the renormalization and factorization scales are chosen as $\mu_R = \mu_F = p_T$, where p_T denotes the transverse momentum of the identified hadron (η or π^0 in this case). This choice leads to enhanced scale uncertainties in the low- p_T region ($p_T < 6$ GeV), where the more pronounced running of the strong coupling constant at lower energy scales results in larger variations.

A systematic trend is observed across all rapidity regions and collision energies, with theoretical predictions consistently overestimating the η/π^0 ratio compared to the experimental data. This discrepancy can be attributed to the sensitivity of the theoretical calculations to the choice of factorization, renormalization and fragmentation scales, as reflected by the large scale uncertainties in Figs. 48 and 49.

At the center-of-mass energy of 13 TeV (Fig. 48), the theoretical predictions demonstrate good agreement with the experimental data across the entire p_T range. The theoretical calculations consistently fall within the experimental uncertainties, indicating robust compatibility between theory and experiment at $\sqrt{s} = 13$ TeV. Additionally, the experimental data reveals no significant rapidity dependence in the η/π^0 ratios at $\sqrt{s} = 13$ TeV.

At the center-of-mass energy of 5.02 TeV (Fig. 49), the theoretical predictions remain stable across both rapidity intervals. However, they consistently overestimate the experimental values by approximately 30%. The agreement is better in the intermediate p_T region compared to both low and high p_T ends. This behavior is observed in both rapidity ranges that are considered in Fig. 49.

We further present a detailed comparison of the differential cross section for η production as a function of transverse momentum p_T between theoretical predictions and experimental measurements at center-of-mass energies of 5.02 TeV and 7 TeV, covering rapidity regions $y \in (2.5, 3.5)$ and $y \in (-4, -3)$. The results are presented in Figs. 50 and 51.

The upper panels of these figures display the differential cross sections, while the lower panels depict the data

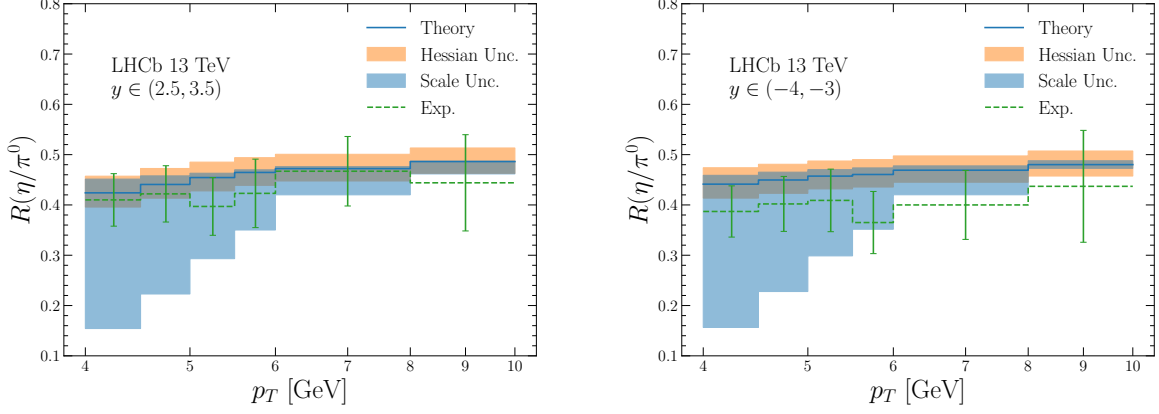


FIG. 48: Comparison between the theoretical predictions generated with the NPC nominal FFs and the experimental data from LHCb [149] at a center-of-mass energy of 13 TeV. The left and right panels correspond the rapidity regions $y \in (2.5, 3.5)$ and $y \in (-4, -3)$, respectively. The data and experimental uncertainties are shown in green error bars, while the scale and Hessian uncertainties are shown in blue and orange bands, respectively.

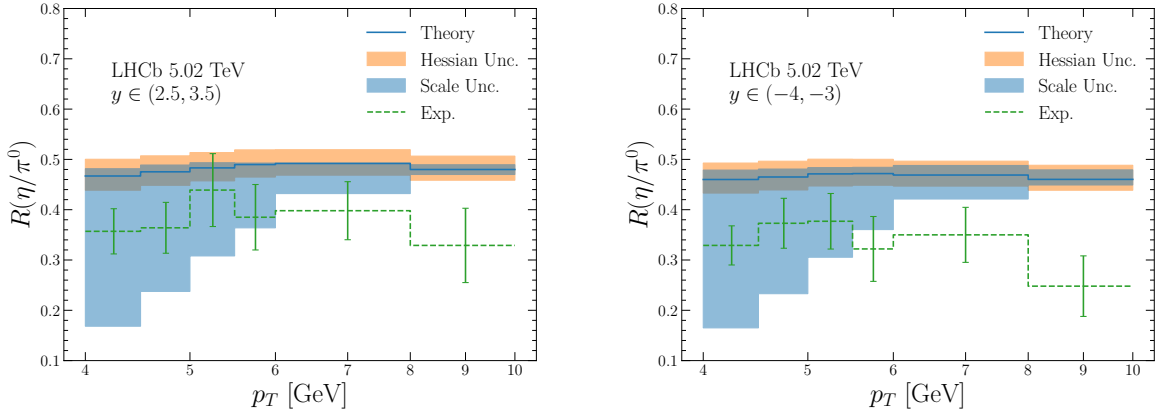


FIG. 49: Same as Fig. 48 but at $\sqrt{s} = 5.02$ TeV.

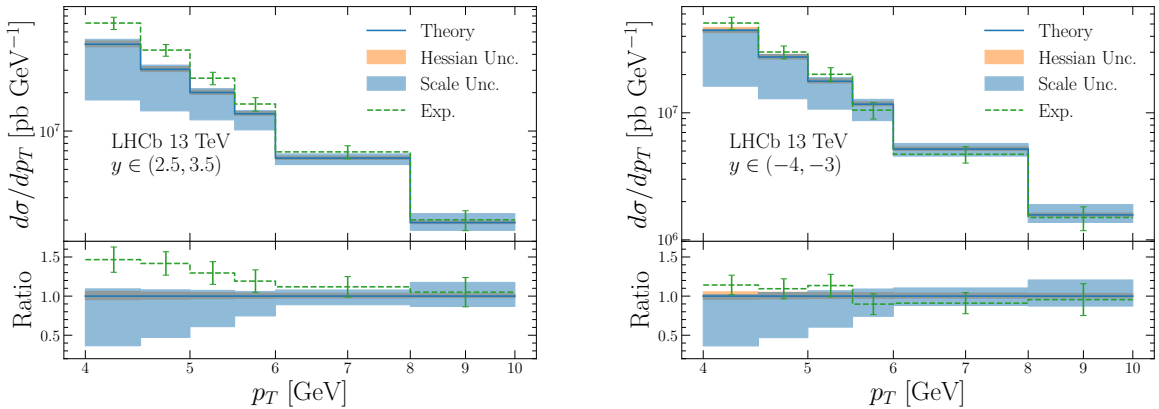


FIG. 50: Comparison of the differential cross section for η production as a function of transverse momentum p_T between theoretical predictions and experimental measurements at a center-of-mass energy of 13 TeV. The left and right panels correspond the rapidity regions $y \in (2.5, 3.5)$ and $y \in (-4, -3)$, respectively. The lower panels display the experimental data normalized to the central value of the theoretical predictions.

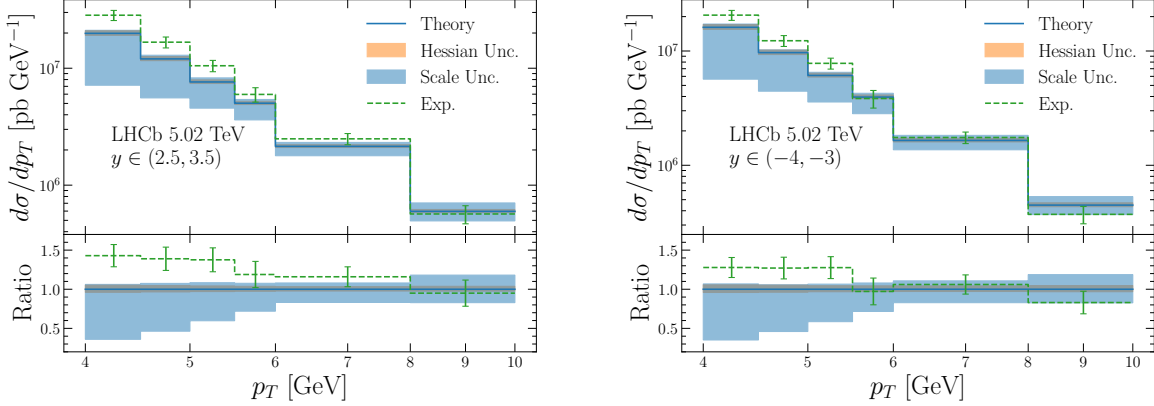


FIG. 51: Same as Fig. 50 but at $\sqrt{s} = 5.02$ TeV.

collaboration	year	\sqrt{s} [GeV]	χ^2	N_{pt}	χ^2/N_{pt}
LHCb forward [149]	2024	5020	5.06	6	0.84
LHCb forward [149]	2024	13000	0.60	6	0.10
LHCb backward [149]	2024	5020	13.08	6	2.18
LHCb backward [149]	2024	13000	1.42	6	0.24
sum			20.16	24	0.84

TABLE XXI: The χ^2 , number of data points (N_{pt}) and χ^2/N_{pt} for LHCb η production data with LHCb dataset [149] added. The terms “forward” and “backward” denote rapidity bins $y \in (2.5, 3.5)$ and $y \in (-4, -3)$, respectively. Additional details, including information on collaboration, the year of publication, and center-of-mass energy, are also provided. Sum of χ^2 is also given for all the datasets listed in this table.

normalized to the central value of the theoretical predictions. At both collision energies, the theoretical curves agree well with experimental data in the high- p_T region. However, discernible deviations appear at low- p_T region, particularly in the rapidity region $y \in (2.5, 3.5)$, where the theoretical predictions overestimate the experimental data by approximately 40% ~ 50% for both collision energies. This discrepancy is accompanied by significant scale uncertainties in this kinematic region, which further highlights the sensitivity of the theoretical calculations to the choice of factorization and renormalization scales.

In contrast, better agreement at low- p_T region is observed for the rapidity region $y \in (-4, -3)$. At 5.02 TeV, the theoretical predictions overestimate the experimental data by approximately 30% ~ 40% in the low- p_T bins. At 7 TeV, the agreement further improves, where experimental measurements and theoretical calculations overlap within their uncertainty bands across the entire p_T region.

These findings demonstrate the robustness of the theoretical framework in describing η production, particularly at high p_T and larger collision energies. However, the persistent discrepancies at lower p_T values suggest areas for further refinement, particularly in addressing scale uncertainties and optimizing the treatment of low- p_T dynamics.

To further investigate the influence of the LHCb data on our analysis, we performed an alternative fit under identical conditions as our baseline analysis, incorporating only the LHCb data [149] in addition. The inclusion of the LHCb data resulted in minimal changes to the overall χ^2 values. The χ^2 values for newly added sets are provided in Table XXI.

As shown in Table XXI, a good quality fit is achieved for the LHCb datasets, with a total $\chi^2/N_{\text{pt}} = 0.84$. However, the LHCb data measured in the backward rapidity region ($\eta \in (-4, -3)$) exhibits a slightly worse agreement, with $\chi^2/N_{\text{pt}} = 2.18$. In addition, the inclusion of the LHCb datasets only slightly deteriorates the fit quality of the global datasets, resulting in an increase of χ^2 by 5.22 units.

In Fig. 52, we present the experimental data normalized to the central values of the theoretical predictions for the LHCb datasets listed in Table XXI. The plot compares the measured and theoretically computed η/π^0 production ratios at center-of-mass energies 5.02 TeV and 13 TeV in both forward and backward rapidity regions. The legends used in this figure are consistent with those in Fig. 26.

By comparing with Figs. 48 and 49, it is clear that the agreement between theory and experimental data improves

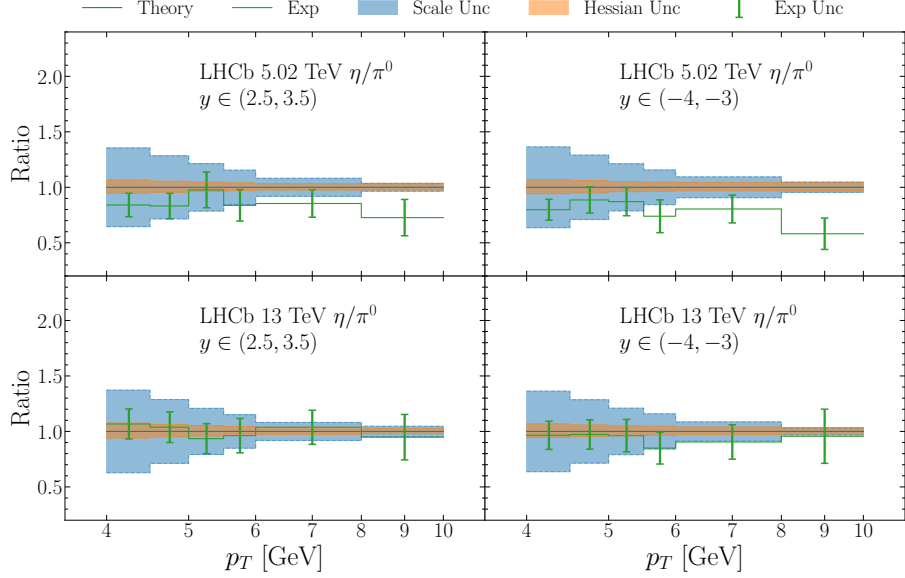


FIG. 52: Same as Fig. 25 but for LHCb data on production ratio of η/π^0 with inclusion of the LHCb data [149] on top of the baseline fit.

significantly after incorporating the LHCb data into the fit. The 13 TeV measurements now show excellent consistency, while discrepancies at 5 TeV are substantially reduced. Nevertheless, in the high p_T region, deviation between the theoretical predictions and the experimental data is still observed at $\sqrt{s} = 5.02$ GeV.

Furthermore, in Fig. 53, we compare the η FFs obtained from our baseline fit with those derived from the alternative fit that includes the LHCb data. The inclusion of the LHCb data only resulted in minor impact on the FFs. Specifically, the u -quark and gluon fragmentation functions are slightly suppressed compared to the baseline fit, while the s -quark and c -quark distributions are moderately enhanced. Importantly, all variations remain within the original uncertainty bands. A notable observation is the reduction in uncertainties for the gluon distribution in the low z region, suggesting that the LHCb measurements provide valuable constraints on gluon FFs.

In summary, the addition of the LHCb data yields results that are consistent with our baseline fit. Although the overall improvements are modest, the enhanced constraints on the gluon fragmentation function, particularly in the low z region, underscore the importance of LHCb measurements in probing gluon dynamics.

Appendix D: LHAPDF6 grid

In this section, we provide a brief summary of the files containing our fragmentation functions. Interpolation tables of the NPC23 neutral hadron FFs follow the LHAGRID1 format [150], which is the same format employed in PDF grid files. Access to the FFs is facilitated through the unified interface of LHAPDF6, available via Fortran, C++ and Python code. To use these sets, one can extract them into the LHAPDF data directory, accessible through the `lhpdf --datadir` command or direct download directly from the website [152].

The FFs fitted (or constructed via isospin symmetry) in this work correspond to partons fragmenting into various hadrons including K_S^0 , Λ , η and π^0 . They are named as NPC23_KAOS_nlo, NPC23_Lambda_nlo, NPC23_Eta_nlo and NPC23_PIO_nlo, respectively. In addition, we provide the K_S^0 FFs constructed from K^\pm FFs via isospin symmetry, as given in Eqs. (1) and (2), under the name NPC23_KAOS_nlo_iso.

The FF sets NPC23_KAOS_nlo, NPC23_Lambda_nlo, NPC23_Eta_nlo, NPC23_PIO_nlo and NPC23_KAOS_nlo_iso consist of 41, 37, 25, 127 and 127 subsets, respectively. The zeroth subset is the central set, while the remaining subsets correspond to the Hessian error sets. For the estimation of FFs uncertainties of any observable X , the

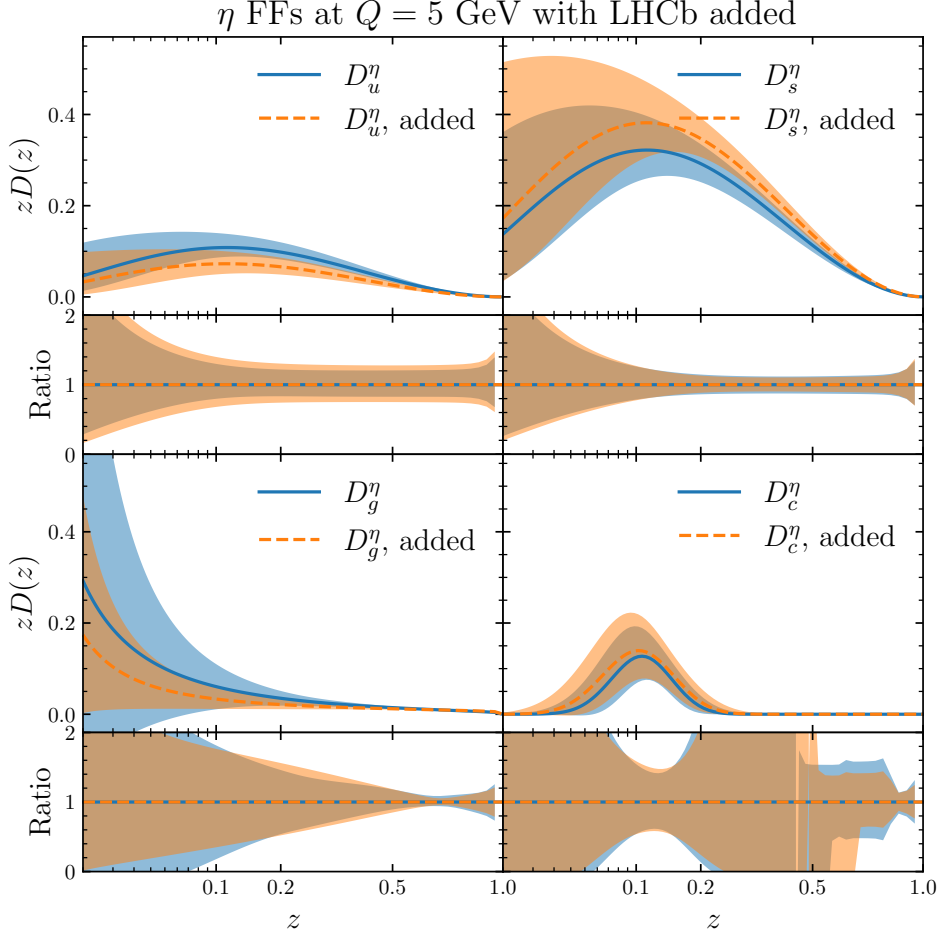


FIG. 53: Comparison of our nominal η FFs (blue) and the alternative fit (orange) with LHCb data [149] added, at $Q = 5$ GeV. The setup of the plot follows the same as Fig. 1.

following formula for asymmetric errors is employed [151]:

$$\delta^+ X = \sqrt{\sum_{i=1}^{N_d} [\max(X_{2i-1} - X_0, X_{2i} - X_0, 0)]^2}, \quad (D1)$$

$$\delta^- X = \sqrt{\sum_{i=1}^{N_d} [\max(X_0 - X_{2i-1}, X_0 - X_{2i}, 0)]^2}.$$

Here, X_0 represents the prediction obtained with the central set of FFs, and $X_{2i-1}(X_{2i})$ represents the predictions obtained with the error set for the i -th eigenvector in positive (negative) direction. When dealing with observables involving FFs of different hadrons, it is crucial to consider their correlations. In particular, the π^0 FFs and K_S^0 FFs constructed via isospin symmetry, namely NPC23_PI0_nlo and NPC23_KA0S_nlo_iso, are correlated with each other, as well as with the charged hadron FFs fitted in the previous NPC work [44]. However, the K_S^0 , Λ and η FFs are not inter-correlated, nor are they correlated with the other FFs from the current and previous NPC analyses. As an example, when calculating ratios between π^0 FFs and K^\pm FFs, it is essential to first compute the ratios using consistent error sets for π^0 and K^\pm . Afterward, the uncertainties can be estimated by applying Eq. (D1). This ensures that the correlations between the π^0 and K^\pm FFs are properly accounted for in the uncertainty estimation.

Our FFs grids are provided as 2-dimensional interpolation tables evaluated at different momentum fractions z and different fragmentation scales Q . The z values range from 0.003 to 1 with 99 nodes, while Q spans from 4 to 4000 GeV with 32 nodes in total. Our grids also include numerical values of α_S with $\alpha_S(m_Z) = 0.118$ and two-loop running. The number of active quark flavors is fixed to 5. The interpolator is configured to use the default log-cubic method, and the FFs are frozen when exceeding the specified ranges of z or Q mentioned above.

-
- [1] S. M. Berman, J. D. Bjorken, and J. B. Kogut, *Phys. Rev. D* **4**, 3388 (1971).
[2] R. D. Field and R. P. Feynman, *Nucl. Phys. B* **136**, 1 (1978).
[3] R. P. Feynman, R. D. Field, and G. C. Fox, *Phys. Rev. D* **18**, 3320 (1978).
[4] A. Metz and A. Vossen, *Prog. Part. Nucl. Phys.* **91**, 136 (2016), 1607.02521.
[5] J. C. Collins, D. E. Soper, and G. F. Sterman, *Adv. Ser. Direct. High Energy Phys.* **5**, 1 (1989), hep-ph/0409313.
[6] J. Collins, *Foundations of Perturbative QCD*, vol. 32 (Cambridge University Press, 2023), ISBN 978-1-109-40184-5, 978-1-109-40183-8, 978-1-109-40182-1.
[7] H. T. Li, I. Vitev, and Y. J. Zhu, *JHEP* **11**, 051 (2020), 2006.02437.
[8] Z.-B. Kang, J. Penttala, F. Zhao, and Y. Zhou, *Phys. Rev. D* **109**, 094012 (2024), 2311.17142.
[9] Z.-B. Kang, S. Lee, J. Penttala, F. Zhao, and Y. Zhou (2024), 2410.02747.
[10] R. Sassot, M. Stratmann, and P. Zurita, *Phys. Rev. D* **81**, 054001 (2010), 0912.1311.
[11] P. Zurita (2021), 2101.01088.
[12] M. Soleymaninia, H. Hashamipour, H. Khanpour, S. Shoeibi, and A. Mohamaditabar, *Eur. Phys. J. Plus* **139**, 794 (2024), 2305.02664.
[13] M. Doradau, R. T. Martinez, R. Sassot, and M. Stratmann, *Phys. Rev. D* **111**, 034045 (2025), 2411.08222.
[14] Z.-B. Kang, J. Terry, A. Vossen, Q. Xu, and J. Zhang, *Phys. Rev. D* **105**, 094033 (2022), 2108.05383.
[15] T. Li, H. Xing, and D.-B. Zhang (2024), 2406.05683.
[16] S. Grienering and I. Zahed (2024), 2406.01891.
[17] P. J. Rijken and W. L. van Neerven, *Phys. Lett. B* **386**, 422 (1996), hep-ph/9604436.
[18] P. J. Rijken and W. L. van Neerven, *Nucl. Phys. B* **487**, 233 (1997), hep-ph/9609377.
[19] A. Mitov and S.-O. Moch, *Nucl. Phys. B* **751**, 18 (2006), hep-ph/0604160.
[20] J. Blumlein and V. Ravindran, *Nucl. Phys. B* **749**, 1 (2006), hep-ph/0604019.
[21] M. Cacciari and S. Catani, *Nucl. Phys. B* **617**, 253 (2001), hep-ph/0107138.
[22] S. Moch and A. Vogt, *Phys. Lett. B* **680**, 239 (2009), 0908.2746.
[23] Z. Xu and H. X. Zhu (2024), 2411.11595.
[24] G. Altarelli, R. K. Ellis, G. Martinelli, and S.-Y. Pi, *Nucl. Phys. B* **160**, 301 (1979).
[25] P. Nason and B. R. Webber, *Nucl. Phys. B* **421**, 473 (1994), [Erratum: *Nucl.Phys.B* 480, 755 (1996)].
[26] W. Furmanski and R. Petronzio, *Z. Phys. C* **11**, 293 (1982).
[27] D. Graudenz, *Nucl. Phys. B* **432**, 351 (1994), hep-ph/9406274.
[28] D. de Florian, M. Stratmann, and W. Vogelsang, *Phys. Rev. D* **57**, 5811 (1998), hep-ph/9711387.
[29] D. de Florian and Y. Rotstein Habarnau, *Eur. Phys. J. C* **73**, 2356 (2013), 1210.7203.
[30] S. Goyal, S.-O. Moch, V. Pathak, N. Rana, and V. Ravindran, *Phys. Rev. Lett.* **132**, 251902 (2024), 2312.17711.
[31] L. Bonino, T. Gehrmann, and G. Stagnitto, *Phys. Rev. Lett.* **132**, 251901 (2024), 2401.16281.
[32] M. Abele, D. de Florian, and W. Vogelsang, *Phys. Rev. D* **104**, 094046 (2021), 2109.00847.
[33] M. Abele, D. de Florian, and W. Vogelsang, *Phys. Rev. D* **106**, 014015 (2022), 2203.07928.
[34] F. Aversa, P. Chiappetta, M. Greco, and J. P. Guillet, *Nucl. Phys. B* **327**, 105 (1989).
[35] D. de Florian, *Phys. Rev. D* **67**, 054004 (2003), hep-ph/0210442.
[36] B. Jager, A. Schafer, M. Stratmann, and W. Vogelsang, *Phys. Rev. D* **67**, 054005 (2003), hep-ph/0211007.
[37] M. Czakon, T. Generet, A. Mitov, and R. Poncelet (2025), 2503.11489.
[38] Z.-B. Kang, F. Ringer, and I. Vitev, *JHEP* **11**, 155 (2016), 1606.07063.
[39] T. Kaufmann, X. Liu, A. Mukherjee, F. Ringer, and W. Vogelsang, *JHEP* **02**, 040 (2020), 1910.11746.
[40] Z.-B. Kang, K. Lee, J. Terry, and H. Xing, *Phys. Lett. B* **798**, 134978 (2019), 1906.07187.
[41] L. Wang, Z.-B. Kang, H. Xing, and B.-W. Zhang, *Phys. Rev. D* **103**, 054043 (2021), 2003.03796.
[42] D. P. Anderle, T. Kaufmann, M. Stratmann, F. Ringer, and I. Vitev, *Phys. Rev. D* **96**, 034028 (2017), 1706.09857.
[43] J. Gao, C. Liu, X. Shen, H. Xing, and Y. Zhao, *Phys. Rev. Lett.* **132**, 261903 (2024), 2401.02781.
[44] J. Gao, C. Liu, X. Shen, H. Xing, and Y. Zhao (2024), 2407.04422.
[45] F. Arleo, M. Fontannaz, J.-P. Guillet, and C. L. Nguyen, *JHEP* **04**, 147 (2014), 1311.7356.
[46] C. Liu, X. Shen, B. Zhou, and J. Gao, *JHEP* **09**, 108 (2023), 2305.14620.
[47] M. S. Zidi, J. P. Guillet, I. Schienbein, and H. Zaraket, *Eur. Phys. J. C* **84**, 611 (2024), 2403.14574.
[48] S. Caletti, A. Gehrmann-De Ridder, A. Huss, A. R. Garcia, and G. Stagnitto, *JHEP* **10**, 027 (2024), 2405.17540.
[49] L. Bonino, T. Gehrmann, M. Marcoli, R. Schürmann, and G. Stagnitto, *JHEP* **08**, 073 (2024), 2406.09925.
[50] A. Mitov, S. Moch, and A. Vogt, *Phys. Lett. B* **638**, 61 (2006), hep-ph/0604053.
[51] S. Moch and A. Vogt, *Phys. Lett. B* **659**, 290 (2008), 0709.3899.
[52] A. A. Almasy, S. Moch, and A. Vogt, *Nucl. Phys. B* **854**, 133 (2012), 1107.2263.

- [53] H. Chen, T.-Z. Yang, H. X. Zhu, and Y. J. Zhu, *Chin. Phys. C* **45**, 043101 (2021), 2006.10534.
- [54] M. A. Ebert, B. Mistlberger, and G. Vita, *JHEP* **07**, 121 (2021), 2012.07853.
- [55] M.-x. Luo, T.-Z. Yang, H. X. Zhu, and Y. J. Zhu, *JHEP* **06**, 115 (2021), 2012.03256.
- [56] J. Binnewies, B. A. Kniehl, and G. Kramer, *Z. Phys. C* **65**, 471 (1995), hep-ph/9407347.
- [57] J. Binnewies, B. A. Kniehl, and G. Kramer, *Phys. Rev. D* **52**, 4947 (1995), hep-ph/9503464.
- [58] B. A. Kniehl, G. Kramer, and B. Potter, *Nucl. Phys. B* **582**, 514 (2000), hep-ph/0010289.
- [59] L. Bourhis, M. Fontannaz, J. P. Guillet, and M. Werlen, *Eur. Phys. J. C* **19**, 89 (2001), hep-ph/0009101.
- [60] S. Kretzer, *Phys. Rev. D* **62**, 054001 (2000), hep-ph/0003177.
- [61] S. Kretzer, E. Leader, and E. Christova, *Eur. Phys. J. C* **22**, 269 (2001), hep-ph/0108055.
- [62] D. de Florian, R. Sassot, and M. Stratmann, *Phys. Rev. D* **76**, 074033 (2007), 0707.1506.
- [63] D. de Florian, R. Sassot, M. Epele, R. J. Hernández-Pinto, and M. Stratmann, *Phys. Rev. D* **91**, 014035 (2015), 1410.6027.
- [64] D. de Florian, M. Epele, R. J. Hernandez-Pinto, R. Sassot, and M. Stratmann, *Phys. Rev. D* **95**, 094019 (2017), 1702.06353.
- [65] I. Borsa, D. de Florian, R. Sassot, and M. Stratmann, *Phys. Rev. D* **105**, L031502 (2022), 2110.14015.
- [66] M. Hirai, S. Kumano, T. H. Nagai, and K. Sudoh, *Phys. Rev. D* **75**, 094009 (2007), hep-ph/0702250.
- [67] S. Albino, B. A. Kniehl, and G. Kramer, *Nucl. Phys. B* **803**, 42 (2008), 0803.2768.
- [68] V. Bertone, N. P. Hartland, E. R. Nocera, J. Rojo, and L. Rottoli (NNPDF), *Eur. Phys. J. C* **78**, 651 (2018), 1807.03310.
- [69] R. A. Khalek, V. Bertone, and E. R. Nocera (MAP (Multi-dimensional Analyses of Partonic distributions)), *Phys. Rev. D* **104**, 034007 (2021), 2105.08725.
- [70] E. Moffat, W. Melnitchouk, T. C. Rogers, and N. Sato (Jefferson Lab Angular Momentum (JAM)), *Phys. Rev. D* **104**, 016015 (2021), 2101.04664.
- [71] J. Gao, X. Shen, H. Xing, Y. Zhao, and B. Zhou (2025), 2502.17837.
- [72] D. P. Anderle, F. Ringer, and M. Stratmann, *Phys. Rev. D* **92**, 114017 (2015), 1510.05845.
- [73] V. Bertone, S. Carrazza, N. P. Hartland, E. R. Nocera, and J. Rojo (NNPDF), *Eur. Phys. J. C* **77**, 516 (2017), 1706.07049.
- [74] M. Soleymaninia, M. Goharipour, and H. Khanpour, *Phys. Rev. D* **98**, 074002 (2018), 1805.04847.
- [75] M. Soleymaninia, M. Goharipour, H. Khanpour, and H. Spiesberger, *Phys. Rev. D* **103**, 054045 (2021), 2008.05342.
- [76] H. Abdolmaleki, M. Soleymaninia, H. Khanpour, S. Amoroso, F. Giuli, A. Glazov, A. Luszczak, F. Olness, and O. Zenaïev (xfitter Developers' Team), *Phys. Rev. D* **104**, 056019 (2021), 2105.11306.
- [77] I. Borsa, R. Sassot, D. de Florian, M. Stratmann, and W. Vogelsang, *Phys. Rev. Lett.* **129**, 012002 (2022), 2202.05060.
- [78] R. Abdul Khalek, V. Bertone, A. Khouli, and E. R. Nocera (MAP (Multi-dimensional Analyses of Partonic distributions)), *Phys. Lett. B* **834**, 137456 (2022), 2204.10331.
- [79] J. Binnewies, B. A. Kniehl, and G. Kramer, *Phys. Rev. D* **53**, 3573 (1996), hep-ph/9506437.
- [80] S. Albino, B. A. Kniehl, and G. Kramer, *Nucl. Phys. B* **734**, 50 (2006), hep-ph/0510173.
- [81] M. Soleymaninia, H. Abdolmaleki, and H. Khanpour, *Phys. Rev. D* **102**, 114029 (2020), 2009.08139.
- [82] M. Li, D. P. Anderle, H. Xing, and Y. Zhao (2024), 2404.11527.
- [83] M. Soleymaninia, H. Hashamipour, M. Salajegheh, H. Khanpour, H. Spiesberger, and U.-G. Meißner, *Phys. Rev. D* **110**, 014019 (2024), 2404.07334.
- [84] C. A. Aidala, F. Ellinghaus, R. Sassot, J. P. Seele, and M. Stratmann, *Phys. Rev. D* **83**, 034002 (2011), 1009.6145.
- [85] H. Abramowicz et al. (ZEUS), *JHEP* **03**, 020 (2012), 1111.3526.
- [86] B. Zhou and J. Gao (2024), 2407.10059.
- [87] K. Abe et al. (SLD), *Phys. Rev. D* **59**, 052001 (1999), hep-ex/9805029.
- [88] K.-B. Chen, Z.-T. Liang, Y.-L. Pan, Y.-K. Song, and S.-Y. Wei, *Phys. Lett. B* **816**, 136217 (2021), 2102.00658.
- [89] K.-b. Chen, Z.-t. Liang, Y.-k. Song, and S.-y. Wei, *Phys. Rev. D* **105**, 034027 (2022), 2108.07740.
- [90] N. Sato, J. J. Ethier, W. Melnitchouk, M. Hirai, S. Kumano, and A. Accardi, *Phys. Rev. D* **94**, 114004 (2016), 1609.00899.
- [91] G. Alexander et al. (OPAL), *Phys. Lett. B* **264**, 467 (1991).
- [92] R. Akers et al. (OPAL), *Z. Phys. C* **67**, 389 (1995).
- [93] G. Abbiendi et al. (OPAL), *Eur. Phys. J. C* **17**, 373 (2000), hep-ex/0007017.
- [94] R. Barate et al. (ALEPH), *Phys. Rept.* **294**, 1 (1998).
- [95] P. Abreu et al. (DELPHI), *Z. Phys. C* **65**, 587 (1995).
- [96] H. Aihara et al. (TPC/Two Gamma), *Phys. Rev. Lett.* **53**, 2378 (1984).
- [97] H. Schellman et al., *Phys. Rev. D* **31**, 3013 (1985).
- [98] M. Althoff et al. (TASSO), *Z. Phys. C* **27**, 27 (1985).
- [99] W. Braunschweig et al. (TASSO), *Z. Phys. C* **47**, 167 (1990).
- [100] M. Derrick et al., *Phys. Rev. D* **35**, 2639 (1987).
- [101] H. J. Behrend et al. (CELLO), *Z. Phys. C* **46**, 397 (1990).
- [102] R. Itoh et al. (TOPAZ), *Phys. Lett. B* **345**, 335 (1995), hep-ex/9412015.
- [103] R. Barate et al. (ALEPH), *Eur. Phys. J. C* **16**, 613 (2000).
- [104] P. Abreu et al. (DELPHI), *Eur. Phys. J. C* **18**, 203 (2000), [Erratum: *Eur.Phys.J.C* 25, 493 (2002)], hep-ex/0103031.
- [105] G. Abbiendi et al. (OPAL), *Eur. Phys. J. C* **16**, 407 (2000), hep-ex/0001054.
- [106] M. Ablikim et al. (BESIII), *Phys. Rev. Lett.* **130**, 231901 (2023), 2211.11253.
- [107] M. Ablikim et al. (BESIII) (2025), 2502.16084.
- [108] S. Acharya et al. (ALICE), *Eur. Phys. J. C* **81**, 256 (2021), 2005.11120.
- [109] P. Abreu et al. (DELPHI), *Phys. Lett. B* **318**, 249 (1993).
- [110] D. Buskulic et al. (ALEPH), *Z. Phys. C* **64**, 361 (1994).

- [111] G. Alexander et al. (OPAL), *Z. Phys. C* **73**, 569 (1997).
- [112] C. de la Vaissiere et al., *Phys. Rev. Lett.* **54**, 2071 (1985), [Erratum: *Phys.Rev.Lett.* 55, 263 (1985)].
- [113] P. D. Acton et al. (OPAL), *Phys. Lett. B* **291**, 503 (1992).
- [114] W. Bartel et al. (JADE), *Phys. Lett. B* **104**, 325 (1981).
- [115] V. Khachatryan et al. (CMS), *JHEP* **05**, 064 (2011), 1102.4282.
- [116] D. Buskulic et al. (ALEPH), *Phys. Lett. B* **292**, 210 (1992).
- [117] A. Heister et al. (ALEPH), *Phys. Lett. B* **528**, 19 (2002), hep-ex/0201012.
- [118] O. Adriani et al. (L3), *Phys. Lett. B* **286**, 403 (1992).
- [119] M. Acciarri et al. (L3), *Phys. Lett. B* **328**, 223 (1994).
- [120] K. Ackerstaff et al. (OPAL), *Eur. Phys. J. C* **5**, 411 (1998), hep-ex/9805011.
- [121] W. Bartel et al. (JADE), *Z. Phys. C* **28**, 343 (1985).
- [122] D. D. Pitzl et al. (JADE), *Z. Phys. C* **46**, 1 (1990), [Erratum: *Z.Phys.C* 47, 676 (1990)].
- [123] H. J. Behrend et al. (CELLO), *Z. Phys. C* **47**, 1 (1990).
- [124] S. Abachi et al. (HRS), *Phys. Lett. B* **205**, 111 (1988).
- [125] H. Albrecht et al. (ARGUS), *Z. Phys. C* **46**, 15 (1990).
- [126] B. Abelev et al. (ALICE), *Phys. Lett. B* **717**, 162 (2012), 1205.5724.
- [127] S. Acharya et al. (ALICE), *Eur. Phys. J. C* **77**, 339 (2017), 1702.00917.
- [128] S. Acharya et al. (ALICE), *Eur. Phys. J. C* **78**, 263 (2018), 1708.08745.
- [129] A. Adare et al. (PHENIX), *Phys. Rev. D* **83**, 032001 (2011), 1009.6224.
- [130] S. Acharya et al. (ALICE) (2024), 2411.09560.
- [131] R. Barate et al. (ALEPH), *Z. Phys. C* **74**, 451 (1997).
- [132] W. Adam et al. (DELPHI), *Z. Phys. C* **69**, 561 (1996).
- [133] H.-T. Elze, *Z. Phys. C* **47**, 647 (1990).
- [134] W. Braunschweig et al. (TASSO), *Z. Phys. C* **42**, 189 (1989).
- [135] B. I. Abelev et al. (STAR), *Phys. Rev. C* **81**, 064904 (2010), 0912.3838.
- [136] A. Adare et al. (PHENIX), *Phys. Rev. D* **76**, 051106 (2007), 0704.3599.
- [137] A. Adare et al. (PHENIX), *Phys. Rev. D* **93**, 011501 (2016), 1510.02317.
- [138] S. Aid et al. (H1), *Nucl. Phys. B* **480**, 3 (1996), hep-ex/9607010.
- [139] M. Stratmann and W. Vogelsang, *Nucl. Phys. B* **496**, 41 (1997), hep-ph/9612250.
- [140] G. P. Salam and J. Rojo, *Comput. Phys. Commun.* **180**, 120 (2009), 0804.3755.
- [141] G. Salam and J. Rojo, in 16th International Workshop on Deep Inelastic Scattering and Related Subjects (2008), p. 42, 0807.0198.
- [142] J. Gao, FMNLO, <https://fmnlo.sjtu.edu.cn/~fmnlo/> (2024).
- [143] S. Dulat, T.-J. Hou, J. Gao, M. Guzzi, J. Huston, P. Nadolsky, J. Pumplin, C. Schmidt, D. Stump, and C. P. Yuan, *Phys. Rev. D* **93**, 033006 (2016), 1506.07443.
- [144] D. Stump, J. Pumplin, R. Brock, D. Casey, J. Huston, J. Kalk, H. L. Lai, and W. K. Tung, *Phys. Rev. D* **65**, 014012 (2001), hep-ph/0101051.
- [145] J. Pumplin, D. R. Stump, J. Huston, H. L. Lai, P. M. Nadolsky, and W. K. Tung, *JHEP* **07**, 012 (2002), hep-ph/0201195.
- [146] J. Collins and T. C. Rogers, *Phys. Rev. D* **109**, 016006 (2024), 2309.03346.
- [147] R. Aaij et al. (LHCb), *Phys. Rev. D* **108**, L031103 (2023), 2208.11691.
- [148] R. Seidl et al. (Belle) (2024), 2411.12216.
- [149] R. Aaij et al. (LHCb), *Phys. Rev. C* **109**, 024907 (2024), 2310.17326.
- [150] A. Buckley, J. Ferrando, S. Lloyd, K. Nordström, B. Page, M. Rüfenacht, M. Schönherr, and G. Watt, *The European Physical Journal C* **75** (2015), ISSN 1434-6052.
- [151] P. M. Nadolsky and Z. Sullivan, eConf **C010630**, P510 (2001), hep-ph/0110378.
- [152] <https://lhpdf.hepforge.org/pdfsets.html>